Publications of the Astronomical Society of the Pacific, 131:064301 (71pp), 2019 June https://doi.org/10.1088/1538-3873/aaf4e5

Consistent Dust and Gas Models for Protoplanetary Disks. III. Models for Selected Objects from the FP7 DIANA Project*

P. Woitke[1,2,14], I. Kamp[3], S. Antonellini[3,4], F. Anthonioz[5], C. Baldovin-Saveedra[6], A. Carmona[7], O. Dionatos[6], C. Dominik[8], J. Greaves[9], M. Güdel[6], J. D. Ilee[10], A. Liebhardt[6], F. Menard[5], M. Min[8,11], C. Pinte[5,12], C. Rab[3], L. Rigon[1], W. F. Thi[13], N. Thureau[1], and L. B. F. M. Waters[8,11]

[1] SUPA, School of Physics & Astronomy, University of St Andrews, North Haugh, KY16 9SS, UK; pw31@st-and.ac.uk
[2] Centre for Exoplanet Science, University of St Andrews, St Andrews, UK
[3] Kapteyn Astronomical Institute, University of Groningen, The Netherlands
[4] Astrophysics Research Centre, School of Mathematics and Physics, Queen's University Belfast, University Road, Belfast BT7 1NN, UK
[5] Université Grenoble-Alpes, CNRS Institut de Planétologie et d'Astrophyisque (IPAG) F-38000 Grenoble, France
[6] University of Vienna, Department of Astrophysics, Türkenschanzstrasse 17, A-1180, Vienna, Austria
[7] IRAP, Université de Toulouse, CNRS, UPS, Toulouse, France
[8] Astronomical institute Anton Pannekoek, University of Amsterdam, Science Park 904, 1098 XH, Amsterdam, The Netherlands
[9] School of Physics and Astronomy, Cardiff University, 4 The Parade, Cardiff CF24 3AA, UK
[10] School of Physics and Astronomy, University of Leeds, Leeds LS2 9JT, UK
[11] SRON Netherlands Institute for Space Research, Sorbonnelaan 2, 3584 CA Utrecht, The Netherlands
[12] Monash Centre for Astrophysics (MoCA) and School of Physics and Astronomy, Monash University, Clayton Vic 3800, Australia
[13] Max Planck Institute for Extraterrestrial Physics, Giessenbachstrasse, D-85741 Garching, Germany
Received 2018 January 11; accepted 2018 November 21; published 2019 May 6

Abstract

The European FP7 project DIANA has performed a coherent analysis of a large set of observational data of protoplanetary disks by means of thermo-chemical disk models. The collected data include extinction-corrected stellar UV and X-ray input spectra (as seen by the disk), photometric fluxes, low and high resolution spectra, interferometric data, emission line fluxes, line velocity profiles and line maps, which probe the dust, polycyclic aromatic hydrocarbons (PAHs) and the gas in these objects. We define and apply a standardized modeling procedure to fit these data by state-of-the-art modeling codes (`ProDiMo`, `MCFOST`, `MCMax`), solving continuum and line radiative transfer (RT), disk chemistry, and the heating and cooling balance for both the gas and the dust. 3D diagnostic RT tools (e.g., FLiTs) are eventually used to predict all available observations from the same disk model, the DIANA-standard model. Our aim is to determine the physical parameters of the disks, such as total gas and dust masses, the dust properties, the disk shape, and the chemical structure in these disks. We allow for up to two radial disk zones to obtain our best-fitting models that have about 20 free parameters. This approach is novel and unique in its completeness and level of consistency. It allows us to break some of the degeneracies arising from pure Spectral Energy Distribution (SED) modeling. In this paper, we present the results from pure SED fitting for 27 objects and from the all inclusive DIANA-standard models for 14 objects. Our analysis shows a number of Herbig Ae and T Tauri stars with very cold and massive outer disks which are situated at least partly in the shadow of a tall and gas-rich inner disk. The disk masses derived are often in excess to previously published values, since these disks are partially optically thick even at millimeter wavelength and so cold that they emit less than in the Rayleigh–Jeans limit. We fit most infrared to millimeter emission line fluxes within a factor better than 3, simultaneously with SED, PAH features and radial brightness profiles extracted from images at various wavelengths. However, some line fluxes may deviate by a larger factor, and sometimes we find puzzling data which the models cannot reproduce. Some of these issues are probably caused by foreground cloud absorption or object variability. Our data collection, the fitted physical disk parameters as well as the full model output are available to the community through an online database (http://www.univie.ac.at/diana).

* EU FP7-SPACE-2011 project 284405 "DiscAnalysis" (Analysis and Modeling of Multi-wavelength Observational Data from Protoplanetary Discs).
[14] Main DIANA website at https://dianaproject.wp.st-andrews.ac.uk.

Key words: astrochemistry – astronomical databases: miscellaneous – line: formation – molecular processes – protoplanetary disks – radiative transfer

Online material: color figures

1. Introduction

The European FP7-SPACE project DIANA[15] analyzed multi-wavelength and multi-kind observational data about protoplanetary disks by using a standardized modeling approach, in order to learn more about the physico-chemical state of the birthplaces of extra-solar planets, their evolution, and the pre-conditions for planet formation. In order to place our efforts into context, we first review the state-of-the-art of fitting disk observations by modeling.

Previous studies have applied a wealth of different disk modeling approaches and fitting techniques, often tailored toward one particular object or a fresh set of observations from a particular new instrument for a couple of disk sources. The approaches can be divided in order of increasing level of self-consistency.

1. Retrieval modeling of a few selected observables using radiative transfer (RT) techniques based on simple parametric disk models. A single model typically runs faster than a few CPU-min, such that χ^2 minimization, e.g., in form of genetic algorithms, and sometimes Monte Carlo Markov Chain (MCMC) techniques can be applied.
2. Multi-stage modeling, using RT-modeling of continuum observations first to determine the physical disk structure, before chemical and line-transfer modeling is applied to compare to line observations,
3. Analysis of large sets of multi-wavelengths observables using forward modeling of consistent RT and chemistry. These models are usually so expensive that many authors do not claim to have fitted all observations, but are rather seeking for a broad agreement with the data, in order to discuss several modeling options and new physical or chemical assumptions that work best to obtain that agreement.

The methodical differences in these individual disk modeling and fitting works are unfortunately so substantial that it is very difficult to cross-compare the results, for example the disk structures obtained, the disk masses determined, or the evolutionary trends deduced. This is a key goal of the homogeneous DIANA modeling approach presented in this paper. Some selected previous disk fitting studies are exemplified in the following, ordered by increasing level of self-consistency and complexity of the physics and chemistry applied.

[15] https://dianaproject.wp.st-andrews.ac.uk

1.1. Continuum Radiative Transfer Modeling (Dust and Polycyclic Aromatic Hydrocarbons (PAHs))

Full 2D/3D continuum RT techniques have been applied to model Spectral Energy Distributions (SEDs), for example (Andrews & Williams 2007; Andrews et al. 2013). More recently, SED fitting has been extended to include continuum visibilities and/or images. For example, Pinte et al. (2008) used the MCMC method to fit the SED and multi-wavelength continuum images of IM Lup with `MCFOST`. Wolff et al. (2017) performed a grid search and used the MCMC method to fit the SED and scattered light images of ESO-Hα 569. Muro-Arena et al. (2018) fitted the SED of HD 163296 in combination with scattered light images (Very Large Telescope (VLT)/SPHERE) and thermal emission (ALMA). Maaskant et al. (2013) fitted SEDs and Q-band images, using a stepwise procedure, for a small number of Herbig Ae sources with `MCMax`. Maaskant et al. (2014) have modeled dust and PAHs in a couple of Herbig Ae transition disks, aiming at determining the properties of PAHs in disk gaps using the disk models of their earlier work (Acke et al. 2010; Maaskant et al. 2013). An example for recent 3D continuum modeling is Min et al. (2016a), who used a genetic fitting algorithm for HD 142527. They have not applied the MCMC algorithm but used the history of their fitting method to identify some parameter degeneracies and to provide rough estimates of the uncertainties in parameter determination. Further examples to 3D disk SED fitting are given in Price et al. (2018) and Pinte et al. (2018).

These continuum modeling approaches are usually multi-λ and based on parametric disk structures, with or without hydrostatic equilibrium. The studies provide constraints on the disk dust structure, dust temperature, and the dust properties, but do not allow for much conclusions about the gas. If MCMC methods are used, these studies provide the credibility intervals for the determination of the various input parameters, and thus allow for a proper assessment of the quality and uniqueness of the fits.

1.2. Simplified Chemical Models

As an extension, models have been developed where the density and dust temperature structure is taken from full 2D dust RT models, but a parametric prescription is used for the molecular concentration, without computing any chemical rates in detail. Examples are Williams & Best (2014), Boneberg et al. (2016), Isella et al. (2016), and Pinte et al. (2018). The molecular abundance in the absence of photodissociation and freeze-out is a free parameter in these models, and usually $T_{\rm gas} = T_{\rm dust}$ is assumed. The molecular abundance is then switched to zero, or to a very small value, where one of the

above mentioned chemical destruction processes is thought to be dominant. This approach can be multi-wavelength, but usually concentrates on a series of lines from a single molecule, in most cases CO and its isotopologues observed at (sub-)mm wavelengths.

Such models are still fast and allow for MCMC approaches. However, they lack the chemical insight to explain why some molecules are confined to certain regions. Also, such models can only be applied to predict the lines of dominant molecules like CO, which contain the majority of the respective elements. The concentrations of other molecules like HCO^+ may not be so straightforward to guess, and so their line emission regions can be different.

1.3. Atomic/Molecular Line Emission Models

Some approaches employ pure RT techniques to fit line observations (fluxes, radial profiles, resolved line images or visibilities). These line radiative models are based on parametric column densities and a given radial temperature law, but without detailed heating/cooling balance or chemical rates. Dust continuum RT modeling can be part of these models. The best fits are derived via retrieval methods to determine the column density and temperature profile parameters, using for example power-law prescriptions.

The Chemistry in Disks (CID) project (Dutrey et al. 2007, and subsequent papers) is a good example. Dutrey et al. focused on N_2H^+ lines from DM Tau, Lk Ca 15 and MWC 480. The results of their fitting are radial profiles of molecular column densities and temperature. The main goal of this approach is to invert the line observations, as directly as possible, to determine the desired disk properties such as chemical abundances, column densities and temperatures, but without a detailed physical or chemical disk model that results in those structures. The main physics included is the line RT. Thanks to the simplicity of these models, a wide parameter space can be explored using χ^2-minimization. The approach is often applied to spatially resolved mm-data, where the dust continuum RT is less crucial, for example (Öberg et al. 2015; Teague et al. 2015). Formal errors on the parameters can be derived from the χ^2-minimization.

These results are then interpreted in the context of generic astrochemical disk models. Teague et al. (2015) presented a disk model for DM Tau to discuss the HCO^+ and DCO^+ sub-mm line observations. The authors used a combination of χ^2 minimization and MCMC fitting in visibility space to derive disk geometry parameters such as inner/outer radius, and inclination as well as physical parameters such as scale height, temperature and surface density power laws for each molecule independently. The authors subsequently use more physical disk models to explore the radial gradient in deuteration in the disk. The stellar parameters of DM Tau, an ISM-like UV radiation field and the accretion rate are taken from the literature to build a 1+1D steady state α-disk model. On top of the physical disk structure, the authors solve time-dependent chemistry using a large gas-grain chemical network including CR, UV and X-ray reactions. A similar approach is used by Semenov et al. (2018). In both cases, restricted disk parameters are varied to interpret the radial molecular column density profiles and to learn about disk ionization or elemental depletion.

At mid- and far-IR wavelengths, the continuum becomes non-negligible, thus requiring a combination of the above approach with dust RT, e.g., (Banzatti et al. 2012; Pontoppidan & Blevins 2014). Zhang et al. (2013) used a detailed physical dust structure, but parametric molecular abundance/column densities. On top of the manually fitted dust RT model (RADMC, Dullemond & Dominik 2004), the authors computed water lines over a wide wavelength range (mid- to far-IR) and discussed the water ice line for the transitional disk around TW Hya in the context of *Spitzer* and *Herschel* data. (Blevins et al. 2016) used a similar approach to model *Spitzer* and *Herschel* water lines in four primordial disks. Similar techniques are also applied for near-infrared CO rovibrational lines, for example (Carmona et al. 2017).

The resulting disk structures of such approaches can be quite degenerate (dust structure, temperature, column density, line emitting region) if unresolved data is used like *Spitzer* and *Herschel* line fluxes and SEDs. The situation improves if a large wavelength range of lines/multiple species are used and/or spatial information is available. However, as far as we know, detailed fitting strategies and an evaluation of the goodness of such fits have never been attempted.

1.4. Pure Chemical Models

This approach uses a proper chemical model on top of a fixed disk structure, i.e., the physical properties like densities, temperatures and radiation fields are calculated once and then fixed. Those quantities are either estimated or taken from a dust RT code. Thus, the gas chemistry has no mutual influence on the physical properties in the disk, including its temperature structure or dust settling. This approach is used, for example, to interpret molecular column density profiles derived from observations (see e.g., CID papers cited above). In those cases, the authors do not fit observations with a chemical model, but rather vary some chemical parameters and discuss what matches the observations best or what is missing, with the intention to improve astro-chemical networks in general. Some of these works may not use detailed UV properties of the star in combination of UV disk RT, or may not be consistent with the observed SED.

Some works go beyond this approach by using dust structures consistent with continuum observations and tailored for specific targets. Cleeves et al. (2015) fitted the SED of TW Hya using existing dust models and carrying out TORUS

RT models (Harries 2000). The gas mass is calibrated using a parametric gas temperature profile (based on $T_{\rm dust}$ and the local FUV radiation field) and the observed HD flux. The disk structure is then fixed and the authors explore cosmic ray (CR) and X-ray processes to fit the radial emission profiles of various mm-lines (mainly ions) using LIME (Brinch & Hogerheijde 2011). A similar approach is used for IM Lup (Cleeves et al. 2016). Here, a chain of dust RT, X-ray and UV RT models is executed. A parametric gas temperature (based on $T_{\rm dust}$ and the local FUV radiation field) is used to calculate the molecular gas distribution based on chemical models. LIME is used to produce CO channel maps for various levels of CO depletion and external UV radiation fields. A χ^2-minimization strategy is applied to find the best match to the observed ALMA channel maps, but without MCMC algorithm to determine the errors.

The computation times of such chemical models are generally orders of magnitude higher than those of continuum RT models. Hence MCMC or other exhaustive χ^2-minimization strategies are generally avoided, as these would require at least hundreds of thousands of such models. This makes it difficult to evaluate in how far the results are degenerate. The conclusions drawn from such approaches are therefore often limited to a specific goal or question in the respective study. Vasyunin et al. (2008) did a sensitivity analysis for the chemistry. The errorbars given in the CID papers (Dutrey et al. 2007, and subsequent papers) are based on those results.

1.5. Radiation Thermo-chemical Models—Consistent Dust and Gas Models

This approach calculates self-consistently the dust temperature, gas temperature, chemical abundances, and optionally the vertical disk structure. Such models include a dust RT module, a chemistry module, a heating/cooling module, and some post-processing tools to derive for example visibilities, images, line profiles and channel maps. These codes include most of the aspects mentioned before, but not necessarily as sophisticated as used in the individual chemical models illustrated above. Examples of such codes are `ProDiMo` (Woitke et al. 2009; Kamp et al. 2010; Aresu et al. 2011; Thi et al. 2011; Rab et al. 2018), DALI (Bruderer et al. 2009, 2012; Bruderer 2013), the Gorti et al. (2011) code, and the Du & Bergin (2014) code. In this approach, a small chemical network is often used that is sufficient to predict the abundances of the main coolants and observed simple molecules, for example no isotope chemistry, no surface chemistry except adsorption and desorption, and steady-state chemistry. The focus is to determine the physical properties of disks, especially their radial/vertical structure. They are also a critical test-bed/virtual laboratory for our understanding of the complex coupling between radiation/energetic particles (X-ray, UV, cosmic rays, stellar particles), dust particles and gas.

Gorti et al. (2011) modeled the disk around TW Hya in the context of a large set of observed line fluxes (e.g., forbidden optical lines such as [S II], [O I], near- and mid-IR lines as well as sub-mm CO and HCO^+ lines). This disk model and derivations thereof are used also in subsequent studies (e.g., Bergin et al. 2013; Favre et al. 2013). Gorti et al. (2011) compiled a detailed input spectrum using stellar parameters from the literature to select a suitable stellar atmosphere model for the photospheric spectrum, completed by a *Far-Ultraviolet Spectroscopic Explorer* (*FUSE*) spectrum and *XMM-Newton* X-ray data and the Lyα luminosity. The dust model and the surface density distribution is a simplified version of a previous study by Calvet et al. (2002) that matched the SED and 7 mm images. It remains unclear, however, whether the "simplified dust model" still fits the SED and the images. The authors then vary the gas surface density on top of the dust until they match the optical to sub-mm line fluxes. No additional effort to consistently fit SED and lines was reported.

DALI was used to fit the CO ladder of HD 100546 and a series of fine-structure lines from neutral/ionized carbon and neutral oxygen (Bruderer et al. 2012) by varying a limited set of disk parameters (e.g., dust opacities, outer disk radius, carbon abundance, and the gas-to-dust mass ratio). In this case, no effort was made to fit the continuum observables such as SED and/or images. Kama et al. (2016b) used DALI to model HD 100546 and TW Hya, performing hand-fitting of the SED by varying a limited set of disk parameters (dust and gas depletion in gaps, dust surface density distribution, disk scale height, flaring angle, tapering off, dust settling). In addition to the previously mentioned lines, they also included C_2H lines and line profiles of CO and [C I]. Typically of the order of 100 models were explored per source. DALI has also been used to interpret ALMA observations of disks, in particular the gas and dust surface density distribution of transition disks, for example by van der Marel et al. (2016) and Fedele et al. (2017).

Du et al. (2015) modeled TW Hya for a selection of gas emission lines from mid-IR to mm (fine-structure lines, CO isotopologues, water, OH, and HD). They showed that their constructed dust model matches the SED and sub-mm image, but they do not attempt to fit the sub-mm visibilities. They fitted the line observations by adjusting the carbon and oxygen abundances, either considered to be ISM-like or modified, with a genetic algorithm. The results of these two models are then discussed in the context of the observations, but no detailed gas line fitting is attempted.

Woitke et al. (2011, ET Cha), Tilling et al. (2012, HD 163296), Thi et al. (2014, HD 141569A) and Carmona et al. (2014, HD 135344B) provide examples of `ProDiMo` + `MCFOST` disk fitting. For example, Woitke et al. (2011) employed a genetic algorithm to find the best parameter combination (11 parameters) to fit a wide range of observables: SED, *Spitzer* spectrum, [O I] 6300 Å, near-IR H_2, far-IR *Herschel* atomic and molecular lines (partly upper limits), and CO 3–2. In this case, the confidence intervals of the determined model parameters are

estimated by a-posteriori variation of single parameters around the χ^2-minimum.

1.6. Grid-approach

We list this approach here mainly for completeness. Its use for fitting disk observations of individual targets is quite limited due to the large number of free parameters in disk modeling, which allows for just a few values per parameter to span several orders of magnitude. Often a sub-selection of parameters must be made to study more specific questions. Diagnostic methods derived from such grids have to be evaluated critically in the context of the non-varied parameters and model simplifications. Examples for this approach are the DENT grid (Pinte et al. 2010; Woitke et al. 2010; Kamp et al. 2011) for SEDs, mid- to far-IR and sub(mm) lines, Williams & Best (2014) and Miotello et al. (2016) for (sub)mm CO isotopologues lines, and Du et al. (2017) for water lines. This approach is mainly driven by the endeavor to understand the predicted changes of observables as selected parameters are varied systematically. Ultimately, such trends can possibly be inverted to devise new diagnostic tools for observations.

1.7. The DIANA Approach

The bottom line of the above summary of published disk modeling works is that full radiation thermo-chemical models, where all disk shape, dust and gas parameters have been commonly varied to obtain the best fit of line and continuum data, have not yet been applied to more than a single object. Fitting gas line observations is usually performed on top of a given disk dust structure. Disk modeling assumptions vary significantly between papers, making it virtually impossible to cross-compare the derived physical disk properties, even if those papers come from the same group.

This is where our approach is new and makes a difference. The ambitious goal of the DIANA project was to perform a coherent analysis of *all* available continuum and line observational data for a statistically relevant sample of protoplanetary disks. Our approach is based on a clearly defined succession of three modeling steps: (i) to fit the stellar and irradiation properties of the central stars; (ii) to apply state-of-the-art 2D disk modeling software `ProDiMo` (Woitke et al. 2009; Kamp et al. 2010; Thi et al. 2011), `MCFOST` (Pinte et al. 2006, 2009) and `MCMax` (Min et al. 2009), with a fixed set of physical and chemical assumptions, to simultaneously fit the disk shape, dust opacity and gas parameters of all objects; and (iii) to use various post-processing RT tools, including FLiTs (Woitke et al. 2018, written by M. Min) to compute spectra and images that can be compared to the available observational data. Contrary to many earlier efforts, our physical and chemical modeling assumptions are not changed as we apply them to different objects. The simultaneous gas and dust modeling is designed to be as self-consistent as possible to cover the following feedback mechanisms:

1. Changing the dust properties means to change the internal disk temperature structure, and to change the ways in which UV photons penetrate the disk, which is of ample importance for the photochemistry, freeze-out, and line formation.
2. Changing the gas properties affects dust settling. Disks with strong line emission may require a flaring gas structure, which can be different from the dust flaring if settling is taken into account in a physical way.
3. Changing or adding an inner disk, to fit some near-IR observations, will put the outer disk into a shadow casted by the inner disk, which changes the physico-chemical properties of the outer disks and related mm-observations.

These are just a few examples. Exploiting these feedback mechanisms can help to break certain degeneracies as known, for example, from pure SED-fitting. Our data collection is available in a public database (DIOD, Dionatos et al. 2019), which includes photometric fluxes, low and high-resolution spectroscopy, line and visibility data, from X-rays to centimeter wavelengths, and respective meta-data such as references. The database is online at http://www.univie.ac.at/diana, together with our fitted stellar and disk properties and detailed modeling results, which are also available in an easy to use format at http://www-star.st-and.ac.uk/~pw31/DIANA/SEDfit. This makes our work completely transparent and reproducible. The predictive power of these models can be tested against new observations, for example unexplored molecules, other wavelength ranges or new instruments. Our results do not only contain the fitted observations, but we also provide predictions for a large suite of other possible observations (continuum and lines), which are computed for all our targets in the same way. The long-term purpose of our disk modeling efforts is

1. to determine the disk masses, the disk geometry and shape, and the internal gas and dust properties (i.e., the dust and gas density distribution in the radial and vertical direction) for a large sample of well-studied protoplanetary disks;
2. to prepare cross-comparisons between individual objects, by applying standardized modeling assumptions and identical modeling techniques to each object;
3. to offer our disk modeling results, including the disk internal physico-chemical structure and a large variety of predicted observations to the community via a web-based interface; and
4. to provide all relevant information and input files to ensure that all individual models can be reproduced, also by researchers from the wider community.

With our open policy to offer our modeling results to the community, we hope to stimulate future research in neighboring research areas, such as hydrodynamical disk modeling and planet formation theories.

2. Target Selection and Stellar Properties

At the beginning of the project, a full DIANA targetlist with 85 individual protoplanetary disks was compiled from well-studied Herbig Ae stars, class II T Tauri stars, and transitional disk objects, covering spectral types B9 to M3. The selection of objects was motivated by the availability and overlap of multi-wavelength and multi-kind, line and continuum data. However, additional criteria have been applied as well, for example the exclusion of strongly variable objects, where the data from different instruments would probe different phases, and the exclusion of multiple or embedded sources, where the observations are often confused by foreground/background clouds or companions in the field, which is a problem in particular when using data from instruments with different fields of view. We do not claim that this target list is an unbiased sample. The full DIANA targetlist was then prioritized and a subset thereof was identified and put forward to detailed disk modeling. The modeling was executed by different members of the team, but was not completed within the run-time of DIANA for all objects. The completed list of objects is shown in Table 1, together with the results of our first modeling step, which is the determination of the stellar parameters and UV and X-ray irradiation properties.

3. Methods

3.1. Modeling Step 1: Fitting the Stellar Parameters

The first step of our modeling procedure is to determine the stellar parameters (stellar mass $M_\star$, stellar luminosity $L_\star$ and effective temperature $T_{\rm eff}$), as well as the interstellar extinction A_V, and the incident spectrum of UV and X-ray photons as irradiated by the star onto the disk. These properties are essential to setup the subsequent disk models. The method we have used for all objects is explained in Woitke et al. (2016, see Appendix A therein), assuming that these parts of the spectrum are entirely produced by the central star, without the disk. We hence neglect scattering of optical and UV photons by the disk surface in this modeling step. The method cannot be applied to edge-on sources where the disk is (partly) in the line of sight toward the star. However, we can check this later, when absorption and scattering by the disk is included, and can adjust in this case. We use a large collection of optical and near-IR photometry points in combination with low-resolution UV spectra, UV photometry points, and X-ray measurements.

We fit the photospheric part of each data set by standard PHOENIX stellar atmosphere model spectra (Brott & Hauschildt 2005), with solar abundances $Z = 1$, after applying a standard reddening law (Fitzpatrick 1999) according to interstellar extinction A_V and reddening parameter R_V. A standard value of $R_V = 3.1$ is applied to all stars if not stated otherwise. All photometric data in magnitudes have been converted to Jansky ($F_{\rm filter}^{\rm obs}$) based on instrument filter functions and zero-point data kindly provided by P. Degroote (2018, private communication). The stellar model is then compared to those data, depending on detector type, as

$$\text{CCD-detectors:} \qquad F_{\rm filter}^{\rm mod} = \frac{\int \frac{1}{\lambda} F_\nu^{\rm mod}\, t_{\rm filter}(\lambda) d\lambda}{\int \frac{1}{\lambda} t_{\rm filter}(\lambda) d\lambda}, \tag{1}$$

$$\text{BOL-detectors:} \qquad F_{\rm filter}^{\rm mod} = \frac{\int \frac{1}{\lambda^2} F_\nu^{\rm mod}\, t_{\rm filter}(\lambda) d\lambda}{\int \frac{1}{\lambda^2} t_{\rm filter}(\lambda) d\lambda}, \tag{2}$$

where $t_{\rm filter}(\lambda)$ are the filter transmission functions and $F_\nu^{\rm mod}$ [Jy] is the high-resolution model spectrum, assuming that CCD detectors measure photon counts and bolometers measure photon energy. The fit quality of the model is then determined with respect to all selected photometric data points $i = 1 \ldots I$, within wavelength interval $[\lambda_1, \lambda_2]$ as

$$\chi^2 = \frac{1}{I} \sum_{i=1}^{I} \begin{cases} \left(\dfrac{\log\left(F_i^{\rm mod}/F_i^{\rm obs}\right)}{\sigma_i^{\rm obs}/F_i^{\rm obs}} \right)^2 & \text{if } F_i^{\rm obs} > 3\,\sigma_i^{\rm obs} \\ \left(\dfrac{F_i^{\rm mod}}{3\,\sigma_i^{\rm obs}} \right)^2 & \text{otherwise} \end{cases}, \tag{3}$$

where $\sigma_i^{\rm obs}$ are the measurement errors. The selection of photometric data and wavelength fit range was made manually for each object. Typical choices are 400–600 nm to 2–3 μm for T Tauri stars and 150–250 nm to 1–2 μm for Herbig Ae stars, depending on the observed level of non-photospheric emission in the UV and IR.

We have used the (1, 12)-evolutionary strategy of Rechenberg (1994) to fit our model parameters P_j (here $L_\star$, $T_{\rm eff}$, A_V) to the data by minimizing χ^2

$$P_{g,j}^k = P_{g,j}^0 + r\ \delta_g\ \Delta P_j \quad (k = 1\ \ldots\ 12), \tag{4}$$

$$P_{g+1,j}^0 = P_{g,j}^{k_{\rm best}}, \tag{5}$$

$$\delta_{g+1} = \begin{cases} \delta_g/1.4 & \text{if } N_{\rm better} = 0 \\ \delta_g & \text{if } 1 \leqslant N_{\rm better} \leqslant 2, \\ \delta_g \times 1.4 & \text{if } N_{\rm better} > 2 \end{cases} \tag{6}$$

where $P_{g,j}^0$ are the parameter values of the parent of generation g, ΔP_j are user-set search widths ($\Delta P_j = 0$ means to freeze the value of parameter j), δ_g is the stepsize, and

$$r = \sqrt{-2\ln(1 - z_1)}\sin(2\pi\, z_2) \tag{7}$$

are normal-distributed random numbers with mean value $\langle r \rangle = 0$ and standard deviation $\langle r^2 \rangle = 1$. They are created from pairs of uniformly distributed pseudo-random numbers $0 \leqslant z_1, z_2 < 1$. $k_{\rm best}$ is the index of the child with lowest χ^2 and

Table 1
Stellar Parameters, and UV and X-Ray Irradiation Properties, for 27 Protoplanetary Disks

Object	SpTyp[a]	d (pc)	A_V[b]	$T_{\rm eff}$(K)	$L_\star(L_\odot)$[b]	$M_\star(M_\odot)$[a]	age (Myr)[a]	$L_{\rm UV,1}$[c]	$L_{\rm UV,2}$[d]	$L_{\rm X,1}$[e]	$L_{\rm X,2}$[f]
HD 100546	B9[g]	103	0.22	10470	30.5	2.5	>4.8[g]	8.0	1.6(−2)	4.9(−5)	2.0(−5)
HD 97048	B9[g]	171	1.28	10000	39.4	2.5	>4.8[g]	7.2	1.9(−2)	2.1(−5)	1.4(−5)
HD 95881	B9[g]	171	0.89	9900	34.3	2.5	>4.8[g]	4.9	8.0(−2)	2.0(−5)[h]	1.3(−5)[h]
AB Aur	B9[i]	144	0.42	9550	42.1	2.5	>4.5[i]	4.0	9.6(−3)	2.3(−4)	2.6(−5)
HD 163296	A1	119	0.48	9000	34.7	2.47	4.6	2.1	1.8(−2)	1.5(−4)	4.4(−5)
49 Cet	A2	59.4	0.00	8770	16.8	2.0	9.8	1.0	1.7(−4)	2.6(−4)	5.3(−5)
MWC 480	A5	137	0.16	8250	13.7	1.97	11	5.6(−1)	3.8(−3)	1.5(−4)	2.5(−5)
HD 169142	A7	145	0.06	7800	9.8	1.8	13	2.2(−1)	1.6(−5)	4.8(−5)	1.4(−6)
HD 142666	F1[j]	116	0.81	7050	6.3	1.6	>13[j]	3.7(−2)[k]	5.6(−9)[k]	1.6(−4)	1.1(−5)
HD 135344B	F3	140	0.40	6620	7.6	1.65	12	3.2(−2)	6.3(−3)	2.4(−4)	5.3(−5)
V 1149 Sco	F9	145	0.71	6080	2.82	1.28	19	5.1(−2)	1.4(−2)	3.7(−4)	2.8(−5)
Lk Ca 15	K5[l]	140	1.7	4730	1.2	1.0	≈2[l]	5.1(−2)	6.3(−3)	5.5(−4)	1.7(−4)
USco J1604-2130	K4	145	1.0	4550	0.76	1.2	10	4.0(−3)[m]	3.1(−4)[m]	2.6(−4)[n]	5.3(−5)[n]
RY Lup	K4	185	0.29	4420	2.84	1.38	3.0	2.4(−3)	1.5(−4)	4.3(−3)	3.6(−4)
CI Tau	K6	140	1.77	4200	0.92	0.90	2.8	2.0(−3)	8.7(−5)	5.0(−5)	1.0(−5)
TW Cha	K6	160	1.61	4110	0.594	1.0	4.3	7.2(−2)	4.4(−3)	3.4(−4)	1.0(−4)
RU Lup	K7	150	0.00	4060	1.35	1.15	1.2	1.4(−2)	9.0(−4)	7.1(−4)	3.4(−4)
AA Tau	K7	140	0.99	4010	0.78	0.85	2.3	2.3(−2)	5.8(−3)	1.1(−3)	3.2(−4)
TW Hya	K7	51	0.20	4000	0.242	0.75	13	1.1(−2)	4.2(−4)	7.7(−4)	7.0(−5)
GM Aur	K7	140	0.30	4000	0.6	0.7	2.6	6.6(−3)	2.8(−3)	7.0(−4)	1.2(−4)
BP Tau	K7	140	0.57	3950	0.89	0.65	1.6	1.3(−2)	1.1(−3)	5.9(−4)	2.5(−4)
DF Tau[o]	K7	140	1.27	3900	2.46	1.17	≈2.2[o]	3.6(−1)	2.9(−1)	–[p]	–[p]
DO Tau	M0	140	2.6	3800	0.92	0.52	1.1	1.3(−1)	2.7(−2)	1.1(−4)	4.1(−5)
DM Tau	M0	140	0.55	3780	0.232	0.53	6.0	7.0(−3)	6.3(−4)	8.4(−4)	2.9(−4)
CY Tau	M1	140	0.10	3640	0.359	0.43	2.2	7.3(−4)	7.1(−5)	2.1(−5)	6.9(−6)
FT Tau	M3	140	1.09	3400	0.295	0.3	1.9	5.2(−3)[q]	8.4(−4)[q]	2.3(−5)[r]	7.0(−6)[r]
RECX 15	M3	94.3	0.65	3400	0.091	0.28	6.5	6.3(−3)	4.0(−4)	1.7(−5)	8.2(−6)

Notes. The table shows spectral type, distance d, interstellar extinction A_V, effective temperature $T_{\rm eff}$, stellar luminosity $L_\star$, stellar mass $M_\star$, age, and UV and X-ray luminosities without extinction, i.e., as seen by the disk. Numbers written $A(-B)$ mean $A \times 10^{-B}$. The UV and X-ray luminosities are listed in units of $[L_\odot]$.
[a] Spectral types, ages and stellar masses are consistent with evolutionary tracks for solar-metallicity pre-main sequence stars by Siess et al. (2000), using $T_{\rm eff}$ & $L_\star$ as input.
[b] Derived from fitting our UV, photometric optical and X-ray data, see Section 3.1.
[c] FUV luminosity from 91.2 to 205 nm, as seen by the disk.
[d] Hard FUV luminosity from 91.2 to 111 nm, as seen by the disk.
[e] X-ray luminosity for photon energies >0.1 keV, as seen by the disk
[f] Hard X-ray luminosity from 1 to 10 keV, as seen by the disk.
[g] No matching track, values from closest point at $T_{\rm eff} = 10{,}000$ K and $L_\star = 42\,L_\odot$.
[h] No X-ray data available, X-ray data taken from HD 97048.
[i] No matching track, values from closest point at $T_{\rm eff} = 9650$ K and $L_\star = 42\,L_\odot$.
[j] No matching track, values from closest point at $T_{\rm eff} = 7050$ K and $L_\star = 7\,L_\odot$.
[k] "low-UV state" model, where a purely photospheric spectrum is assumed.
[l] No matching track, values taken from (Kraus & Ireland 2012; Drabek-Maunder et al. 2016).
[m] No UV data, model uses $f_{\rm UV} = 0.01$ and $p_{\rm UV} = 2$ (see Woitke et al. 2016, Appendix A for explanations).
[n] No X-ray data, model uses $L_X = 10^{30}$ erg s^{-1} and $T_X = 20$ MK (see Woitke et al. 2016, Appendix A for explanations).
[o] Resolved binary, 2× spectral type M1, luminosities 0.69 $L_\odot$ and 0.56 $L_\odot$, separation 0.″094 ≈ 13 au (Hillenbrand & White 2004).
[p] No X-ray data available.
[q] No UV data, model uses an UV-powerlaw with $f_{\rm UV} = 0.025$ and $p_{\rm UV} = 0.2$ (see Woitke et al. 2016, Appendix A for explanations).
[r] No detailed X-ray data available, model uses a bremsstrahlungs-spectrum with $L_X = 8.8 \times 10^{28}$ erg s^{-1} and $T_X = 20$ MK, based on archival XMM survey data (M. Güdel 2018, private communication).

$N_{\rm better}$ is the number of children with χ^2 better than their parent. In order to escape local minima, it is important in this strategy to always accept the best child as new parent, even if the fit quality of the child is worse than the fit quality of its parent. In numerous tests, we found that this genetic fitting algorithm is very robust and reliable, even if the models are noisy as will become relevant in the next modeling step where Monte-Carlo RT techniques are applied.

Since most of our sources are well-studied with high-resolution spectroscopy, we used distance, d, and effective

temperatures $T_{\rm eff}$-values from the literature.[16] Once $T_{\rm eff}$ and $L_\star$ are determined, we involve pre-main sequence stellar evolutionary models (Siess et al. 2000) to determine $M_\star$, the spectral type and the age of the star. Based on those results, the stellar radius $R_\star$ and the surface gravity $\log g$ can be computed which are then used in the next iteration step to better select our photospheric spectra (which depend on $T_{\rm eff}$ and $\log g$). For given d and $T_{\rm eff}$, this iteration is found to converge very quickly to a unique solution. Certain combinations of d and $T_{\rm eff}$ found in the literature, however, needed to be rejected this way, because the procedure described above resulted in an impossible location in the Hertzsprung–Russel diagram.

A large collection of UV low- and high-resolution archival data was collected from different instruments (*IUE*, *FUSE*, Space Telescope Imaging Spectrograph, Cosmic Origins Spectrograph, Advanced Camera for Surveys), and then collated, averaged and successively re-binned until statistically relevant data was obtained, using the method of weighted means described in Valenti et al. (2000, 2003). The details are described in Dionatos et al. (2019, see Figure 3 therein). These spectra were then de-reddened according to our A_V to obtain the stellar UV-spectra as seen by the disk. These UV input spectra are included in our database DIOD. The de-reddened data is used to replace the photospheric model in the UV, and possible gaps between UV spectral data and photospheric model spectrum are filled by powerlaws.

X-ray data was collected from *XMM-Newton* and *Chandra*. A physically detailed X-ray emission model was fitted to these observations (Dionatos et al. 2019), from which we extracted a high-resolution X-ray emission spectrum as seen by the disk by not computing the last modeling step, namely the reduction of the X-ray fluxes by extinction. These X-ray emission spectra are also available in our database DIOD. As a side result, the modeling of the X-ray data provided estimates of the hydrogen column densities toward the sources, which is useful to verify our results for A_V.

The stellar properties, and in particular the assumed visual extinction A_V, have a profound influence on the disk modeling results. The stellar parameters must be carefully adjusted and checked against UV and optical data to make sure that this part of the spectrum is properly reproduced by the model. A blind application of published stellar parameters can lead to substantial inconsistencies. If A_V is overestimated, for example, one needs to assume larger values for $L_\star$, which would then make the disk warmer and brighter in the infrared and beyond. A more substantial de-reddening would result in a stronger UV spectrum as seen by the disk, causing stronger emission lines, etc. The resulting stellar properties of our target objects are listed in Table 1 for 27 objects. The photometric and UV data are visualized in Figure 1.

[16] The setup of all our models was executed before the first GAIA data release.

3.2. Modeling Step 2: SED Fitting

The second step of our modeling pipeline is to fit the SED of our targets including all photometric data points and low-resolution spectra (*Infrared Space Observatory* (*ISO*)/SWS and LWS, *Spitzer*/intensified Reticon spectrograph (IRS), *Herschel*/PACS and SPIRE) from near-IR to millimeter wavelengths. The data partly contains mid-IR PAH emission features which we aim to fit as well. Our model is composed of a central star, with parameters fixed by the previous modeling step, surrounded by an axi-symmetric dusty disk seen under inclination angle i, which is taken from the literature. Our physical assumptions about the gas, dust particles and PAHs in the protoplanetary disk are detailed in Woitke et al. (2016, Section 3 therein). We briefly summarize these assumptions here.

1. passive disk model, i.e., no internal heating of the dust by viscous processes,
2. up to two radial disk zones, optionally with a gap in-between,
3. prescribed gas column density as function of radius in each disk zone, using a radial power-law with a tapered outer edge,
4. fixed gas-to-dust mass ratio in each zone,
5. parametric gas scale height as function of radius in each zone, using a radial powerlaw,
6. dust settling according to Dubrulle et al. (1995), with typically 100 size-bins,
7. we apply the DIANA standard dust opacities for disks, based on a power-law dust size distribution, an effective mixture of laboratory silicate and amorphous carbon, porosity, and a distribution of hollow spheres (DHS), see Min et al. (2016b) and Woitke et al. (2016), and
8. simplified PAH absorption and re-emission optionally included, see Woitke et al. (2016, Section 3.8).

These disk models are run by means of our fast Monte Carlo RT tools `MCFOST` and/or `MCMax`. The number of free parameters to fit are

1. Inner and outer radius of each zone $R_{\rm in}$ and $R_{\rm out}$. In the outermost zone, the outer radius is exchanged by the tapering-off radius $R_{\rm tap}$, and the disk is radially extended until the total hydrogen nuclei column density reaches the tiny value of $10^{20}\,{\rm cm}^{-2}$.
2. The disk gas mass $M_{\rm disk}$ and the column density powerlaw index ϵ in each zone. In case of the outermost disk zone, there is in addition the tapering-off power-index γ.
3. The dust-to-gas ratio in each zone.
4. The gas scale height H_0 at some reference radius and the flaring index β in each disk zone.

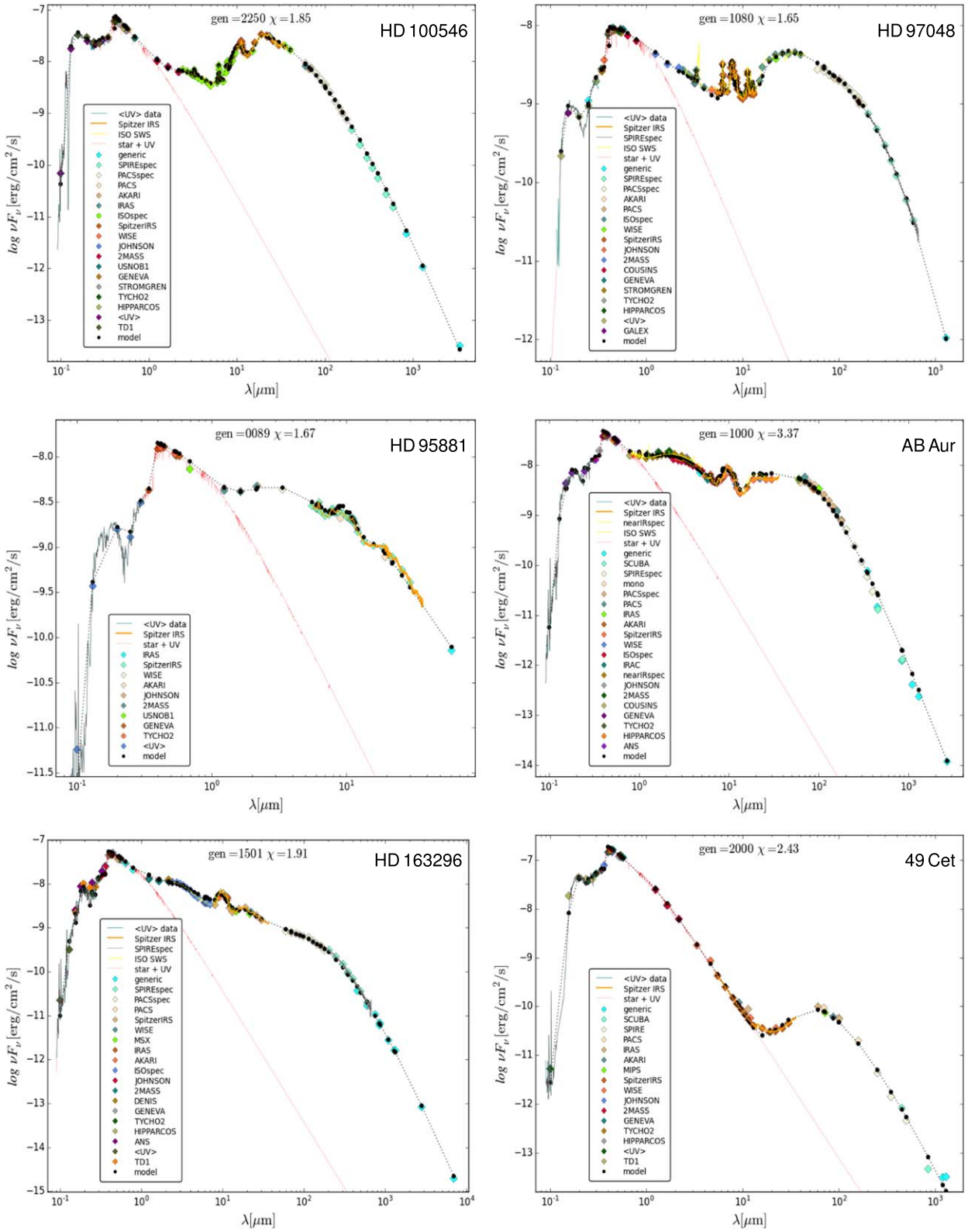

Figure 1. SED-fitting models after reddening, in comparison to all photometric and low-resolution spectroscopic data. All spectroscopic data have been converted into a small number of spectral points. The red line is the fitted photospheric + UV spectrum of the star. The black dots represent the fluxes computed by MCFOST, only at the wavelength points where we have observations. These model fluxes are connected by a black dashed line. The other colored dots and lines are the observational data as indicated in the legends. The "generic" points are individual measurements, usually in the mm-region, where a generic filter of type BOL (see Equation (2)) with a relative spectral width 12% was applied.

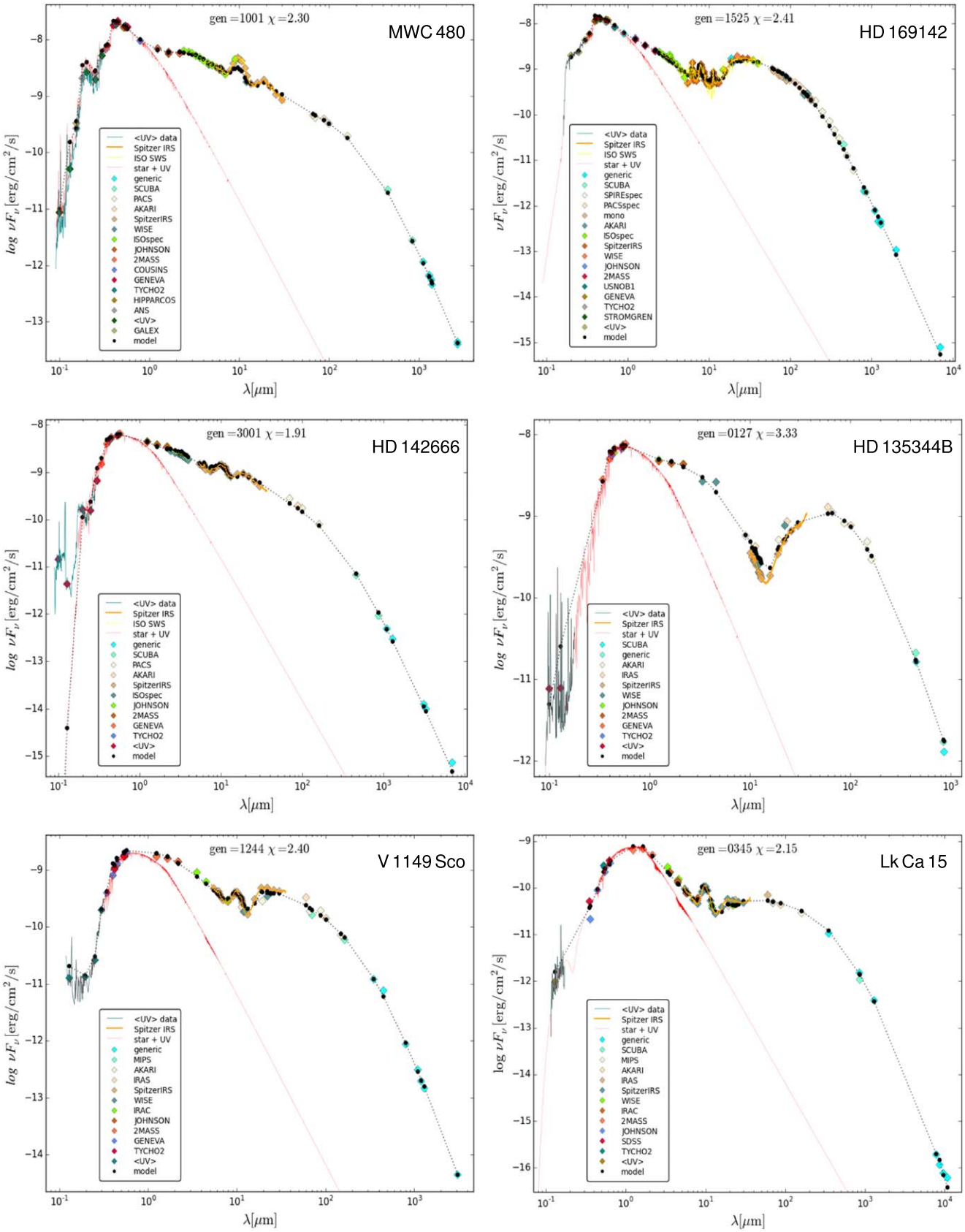

Figure 1. (Continued.)

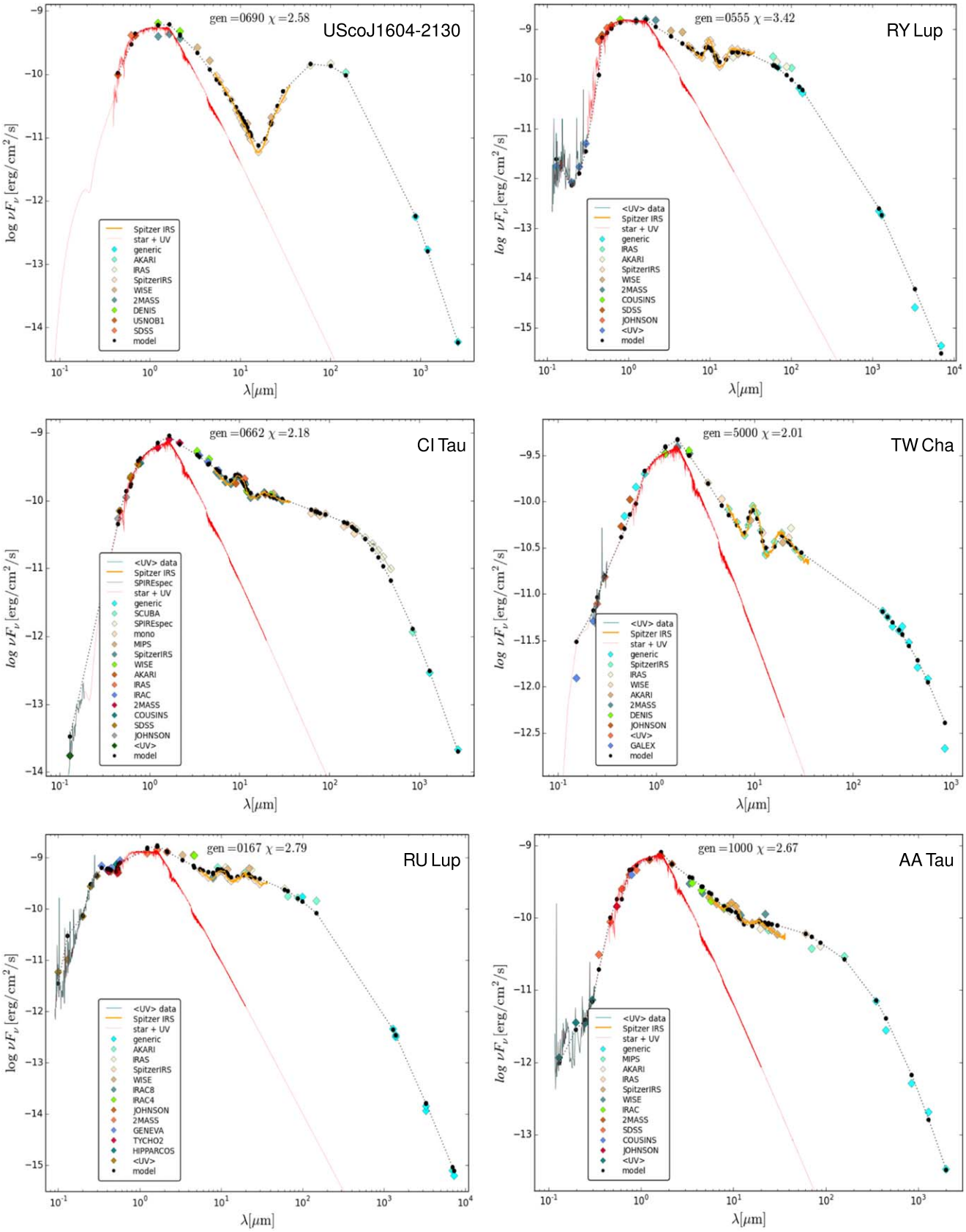

Figure 1. (Continued.)

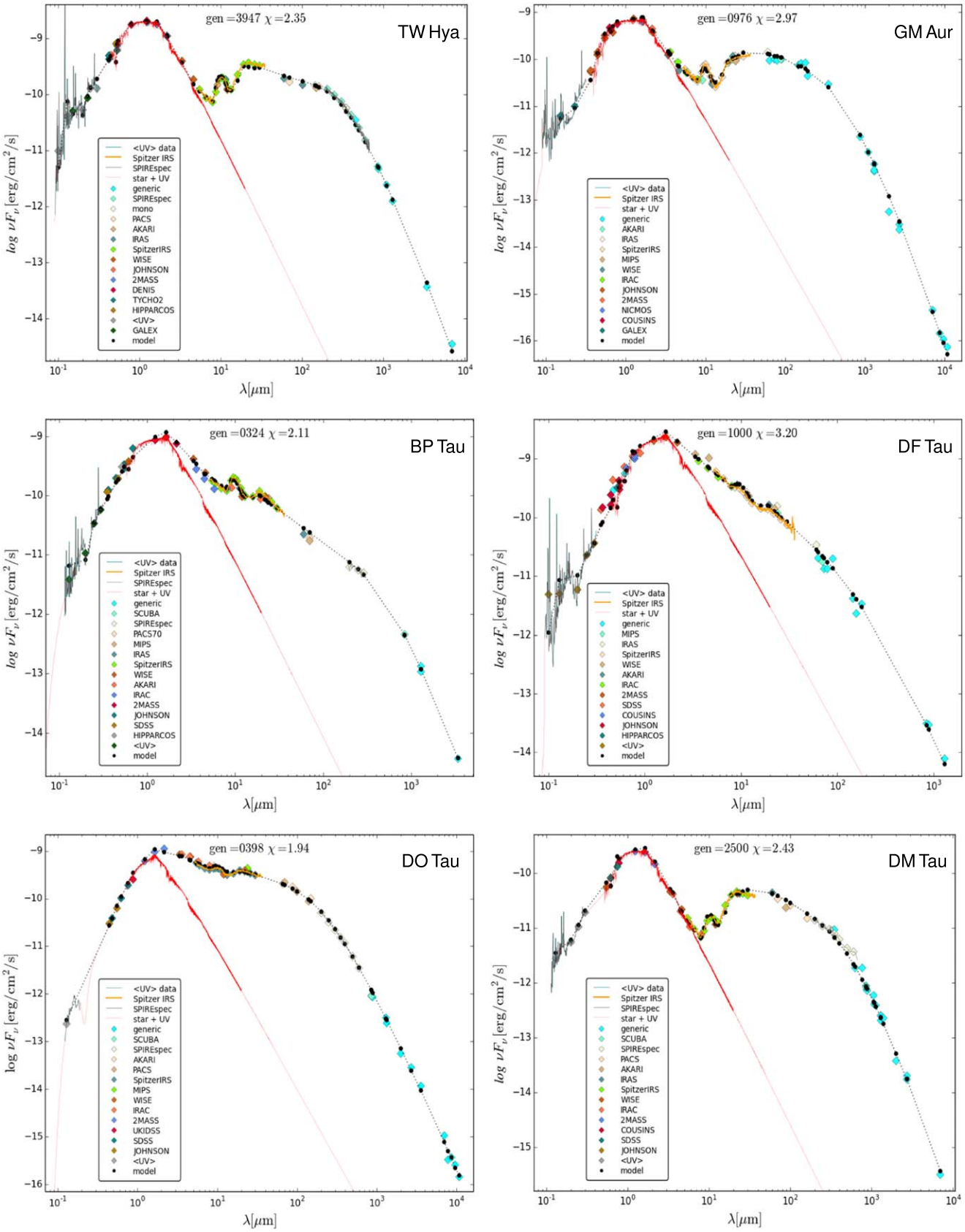

Figure 1. (Continued.)

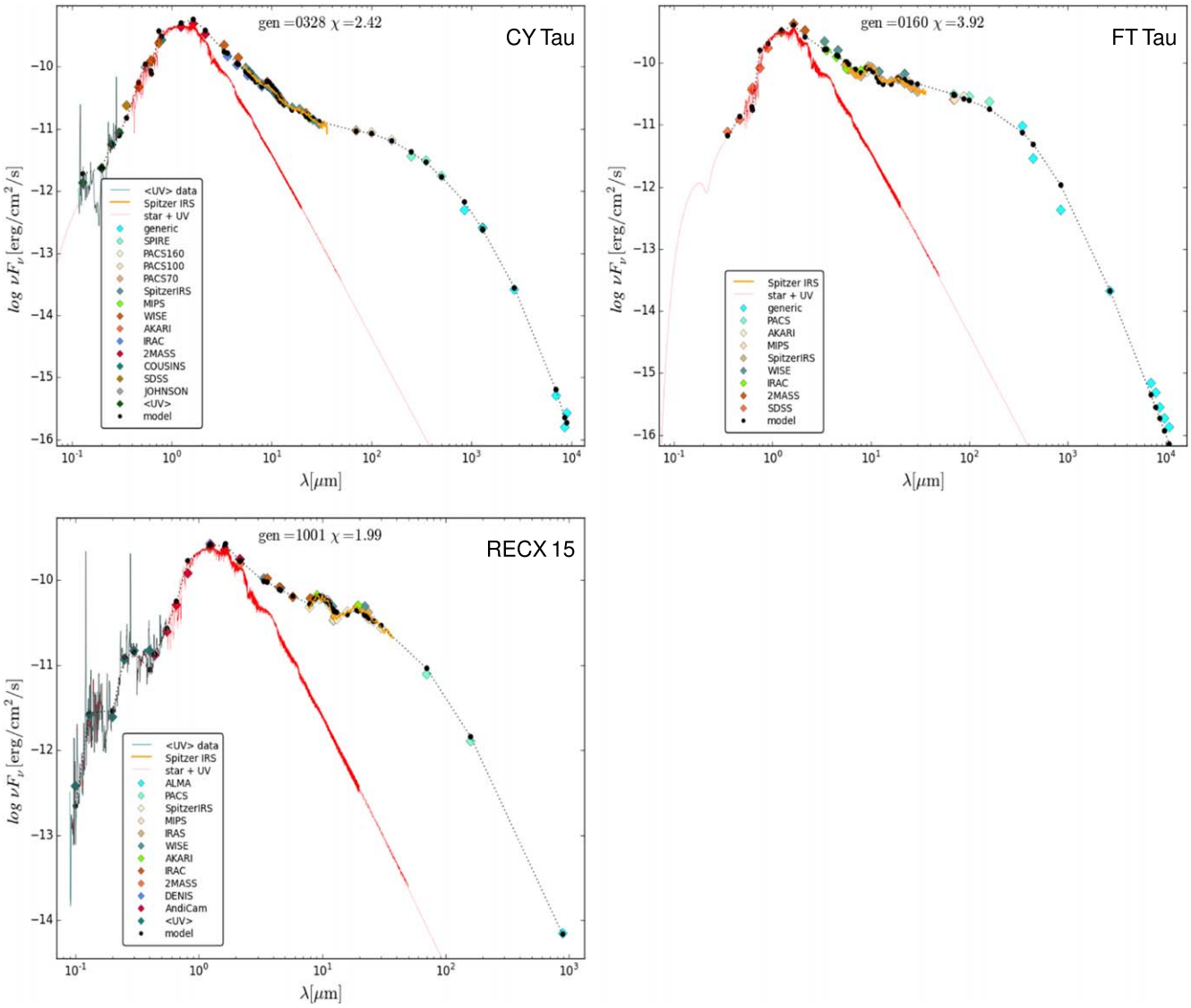

Figure 1. (Continued.)

5. The assumed strength of turbulence in the disk $\alpha_{\rm settle}$ counteracting dust settling. This value is treated as a global parameter throughout all disk zones.
6. The minimum and maximum radius ($a_{\rm min}$, $a_{\rm max}$) and the powerlaw index of the size distribution function $a_{\rm pow}$ of the grains in each zone.
7. The volume fraction of amorphous carbon (amC) in the grains, treated as global parameter throughout all disk zones. The other two dust volume contributors $Mg_{0.7}Fe_{0.3}SiO_3$ (60%) and porosity (25%) are scaled to reach 100% altogether. The values in brackets are for default choice amC = 15%. The maximum hollow sphere volume fraction is fixed at 80% (not used for fitting).
8. The PAH abundance with respect to interstellar standard $f_{\rm PAH}$ in each zone, and the ratio of charged PAHs (global parameter) in case the PAHs are included in the fit. We fix the kind of PAHs to circumcoronene with 54 carbon and 18 hydrogen atoms in all disk models.

Altogether, we have hence $2 + 3 + 1 + 2 + 1 + 3 + 1 = 13$ free parameters for a single-zone SED model without PAHs, 15 free parameters for a single-zone model including PAHs, 21 free parameters for a two-zone model without PAHs, and 24 free parameters for a two-zone model including PAHs. In practice, however, the actual number of these parameters is smaller. It is more or less impossible, for example, to determine the radial extension of a disk by SED-fitting. Therefore, $R_{\rm out}$

Table 2
Type of SED-fitting Model, Number of Free Parameters, Generations Completed and Models Calculated, and Final Fit Quality

Object	# Disk Zones	PAHs Fitted?	# Free Parameters	# Data Points	# Generations	# Models	Final χ
HD 100546	2	Yes	16	120	632	7584	1.85
HD 97048	2	Yes	16	119	1124	13488	1.65
HD 95881	2	Yes	14	69	114	1368	1.67
AB Aur	2	Yes	13	140	533	6396	3.37
HD 163296	2	Yes	15	116	887	10644	1.91
49 Cet	2	–	14	65	n.a.	n.a.	2.43
MWC 480	1	Yes	10	80	713	8556	2.30
HD 169142	2	Yes	15	126	1039	12468	2.41
HD 142666	2	Yes	19	80	1401	16812	1.91
HD 135344B	2	Yes	15	58	141	1692	3.33
V 1149 Sco	2	Yes	17	72	665	7980	2.40
Lk Ca 15	2	–	14	65	1006	12072	2.05
USco J1604-2130	2	–	15	45	703	8436	2.58
RY Lup	2	–	15	47	601	7212	3.42
CI Tau	2	Yes	13	61	682	7448	2.18
TW Cha	1	–	9	47	n.a.	n.a.	2.01
RU Lup	1	–	8	63	172	2064	2.78
AA Tau	1	–	9	49	n.a.	n.a.	2.67
TW Hya	2	–	13	63	3031	36372	2.35
GM Aur	2	–	14	72	1004	12048	2.97
BP Tau	1	Yes	9	60	343	4116	2.11
DF Tau	1	–	9	64	n.a.	n.a.	3.20
DO Tau	1	–	9	63	456	5472	1.94
DM Tau	2	–	13	64	n.a.	n.a.	2.43
CY Tau	2	Yes	14	65	333	3996	2.41
FT Tau	1	–	9	51	179	2148	3.92
RECX 15	1	Yes	8	56	1018	12216	1.99

Note. Objects marked with "–" have no detections of PAH features, so PAHs are not included in the radiative transfer. "n.a." = not recorded.

and γ are rather estimated or values are taken from the literature, but are not varied during the SED-fitting stage. The same is true for ϵ in the outer disk which we would rather fix to a default value of one, because it has very little influence of the SED. In consideration of two-zone disks, some parameters may be chosen to be global, i.e., not zone-dependent. All these operational decisions are left to the modeler's responsibility, in consideration of known facts about the object under discussion. Our general strategy was to first try a single-zone disk model, and only if that resulted in a poor fit, we needed to repeat the fitting exercise with a two-zone model. In cases where the object is well-known to have a gap (pre-ALMA era), the disk was treated by a two-zone model in the first place. Table 2 summarizes these choices in terms of the number of radial disk zones assumed, whether PAH properties have been part of the fitting or not (only attempted when PAH features are detected), and what was the total number of free parameters (average is 13 ± 3). Small numbers of parameters and/or generations indicate that we had a good SED-fitting model to start with from previous works. Large χ-values indicate that incompatible observational data was used for the fit (some data points might not agree with others within the errorbars) rather than a failed fit. This list demonstrates that a fully automated SED-fitting is impossible. We need to decide which disk parameters can be fitted by the available observations, and which cannot, and here human interference is unavoidable.

To save computational time, we have converted all low-resolution spectra into small sets of monochromatic points and added those to the photometric data (see Figure 1). The spectral fluxes are then only computed for these wavelengths by RT. These model fluxes are always a bit noisy due to the application of MC methods, which produces noise both in the temperature determination phase and flux calculation phase. The fit quality of an SED-fitting model χ^2 is computed according to Equation (3), but we first calculate χ^2 separately in spectral windows, for example [0, 0.3] μm, [0.3, 1] μm, [1, 3] μm, etc., and then average those results. This procedure makes sure that all spectral regions have an equal influence of the fit quality, even if the distribution of measurement points is unbalanced in wavelength space.

The SED-fitting models are relatively fast. One RT model with `MCFOST` needs about 5–10 minutes on 6 CPU-cores, allowing us to complete about 150–1500 generations (1800–18,000 models) per target to find a good fit to all photometric and spectroscopic data, including the *Spitzer* PAH and silicate emission features. The same genetic fitting

algorithm was used as explained in Section 3.1. However, a thorough determination of the errorbars of our results, for example by applying the Markov Chain Monte Carlo (MCMC) method, is already quite cumbersome in the SED-fitting stage. Since we have about 15 free parameters, we would need to run hundreds of thousands of disk models to sample all relevant regions of the parameter space, which would correspond to about 5×10^5 CPU-hours or 20,000 CPU-days. Even if we had 100 processors available to us at all times, we would still need to wait for more than half a year to finish one of our SED-fitting models with errorbars. We therefore decided that we do not have the resources to perform such an analysis. The uncertainties in our determinations of disk properties are roughly estimated in Appendix B.

The obtained SED-fits are visualized in Figure 1 with enlargements of the mid-IR region including the 10 and 20 μm silicate features and the PAH emission bands in Figure 35 of Appendix C. The SED-fits obtained are very convincing. The detailed mid-IR spectra, which are plotted on a linear scale in Figure 35, show some shortcomings of our global fitting strategy. Of course, one could subtract "the continuum" and use more free parameters for the dust properties (mix of materials, crystalline/amorphous, dust size and shape distribution → opacity fitting), to get a better fit for this limited wavelength region, but such a model would not be applicable to the entire SED and would not serve DIANA's purpose of determining the disk shape and dust properties as preparation for the thermo-chemical models. Our aim is to fit all available data by a single model for each object, with a minimum set of free parameters, here four parameters for the kind and size distribution of dust grains, and two parameters for the PAHs. And in this respect we think that our results are actually quite remarkable as they broadly capture the observed wavelength positions and amplitudes of the spectral variations in many cases. The observations obtained with different instruments can also show some ambiguities, with issues due to different fields of view or variability of the objects. On the chosen linear scale, one can also start to see the noise in the MC models. The resulting parameters and physical disk and PAH properties are continued to be discussed in Section 4.

3.3. Modeling Step 3: Thermo-chemical Disk Models (DIANA Standard Models)

Pure SED-fitting is well-known to suffer from various degeneracies, which can only be resolved by taking into account additional types of observational data. These degeneracies are often grounded in certain physical effects; for example:

1. The outer disk radius has very little influence on the SED. In order to determine the radial extension of the dust in a disk, continuum images or visibilities at (sub)mm wavelengths have to be taken into account.
2. To determine the radial extension of the gas, we need (sub-)mm molecular observations, preferably spatially resolved maps or line visibilities. However, already the fluxes and widths of (sub-)mm lines, such as low-J rotational CO lines, contain this information.
3. There is a degeneracy between lacking disk flaring and strong dust settling. Both physical mechanisms lead to a flat distribution of dust in the disk, hence to very similar observational consequences for all continuum observations. However, dust settling leaves the vertically extended gas bare and exposed to the stellar UV radiation, leading to higher gas temperatures and stronger gas emission lines in general, hence the opposite effect on the strengths of far-IR emission lines (Woitke et al. 2016). By taking into account mid or far-IR line flux observations, we can break this degeneracy.
4. More transparent dust in the UV, for example by changing the size-distribution parameters of the dust grains, leads to enhanced gas heating and line formation, but has only little influence on the appearance of the dust at longer wavelengths. This is an important degree of freedom in our models to adjust the emission line fluxes, whereas the effects on the continuum appearance are rather subtle and can be compensated for by adjusting other, for example disk shape parameters.
5. A tall inner disk zone can efficiently shield the outer disk from stellar UV and X-ray photons. Such shielding reduces gas heating and emission lines coming from an outer disk.

The final step of our data analysis is therefore to run full radiation thermo-chemical models with an enlarged set of continuum and line observations. This is the core of the project, involves running full `ProDiMo` models, and is by far the computationally most demanding task. Most published works on fitting gas properties of disks have fixed the disk dust structure after SED-fitting (multi-stage models, see Section 1), and only adjusted a few remaining gas parameters (such as the dust-to-gas ratio or the element abundances) and chemical rate-networks to fit the line observations. Our ambitious goal in the DIANA project was *not* to do that. From our experience with the dependencies of predicted line observations as function of dust properties and disk shape, freezing the spatial distribution and properties of the dust grains may be not suitable for fitting line observations, because these properties matter the most for the gas emission lines. The details of our thermo-chemical models are explained in Woitke et al. (2016), Kamp et al. (2017), which we summarize here as follows:

1. usage of detailed UV and X-ray properties of the central stars to determine the chemical processes in the disk after detailed UV RT and X-ray extinction in the disk,
2. physical description of dust settling by balancing upward turbulent mixing against downward settling, resulting in changes of the dust structure when the gas properties are altered,
3. consistent use of PAH abundance in continuum RT, gas heating and chemistry,
4. the same element abundances in all disks and in all disk zones (values from Table 5 in Kamp et al. 2017),
5. fixed isotope ratios $^{13}C/^{12}C = 0.014$, $^{18}O/^{16}O = 0.0020$ and $^{17}O/^{16}O = 0.00053$ for all disks, no isotope selective photodissociation,
6. fixed dust-to-gas ratios in each zone before dust settling, value can depend on object and on disk zone,
7. small chemical rate network (about 100–200 species) with freeze-out, thermal and photodesorption (Kamp et al. 2017), but no surface chemistry other than H_2 formation on grains (Cazaux & Tielens 2004, 2010),
8. chemical concentrations are taken from the time-independent solution of the chemical rate-network (no time-dependent models).
9. the same standard H_2 cosmic ray ionization rate ($1.7 \times 10^{-17}\,s^{-1}$) and the same background interstellar UV field strength ($\chi_{ISM} = 1$) for all objects.

Or fitting approach was to use the SED-fitted models as starting points in parameter space, but then to continue varying the dust and disk shape parameters, along with a few additional gas parameters, as we fit an enlarged set of line and continuum observations. All continuum observations used before remain part of the fit quality χ^2. The additional observational data include continuum images and visibilities, line fluxes, line velocity profiles and integrated line maps, see Table 3. For each of these observations we evaluate a fit quality by calculating additional χ^2_{type}, which are then added together to form the overall model χ^2:

$$\chi^2 = w_{phot}\,\chi^2_{phot} + w_{spec}\,\chi^2_{spec} + w_{image}\,\chi^2_{image} + w_{line}\,\chi^2_{line}, \tag{8}$$

where the weights w_{type} of the different types of observations are chosen by the modeler and are normalized to $w_{phot} + w_{spec} + w_{image} + w_{line} = 1$. The fit quality of the photometric data χ^2_{phot} is calculated as in Equation (3). χ^2_{spec} is computed in the same way by summing up the differences between $\log F^{model}_{\lambda_i}$ and $\log F^{obs}_{\lambda_i}$ on all wavelength points λ_i given by the observational spectrum, after reddening and interpolation in the model spectrum. Concerning the image data, we have averaged the 2D-intensity data in concentric rings, resulting in radial intensity profiles. The model images are treated in the same way as the observations after rotation and convolution with the instrument point-spread function (PSF). We then apply again Equation (3) to obtain χ^2_{image}. The definition of our χ_{line} is special and depends on the available data. We first compute χ^2_{flux} for one line by comparing the model and observed line fluxes according to Equation (3). If the full width half maximum (FWHM) of the line has been measured, we also compute

$$\chi^2_{FWHM} = \left(\frac{FWHM^{mod} - FWHM^{obs}}{\sigma_{FWHM}}\right)^2. \tag{9}$$

If velocity profiles are available, we use again Equation (3) to compute χ^2_{velo}, and if a line map is available (converted to a radial line intensity profile by averaging over concentric rings), we use Equation (3) to calculate χ^2_{map}. Finally, these components are added together to compute

$$\chi^2_{line,k} = \begin{cases} \chi^2_{flux} & \text{if only line flux is observed} \\ \frac{1}{2}\,\chi^2_{flux} + \frac{1}{2}\,\chi^2_{FWHM} & \text{if line flux and FWHM are observed} \\ \frac{1}{2}\,\chi^2_{flux} + \frac{1}{2}\,\chi^2_{velo} & \text{if line flux and line profile are observed} \\ \frac{1}{3}\,\chi^2_{flux} + \frac{1}{3}\,\chi^2_{velo} + \frac{1}{3}\,\chi^2_{map} & \text{if line flux, profile and a map are observed,} \end{cases}, \tag{10}$$

where, for the total χ^2_{line}, we still need to average over all observed lines k in the data set. Our final choices how to fit each line for each object are recorded in the individual `LINEobs.dat` files, which is contained, for example for DM Tau, in http://www-star.st-and.ac.uk/~pw31/DIANA/DIANAstandard/DMTau_ModelSetup.tgz. Therefore, our χ^2 is not the result of a sound mathematical procedure. We have to carefully select and review the data, to see whether the data quality is sufficient to include them in our fit quality, and we have to carefully assign some weights to compensate the different numbers of points associated with each kind of data. For example, a line flux is one point, a line profile is composed of maybe 10–20 points, but a low resolution spectrum may contain hundreds of data points.

Table 3
DIANA Standard Models for 14 Disks

Object	Chemistry	Visc.Heat.?	# Free Para.	N_{phot}	N_{spec}	N_{image}	N_{lines}	N_{widths}	N_{velo}	N_{maps}	Final χ
HD 97048	Small	No	21	41	4	–	37	–	–	–	0.99
AB Aur	Large	Yes	22	69	6	4	65	28	3	1	1.87
HD 163296	Small	Yes	23	69	4	2	35	5	4	4	1.01
MWC 480	Large	No	10	44	2	2	32	8	4	2	9.0[a]
HD 169142	Small	No	14	30	4	–	2	2	–	–	3.28
HD 142666	Small	No	13	32	1	1	11	1	1	–	1.41
Lk Ca 15	Large	No	20	48	2	–	14	8	8	–	2.24
USco J1604-2130	Small	No	20	18	1	–	4	–	–	–	1.35
TW Hya	Large[b]	Yes	22	34	2	1	48	12	3	3	1.43
GM Aur	Small	No	n.a.[c]	55	1	–	18	–	–	–	3.67
BP Tau	Small	Yes	21	34	2	–	6	3	3	1	1.39
DM Tau	Large	No	21	32	2	2	13	2	2	2	0.92
CY Tau	Small	Yes	18	30	1	1	7	5	5	3	1.94
RECX 15	Small	Yes	16	26	1	–	10	1	2	–	0.84

Notes. See Table 2 for the (unchanged) model setup concerning number of disk zones and inclusion of PAHs in radiative transfer. N_{phot} = number of selected photometric data points. N_{spec} = number of low-resolution spectra, for example *Spitzer*/IRS, *Herschel*/PACS, *Herschel*/SPIRE, *ISO*/SWS or *ISO*/LWS. N_{image} = number of continuum images or visibility data files, for example from NICMOS, SUBARU, SMA, ALMA or MIDI. N_{lines} = number of observed line fluxes (including upper limits). N_{velo} = number of high-resolution line velocity profiles, for example VLT/CRIRES, SMA, ALMA, and two NIRSPEC observations probing full series of CO fundamental lines for BP Tau and CY Tau. N_{maps} = number of spatially resolved line data sets, converted to line-integrated intensity profiles, for example SMA, ALMA. More details about the data, object by object, are given in Section 4.5.
[a] Mismatch of NICMOS-image at $\lambda = 1.6$ μm destroys the otherwise fine fit for MWC 480, possibly a problem related to the variability of the object.
[b] In the TW Hya model, D, D^+, HD and HD^+ have been included as additional species to predict the detected HD 1–0 line at 112 μm.
[c] Value not recorded (hand-fitted model).

In addition to the parameters of our SED-fitting disk models listed in Section 3.2 (the dust-to-gas ratio is listed there already) we have only the two following additional free model parameters for the gas in the DIANA standard models:

1. the efficiency of exothermal reactions (global parameter) γ_{chem}, see Woitke et al. (2011) for explanations,
2. the abundance of PAHs with respect to the gas f_{PAH} in each zone (only a new parameter when not yet included in the SED-fitting model).

All other gas and chemical parameters are fixed throughout the project, in particular the element abundances. However, there are two choices to be made for each object:

3. Choice of the size of the chemical rate network, either the small or the large DIANA-standard chemical setup (Kamp et al. 2017). The small network has 12 elements and 100 molecules and ice species, whereas the large network has 13 elements and 235 molecules and ice species.
4. Choice whether or not viscous heating is taken into account as additional heating process, according to a fixed published value of the accretion rate $\dot{M}_{acc}$.

Concerning option 3, the small DIANA chemical standard can be used if line observations are available only for atoms and common molecules like CO and H_2O. If larger and more complicated molecules are detected such as HCN or HCO^+, the large DIANA chemical standard is recommended. Option 4 turned out to be essential to explain some strong near-IR and mid-IR emission lines detected from objects with high $\dot{M}_{acc}/M_{disk}$ values. We compute the total heating rate of an annulus at distance r in [erg cm^{-2} s^{-1}] according to Equation (2) in D'Alessio et al. (1998),

$$F_{vis}(r) = \frac{3\,GM_\star \dot{M}_{acc}}{8\pi r^3}\left(1 - \sqrt{\frac{R_\star}{r}}\right), \tag{11}$$

and distribute this amount of heat in the vertical column [erg cm^{-3} s^{-1}] as

$$\Gamma_{vis}(r, z) = F_{vis}(r)\frac{\rho(r, z)^p}{\int_0^\infty \rho(r, z')^p\, dz'}, \tag{12}$$

where $p = 1$ leads to unstoppable heating at high altitudes where cooling tends to scale as $\propto\rho^2$. We avoid this problem by setting $p = 1.25$ as global choice. In the passive disk models discussed in this paper, the dust energy balance is assumed not to be affected by accretion, only the gas is assumed to receive additional heat via the action of viscosity and accretion.

Thermo-chemical disk models which obey the rules and assumptions listed above and in Section 3.2 are henceforth called the *DIANA standard models*. We have not changed these assumptions throughout the project as we continued to fit the

models for more and more targets. This procedure was highly debated among the team members, as certain new modeling ideas might have helped to improve the fits of some objects. However, for the sake of a uniform and coherent disk modeling, we finally agreed to keep the modeling assumptions the same for all objects.

One typical radiation thermo-chemical model, including Monte Carlo RT, requires about 1–3 hr on 6 processors (6–18 CPU hours), depending on the size of the spatial grid, the size of the chemical rate network, and the quantity and kinds of observational data to be simulated. We have used the SED-fitted models as starting points for the DIANA standard models, mostly using the same genetic fitting algorithm as explained in Section 3.1. However, some team members preferred to fit just by hand. The number of free parameters used during this final fitting stage also largely depended on the judgment of the modeler, see Table 3. Some team members decided to fix as many as possible disk parameters as determined during the SED-fitting stage, such as the inner disk radius, the charge and abundances of the PAHs, or the dust masses in the different disk zones. Other team members decided to leave more parameters open, for example the dust size distribution, the disk shape and the dust settling parameters. In such cases, of course, the continuum RT must be re-computed. In particular, the disk extension and tapering-off parameters can be adjusted to sub-mm line observations, dust settling and disk flaring can be disentangled, and the shape of the inner disk, which is usually only little constrained by the SED, can be fitted to visibility and, for example, to CO rovibrational line data. The convergence of each fit was manually monitored, and decisions about data (de-)selection and fitting weights sometimes needed to be revised on the fly. Again, all these decisions cannot be automated, they need human expertise.

Computing 300 generations with 12 children per generation requires 3600 DIANA standard models, which can be calculated in about 20,000–65,000 CPU hours per object. This was at the limit of the computational resources available to us. Our results are probably not unique and likely to be influenced by the initial parameter values taken from the SED-fitting models. It is probably fair to state that our computational resources only allowed us to find a χ^2 minimum in the neighborhood of the SED-fitting model in parameter space. Running MCMC models to determine errorbars was not feasible.

4. Results

The full results of our SED-fitting models are available at http://www-star.st-and.ac.uk/~pw31/DIANA/SEDfit and the full results of the DIANA-standard models are available at http://www-star.st-and.ac.uk/~pw31/DIANA/DIANAstandard. These files include all continuum and line observations used, the fitted stellar, disk and dust parameters, the resulting 2D physico-chemical disk structures, including dust and gas temperatures, chemical concentrations and dust opacities, and all files required to re-setup the models and run them again for future purposes. Details about the content of these files can be found in Appendix A.

We offer these results to the community for further analysis, and as starting points to interpret other or maybe to predict new observations. It is not our intention in this paper to discuss all results in a systematic way. We rather want to show a few interesting properties found for some individual objects, and to highlight a few trends and results for the overall ensemble of protoplanetary disks considered. The resulting UV and X-ray properties of the central stars, derived from modeling step 1, are discussed in Section 4.1, the disk dust masses obtained from modeling step 2 are shown in Section 4.2, and the dust properties and mm-slopes are discussed in Section 4.3, as well as the resulting PAH properties in Section 4.4, before we turn to the results of the individual DIANA standard models in Section 4.5.

4.1. UV and X-Ray Stellar Properties

The strength and color of the UV and X-ray irradiation have an important influence on the chemistry, heating and line formation in the disk. The details about the UV and X-ray data used and methods applied are explained in (Dionatos et al. 2019). Considering the total UV flux between 91.2 and 205 nm (see Table 1), the Herbig Ae/Be stars are found to be about 10^4 times brighter, but this is mostly photospheric, soft UV radiation. If one focuses on the hard UV from 91.2 to 111 nm, which can photodissociate H_2 and CO, the Herbig Ae/Be stars are only brighter by a maximum factor of about 100. Concerning soft X-rays, there is hardly any systematic difference between the T Tauri and Herbig Ae stars, and for hard X-rays between 1 and 10 keV, the brightest X-ray sources are actually the T Tauri stars RY Lup, RU Lup, AA Tau. We note that DM Tau is also identified as a strong X-ray source with an unextincted X-ray luminosity of about 3×10^{30} erg s^{-1} for energies >0.1 keV. Earlier *Chandra* observations (Güdel et al. 2007) only showed 1.8×10^{29} erg s^{-1}, but then later, XMM observations (Güdel et al. 2010) resulted in a much higher unextincted X-ray luminosity of 2×10^{30} erg s^{-1} for energies >0.3 keV, which is consistent with 3×10^{30} erg s^{-1} for energies >0.1 keV. We would like to emphasize again that the UV and X-ray luminosities listed in Table 1 are not the observed values, but are the luminosities as seen by the disk, assuming that the extinction between the emitting source and the disk is small.

4.2. Disk Dust Masses

The dust masses of protoplanetary disks are classically derived from the observation of (sub-)mm continuum fluxes

Table 4
Total Dust Masses $M_{\rm dust}$ [$10^{-4}\,M_\odot$] in the SED-fitting Models Compared to the Values Derived from the Spectral Flux F_ν at $\lambda = 850\,\mu$m

Object	$M_\star$ ($M_\odot$)	d (pc)	F_{850} (Jy)	$\langle T_{\rm dust}\rangle$ (K)	$\langle\kappa_{850}^{\rm abs}\rangle$	$M_{\rm dust}^{\rm class}$	$M_{\rm dust}^{\rm derived}$	$M_{\rm dust}^{\rm model}$	$M_{\rm disk}/M_\star$
HD 100546	2.5	103	1.41	56.1	4.69	2.67	0.710	0.708	0.28%
HD 97048	2.5	171	2.02	34.9	2.42	10.6	8.75	13.20	5.3%
HD 95881	2.5	171	0.0346	131	7.93	0.181	0.0122	0.394	0.16%
AB Aur	2.5	144	0.585	29.7	2.85	2.17	1.79	2.20	0.88%
HD 163296	2.47	118	1.93	30.1	6.00	4.86	1.88	5.29	2.1%
49 Cet	2.0	59.4	0.0173	58.7	4.78	0.011	0.0027	0.0028	0.0014%
MWC 480	1.97	137	0.748	19.7	5.96	2.51	1.49	2.18	1.1%
HD 169142	1.8	145	0.607	38.3	9.36	2.28	0.445	0.581	0.32%
HD 142666	1.6	116	0.307	26.8	3.78	0.740	0.512	0.840	0.53%
HD 135344B	1.65	140	0.552	34.3	7.74	1.94	0.511	0.602	0.37%
V 1149 Sco	1.3	145	0.209	27.6	4.46	0.785	0.447	0.761	0.59%
Lk Ca 15	1.0	140	0.425	11.6	5.70	1.49	1.57	3.53	3.53%
USco J1604-2130	1.2	145	0.190	26.4	8.02	0.716	0.237	0.376	0.31%
RY Lup	1.38	185	0.210	29.1	4.93	1.29	0.627	2.05	1.5%
CI Tau	0.9	140	0.371	22.9	12.2	1.30	0.326	1.19	1.32%
TW Cha	1.0	160	0.125	14.2	8.70	0.570	0.323	1.02	1.0%
RU Lup	1.15	150	0.479	41.8	4.94	1.93	0.654	3.09	2.7%
AA Tau	0.85	140	0.176	28.6	7.23	0.617	0.209	1.31	1.5%
TW Hya	0.75	51	1.52	23.1	11.1	0.705	0.193	0.889	1.2%
GM Aur	0.7	140	0.681	17.9	3.78	2.44	2.47	11.1	16%
BP Tau	0.65	140	0.131	16.7	10.5	0.460	0.184	0.701	1.1%
DF Tau	1.17	140	0.0077	32.4	3.78	0.027	0.015	0.020	0.020%
DO Tau	0.52	140	0.346	37.3	7.92	1.21	0.287	0.721	1.4%
DM Tau	0.53	140	0.251	10.2	9.42	0.878	0.642	1.63	3.1%
CY Tau	0.43	140	0.193	9.3	6.69	0.676	0.762	10.0	23%
FT Tau	0.30	140	0.310	19.7	9.16	1.09	0.421	3.03	10%
RECX 15	0.28	94.3	0.0023	64.8	11.8	0.0036	0.0033	0.0038	0.0014%
mean value[a]				27.7	6.32				0.72%

Notes. Uncertainties are discussed in Appendix B. $M_{\rm dust}^{\rm class}$, $M_{\rm dust}^{\rm derived}$ and $M_{\rm dust}^{\rm model}$ are listed in units [$10^{-4}\,M_\odot$]. F_{850} is the spectral flux at 850 μm taken from the SED-fitting models. The dust mass $M_{\rm dust}^{\rm class}$ is calculated from F_{850}, using the classical Equation (13) with standard values for opacity $\kappa_{850}^{\rm abs} = 3.5$ cm^2/g (dust) and mean dust temperature $\langle T_{\rm dust}\rangle = 20$ K (Andrews & Williams 2005). $M_{\rm dust}^{\rm derived}$ is also derived from Equation (13), but using the proper opacities and mass-averaged dust temperatures $\langle T_{\rm dust}\rangle$ as found in the SED-fitting models. $M_{\rm dust}^{\rm model}$ is the actual dust mass in the model. The mass-mean dust absorption opacities $\langle\kappa_{850}^{\rm abs}\rangle$ are listed in units [cm^2/g(dust)]. $M_{\rm disk} = M_{\rm dust}^{\rm model} \times 100$ is assumed here.
[a] Logarithmic mean value = exp($\langle$ log.$\rangle$).

(e.g., Andrews & Williams 2005), using some well-established values for the dust absorption opacity and mean dust temperature. Our results show that this method can have large uncertainties because of the unknown mean dust temperature in the disk, the unknown dust opacities, and the particular behavior of cold disks (see also Section 5.3.3 in Woitke et al. 2016). If the disk is entirely optically thin at frequency ν, and if all grains in the disk are warm enough to emit in the Rayleigh–Jeans limit, the observable spectral flux F_ν is given by

$$F_\nu = \frac{2\nu^2 k}{c^2\,d^2}\,\langle T_{\rm dust}\rangle\,M_{\rm dust}\,\kappa_{850}^{\rm abs}, \qquad (13)$$

where ν is the frequency, c is the speed of light, d the distance, k the Boltzmann constant, $\langle T_{\rm dust}\rangle$ the mass-averaged dust temperature in the disk, and $\kappa_{850}^{\rm abs}$ the absorption coefficient per dust mass [cm^2 g^{-1}] at 850 μm, here assumed to be constant throughout the disk. Equation (13) is widely used in the literature to measure total dust masses of protoplanetary disks (e.g., Andrews & Williams 2005), and then drawing conclusions about the disk gas mass by assuming $M_{\rm disk} = 100 \times M_{\rm dust}$.

Table 4 shows a comparison between the actual dust masses in the SED-fitting models ($M_{\rm dust}^{\rm model}$), and the results that would be obtained if Equation (13) was applied to the 850 μm flux ($M_{\rm dust}^{\rm class}$). In many cases, the two dust mass results are fairly similar, however, there are deviations of up to a factor of 15 for individual objects. In fact, Table 4 shows that Equation (13) *is not valid*, because if we use the actual, proper mass averaged dust temperatures and opacities used in the models, $\langle T_{\rm dust}\rangle$ and $\langle\kappa_{850}^{\rm abs}\rangle$, the agreement is worse and shows a systematic offset with respect to $M_{\rm dust}^{\rm model}$ (Figure 2). There are three effects we need to understand in order to explain this behavior. (1) Our mean dust opacities are usually larger than 3.5 cm^2 g^{-1}, which

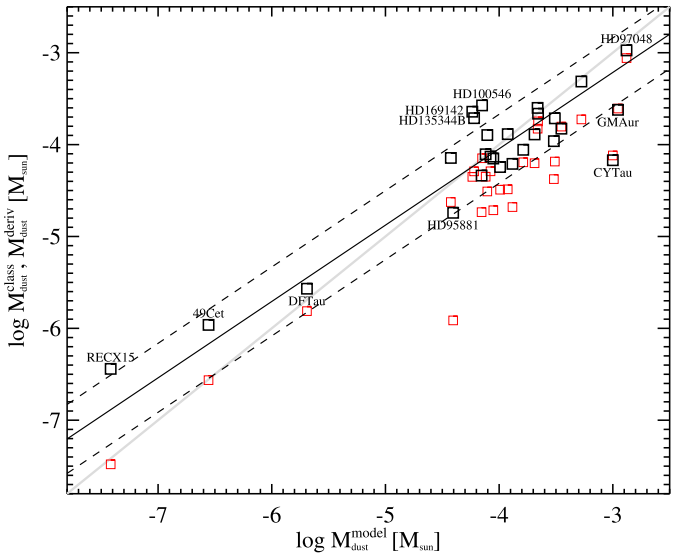

Figure 2. Black squares show the dust masses $M_{\rm dust}^{\rm class}$ computed from the 850 μm flux using the classical method (standard opacity of 3.5 cm^2/g(dust), dust temperature of 20 K) vs. the actual dust masses $M_{\rm dust}^{\rm model}$ used in the SED-fitting models to produce those fluxes. The black full and dashed lines show a linear fit to these data (Equation (14)). The red squares show the dust masses $M_{\rm dust}^{\rm derived}$ derived in the classical way, but using the proper mean dust opacities and mean dust temperatures present in the models.

(A color version of this figure is available in the online journal.)

generally leads to lower dust masses at fixed 850 μm flux. (2) Many disks are not optically thin at 850 μm, which leads to higher dust masses at fixed flux. (3) Small or tenuous disks can be much warmer than 20 K, but massive extended disks can also be much cooler than 20 K. Those cool disks have very cold midplane regions, which emit less than in the Rayleigh–Jeans limit at 850 μm. Consequently, such cold disks need to be more massive in order to produce a certain given 850 μm flux. To explain the deviations between $M_{\rm dust}^{\rm class}$ and $M_{\rm dust}^{\rm model}$, mechanism (3) is actually the most significant one. All three effects superimposed lead to roughly $M_{\rm dust}^{\rm class} \approx M_{\rm dust}^{\rm model}$, but cause an uncertainty of about 0.5 dex, see Figure 2. A linear fit results in

$$\log_{10} M_{\rm dust}\,[M_\odot] = (0.87 \pm 0.45) + (1.20 \pm 0.11)\log_{10} M_{\rm dust}^{\rm class}\,[M_\odot]. \quad (14)$$

This leads us to the following important conclusion. For warm disks, such as the Herbig Ae/Be in general, and HD 100546 and HD 169142 in particular, the classical method tends to overestimate the dust masses. In contrast, cold T Tauri disks, such as CY Tau and DM Tau, might be much more massive than previously thought. Using the classical dust mass determination method, observations tentatively indicate a linear correlation between disk dust mass with stellar mass (e.g., Andrews et al. 2013; Mohanty et al. 2013; Pascucci et al. 2016), but also report on significant scatter with deviations of up to a factor of 100. In our rather small sample such a relation is not obvious. Our sample also includes a debris disk (49 Cet) and a strongly truncated disk (RECX 15). However, in summary, our derived disk mass–stellar mass ratios are well within the observed ranges and are consistent with a mean mass ratio of about 1%.

4.3. Dust Properties, and the mm-slope

Table 5 shows the results from our SED-fitting work concerning the mm-slope, generally considered as important indicators for grain size, dust growth and disk evolution, see e.g., Natta et al. (2007) and Testi et al. (2014). However, the material composition of the grains, in particular the inclusion of conducting materials like, in our case, amorphous carbon, can have an important influence on the opacity mm-slope, too. Min et al. (2016b) have shown that if conducting materials are included, dust aggregate opacity computations, using the discrete dipole approximation, result in shallow opacity slopes in the millimeter regime even for small grains, known as the "antenna effect." This behavior can be reproduced by using Mie computations with effective medium theory and a DHS (Min et al. 2016b). The dust size distributions in our SED-fitted models typically ranges from a few 0.01 μm to a few millimeters, with power-law exponents between about 3.2 and 4.0, with two outliers CI Tau and FT Tau and a mean value of about 3.7. The amorphous carbon volume fraction is found to be about 10%–25%.

The observable SED-slope $\alpha_{\rm SED}$ and the dust opacity slope $\beta_{\rm abs}$ are given by

$$\alpha_{\rm SED} = -\frac{d\log F_\nu}{d\log\lambda}, \quad (15)$$

$$\beta_{\rm abs} = -\frac{d\log \kappa^{\rm abs}}{d\log\lambda}. \quad (16)$$

For optically thin disks, which are warm enough to emit in the Rayleigh–Jeans limit (where Equation (13) holds), the following equation is valid

$$\alpha_{\rm SED} = \beta_{\rm abs} + 2. \quad (17)$$

Table 5 shows results from our SED-fitting models where we know $\beta_{\rm abs}$ and can measure in how far Equation (17) is valid. We consider the mm-slope by using the wavelength interval 0.85–1.3 mm, and the cm-slope by using wavelengths 5–10 mm. Steep SEDs can be explained either by the complete absence of millimeter-sized dust grains (small $a_{\rm max}$ such as 0.1 mm for HD 97048) or by a steep dust size distribution function (large size distribution powerlaw index $a_{\rm pow} > 3.9$ as for AB Aur and GM Aur). However, both explanations require in addition that the amorphous carbon volume fraction is small (amC $< 10\%$). To break this degeneracy, additional continuum and line observations have to be taken into account. For example, amC is crucial for the dust albedo in the near-IR, and thereby controls the primary heating of the dust in the disk

Table 5
Dust Opacity and SED-slopes in the Millimeter and Centimeter Regimes as Affected by Dust Input Parameters and Disk Mean Temperatures

Object	$a_{\rm min}(\mu{\rm m})$	$a_{\rm max}(\mu{\rm m})$	$a_{\rm pow}$	amC	$\langle T_{\rm dust}\rangle$(K)	$\beta_{\rm abs}^{\rm mm}$	$\alpha_{\rm SED}^{\rm mm}$	$\Delta^{\rm mm}$	$\beta_{\rm abs}^{\rm cm}$	$\alpha_{\rm SED}^{\rm cm}$	$\Delta^{\rm cm}$
HD 100546	0.042	2980	3.34	16.8%	56.1	0.90	2.69	−0.20	1.33	3.30	−0.03
HD 97048	0.054	96	3.49	8.2%	34.9	1.93	3.48	−0.45	1.71	3.69	−0.02
HD 95881	0.046	3030	3.67	18.8%	131	1.06	2.07	−0.99	–	–	–
AB Aur	0.026	4560	3.92	8.2%	29.7	1.55	3.31	−0.24	1.71	3.46	−0.25
HD 163296	0.052	10000	3.80	17.4%	30.1	1.16	2.41	−0.75	1.44	3.06	−0.38
49 Cet	0.037	1260	3.20	15.6&	58.7	0.93	2.76	−0.17	–	–	–
MWC 480	0.020	4280	3.62	18.9%	19.7	1.05	2.56	−0.49	–	–	–
HD 169142	0.046	6510	3.76	22.4%	38.3	1.01	2.63	−0.39	1.21	3.19	−0.02
HD 142666	0.082	10000	3.53	17.6%	26.8	0.93	2.39	−0.54	1.19	2.95	−0.24
HD 135344B	0.05	5440	3.73	19.7%	34.3	1.05	2.81	−0.24	1.35	3.30	−0.05
V 1149 Sco	0.003	4950	3.78	12.5%	27.6	1.31	2.69	−0.62	1.57	3.55	−0.02
Lk Ca 15	0.005	2570	3.60	14.5%	11.6	1.20	2.30	−0.90	1.83	3.38	−0.45
USco J1604-21	0.014	44	3.02	21.4%	26.4	1.59	3.17	−0.42	1.54	3.52	−0.02
RY Lup	0.004	3880	3.62	13.4%	29.1	1.15	2.36	−0.79	1.54	3.10	−0.43
CI Tau	0.084	1990	4.24	23.4%	22.9	1.35	2.40	−0.95	1.49	3.36	−0.13
TW Cha	0.075	5650	3.55	25.0%	14.2	0.76	1.90	−0.86	–	–	–
RU Lup	0.051	4620	3.52	15.0%	41.8	0.98	2.29	−0.80	1.35	2.79	−0.56
AA Tau	0.42	1120	3.67	13.9%	28.6	1.29	2.36	−0.93	–	–	–
TW Hya	0.11	6650	3.99	23.0%	23.1	1.22	2.23	−0.99	1.32	2.98	−0.34
GM Aur	0.006	1070	3.99	10.7%	17.9	1.64	2.43	−1.21	1.95	3.88	−0.07
BP Tau	0.078	4290	3.97	22.1%	16.7	1.23	2.09	−1.14	1.44	3.18	−0.27
DF Tau	0.055	3000	3.25	13.7%	32.4	0.94	2.62	−0.32	–	–	–
DO Tau	0.037	7880	3.55	24.9%	37.3	0.74	2.26	−0.48	0.94	2.74	−0.21
DM Tau	0.015	3990	3.70	21.8%	10.2	1.01	2.13	−0.88	1.38	3.24	−0.14
CY Tau	0.076	1540	3.72	14.3%	9.3	1.29	1.48	−1.80	2.26	3.74	−0.52
FT Tau	0.052	8630	4.97	23.8%	19.7	1.43	2.13	−1.30	1.49	3.23	−0.26
RECX 15	0.021	3000	3.47	27.4%	64.8	0.65	2.42	−0.23	–	–	–
mean value	0.034[a]	2820[a]	3.69	18%							

Notes. We list results with up to 3 digits precision in order to discuss the differences Δ. $a_{\rm min}$ and $a_{\rm max}$ are the minimum and maximum dust radii assumed in the (outer disk of the) model, and $a_{\rm pow}$ is the dust size distribution powerlaw index. amC is the volume fraction of amorphous carbon in the dust material, and $\langle T_{\rm dust}\rangle$ the mass averaged dust temperature in the disk. $\beta_{\rm abs}$ is the dust opacity slope according to Equation (16) and $\alpha_{\rm SED}$ the observable log–log flux gradient in the SED, at millimeter (0.85–1.3 mm) and centimeter wavelengths (5–10 mm), respectively. The deviation between expected and actual SED-slope, according to Equation (17), is $\Delta = \alpha_{\rm SED} - (\beta_{\rm abs} + 2)$. HD 95881, 49 Cet, MWC 480, TW Cha, AA Tau, DF Tau and RECX 15 have no cm-data.
[a] Logarithmic mean value = $\exp(\langle \log. \rangle)$.

surface by stellar photons, with large implications on the shape of the SED in the near and mid IR regions.

Interestingly, the deviation from the optically thin warm case (Equation (17)), $\Delta = \alpha_{\rm SED} - (\beta_{\rm abs} + 2)$, can be quite substantial. In the millimeter-region (0.85–1.3 mm), we find the largest deviation to be −1.8 for CY Tau (because it is a very cold disk in the model), followed by −1.3 for FT Tau (because it is a cold and optically thick disk in the model). Deviations between −0.5 and −1.0 are quite typical among our models. Only a few warm and optically thin disks (HD 100546, AB Aur, HD 135344B, RECX 15) have deviations as small as −0.2 to −0.3. For very cold disks like CY Tau, the SED-slope flattens, despite an opacity slope that is relatively steep. These trends continue into the centimeter region, albeit less pronounced. Linear fits to these results lead to

$$\alpha_{\rm SED}^{\rm mm} = (1.72 \pm 0.31) + (0.63 \pm 0.26)\beta_{\rm abs}^{\rm mm}, \qquad (18)$$

$$\alpha_{\rm SED}^{\rm cm} = (1.97 \pm 0.22) + (0.87 \pm 0.15)\beta_{\rm abs}^{\rm cm}. \qquad (19)$$

All millimeter and centimeter modeling results are visualized in Figure 3, together with these linear fits. The coolest disks, showing the largest deviations from the expectations (Equation (17)), gather at the bottom of this plot. The gray line, which visualizes those expectations, is an upper limit to these dependencies. It always overestimates $\alpha_{\rm SED}$ or underestimates $\beta_{\rm abs}$, respectively, depending on what quantity is considered to be given. The deviations are much less pronounced at centimeter wavelengths, but still relevant. We conclude that the determination of dust sizes from the observation of SED-slopes $\alpha_{\rm SED}$ has large principle uncertainties. This analysis may already fail in its first step, namely the determination of $\beta_{\rm abs}$, because disks may be partly optically thick and too cold to allow for the application of the Rayleigh–Jeans approximation, so the problem becomes nonlinear. Other unknowns, such as the impact of amorphous carbon or other

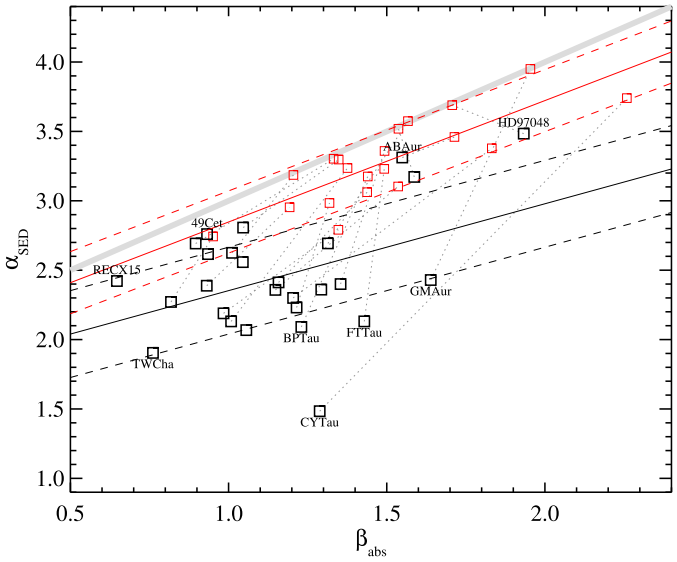

Figure 3. Black squares show the millimeter SED-slopes α_{SED}^{mm} as function of the dust opacity slopes β_{abs}^{mm} that we used in the models to produce those SED-slopes. The black full and dashed lines show a linear fit to these results (Equation (19)). The red squares show the same for centimeter wavelength. The expectation $\alpha_{SED} = \beta_{abs} + 2$ for a warm, optically thin disk is shown by a thick gray line.
(A color version of this figure is available in the online journal.)

conducting materials on the opacity slope, can affect the second analysis step as well, namely the determination of dust sizes from β_{abs}.

4.4. PAH Properties

The results of our simultaneous fits of the the dust and PAH properties in the disks to the SED and mid-IR spectral data are summarized in Table 6. Small PAHs with 54 carbon atoms ("circumcoronene") are sufficient to explain the observations, with abundances $f_{PAH} \approx 0.005$–0.8, i.e., somewhat under-abundant with respect to standard interstellar medium (ISM) conditions ($10^{-6.52}$ PAH molecules/H-nucleus), which agrees with the results of Geers et al. (2007, 2009). We note, however, that our analysis is based on full RT disk models. In all cases where a couple of different PAH bands are detected (HD 100546, HD 97048, HD 95881, AB Aur, HD 169142, HD 142666) we find a mean PAH charge of about 0.6–0.98, but see no clear trend of PAH charge with disk gaps as reported by Maaskant et al. (2014).

4.5. DIANA Standard Models

We computed full DIANA-standard disk models for 14 objects, see Table 7. Full information about the fitted stellar, disk shape, dust and gas parameters, the full 2D modeling results and predicted observations are available at http://www-star.st-and.ac.uk/~pw31/DIANA/DIANAstandard. The corresponding data products are described in Appendix A. The collected observational data can also be downloaded from http://www.univie.ac.at/diana.

In the following pages, we highlight a few results for each object. The figures show the fitted disk density structures, the surface density profiles of dust and gas, and a few selected graphical comparisons between observed and predicted line properties, followed by the complete list of observed and modeled line properties. The SED-plots are not repeated here, as they are very similar to those shown in Figure 1, although, admittedly, χ^2_{phot} and χ^2_{spec} usually increased slightly as we started fitting the images and lines, too. This is a natural consequence of including more data into the fit quality (see Equation (8)). In cases where the genetic fitting algorithm started to actually loose the SED fit, the program was stopped and re-run with larger weights w_{phot} and w_{spec}. Full information about the final choice of fitting weights is

Table 6
Properties of Polycyclic Aromatic Hydrocarbon Molecules (PAHs) in 14 SED-fitting Models[a]

Object	f_{PAH}[b]	M_{PAH}/M_{dust}	⟨PAH-charge⟩[c]
HD 100546	0.0028	3.7(−5)	0.89
HD 97048	0.42	5.5(−3)	0.63
HD 95881	0.36	4.8(−3)	0.61
AB Aur	0.40	5.3(−3)	0.90
HD 163296	0.050	6.6(−4)	0.80
MWC 480	0.1[d]	1.3(−3)[d]	1[d]
HD 169142	0.77	1.0(−2)	0.98
HD 142666	0.050	6.6(−4)	0.70
HD 135344B	0.2[d]	2.7(−3)[d]	1[d]
V 1149 Sco	0.5	6.6(−3)	1
CI Tau	0.1[d]	1.3(−3)	0[d]
BP Tau	0.3[d]	4.0(−3)	0[d]
CY Tau	0.007[d]	8.9(−5)	0[d]
RECX 15	0.0005[d,e]	3.4(−4)[d,e]	0[d]

Notes. All models use the spectral properties of circumcoronene with 54 carbon atoms and 18 hydrogen atoms, with a constant mixture of charged and neutral opacities.
[a] Only objects with detected PAH features are listed. There are two well-known "PAH-sources" (HD 97048, HD 169142) which show a number of very prominent PAH features, see Figure 35. However, many other objects do have at least one PAH band detected, which allows us to determine some PAH properties as well.
[b] f_{PAH} is the PAH concentration with respect to hydrogen nuclei, normalized to standard conditions in the ISM, i.e., $f_{PAH} = 1$ means that PAHs are as abundant in the disk as in the standard ISM ($10^{-6.52}$ PAH molecules/H-nucleus Tielens 2008). $f_{PAH} \propto M_{PAH}/M_{dust} \cdot \delta$, with δ being the dust/gas mass ratio.
[c] The mean PAH charge is the mixing ratio between charged and (neutral + charged) PAHs, 0 means all PAHs neutral, 1 means all PAHs charged.
[d] Only one PAH band was detected, or the spectroscopic data are of too poor quality to perform a detailed analysis including the PAH-charge. The PAH-charge is assumed in those cases.
[e] The model for RECX 15 has a very peculiar gas/dust mass ratio of 5200. The PAH/dust mass ratio is comparable to the other objects listed.

Table 7
Disk Shape, Dust Opacity and PAH Parameters of the DIANA Standard Models[a]

	ABAur	HD 163296	MWC 480	HD 169142	HD 142666	GMAur	TWHya
$M_\star$ [$M_\odot$]	2.50	2.47	1.97	1.80	1.60	0.70	0.75
$T_{\rm eff}$ [K]	9550	9000	8250	7800	7050	4000	4000
$L_\star$ [$L_\odot$]	42.1	34.7	13.7	9.8	6.3	0.60	0.24
$\dot{M}_{\rm acc}$[b] [$M_\odot$ yr^{-1}]	1.4(−7)	4.5(−7)	–	–	–	–	1.5(−9)
Dust and PAH parameters							
$a_{\rm min}$ [μm]	0.047	0.020	0.020	0.046	0.057	0.050	0.0011
$a_{\rm max}$[c] [mm]	7.5	8.2[c]	4.3	6.5	2.8	3.0	5.7
$a_{\rm pow}$	4.00	3.71	3.62	3.76	3.33	3.84	3.99
amC [%]	5.0%	6.0%	18.9%	22.4%	25.0%	15.0%	24.9%
$\alpha_{\rm settle}$	1.0(−3)	6.6(−3)	7.3(−5)	3.8(−3)	2.8(−3)	1.0(−1)	5.2(−3)
$f_{\rm PAH}$[c]	0.061	0.076	0.1	0.77[c]	0.05	0.01	0.081[c]
PAH$_{\rm charge}$[d] [%]	73%	1.1%	100%	97.6%	0%	–	–
Inner disk zone							
$R_{\rm in}$ [au]	0.46	0.41	–	0.10	0.10	0.19	0.078
$R_{\rm taper}$ [au]	–	–	–	–	–	–	–
$R_{\rm out}$ [au]	88	3.7	–	5.0	10.3	5.0	4.6
Gas mass [$M_\odot$]	4.2(−4)	1.3(−4)	–	7.9(−7)	6.8(−6)	1.0(−7)	1.1(−6)
Dust mass [$M_\odot$]	6.8(−7)	1.5(−9)	–	7.9(−9)	6.8(−8)	1.0(−9)	1.3(−9)
Gas/dust	618	86667	–	100	100	100	847
Col. dens. ϵ	1.28	1.11	–	1.38	0.12	0.90	−0.78
Tapering γ	–	–	–	–	–	–	–
H @ 1 au [au]	0.092	0.077	–	0.035	0.20	0.036	0.028
Flaring β	0.99	1.00	–	0.80	1.15	1.22	1.21
Outer disk zone							
$R_{\rm in}$ [au]	88	3.7	0.28	22	10.3	20.0	4.6
$R_{\rm taper}$ [au]	174	133	100	140	53	100	48
$R_{\rm out}$[e] [au]	680	488	474	457	344	521	192
Gas mass [$M_\odot$]	1.9(−2)	5.8(−1)	2.2(−2)	5.8(−3)	3.3(−3)	3.3(−2)	4.5(−2)
Dust mass [$M_\odot$]	1.8(−4)	1.7(−3)	2.2(−4)	5.8(−5)	3.3(−5)	3.3(−4)	1.0(−4)
Gas/dust	106	341	100	100	100	100	450
Col. dens. ϵ	0.72	0.95	0.66	1.0	1.0	1.3	1.52
Tapering γ	0.54	0.2	0.66	0.50	1.0	0.8	0.45
H @ 100 au [au]	16.8	6.5	12.3	9.6	10.0	8.0	6.3
Flaring β	0.95	1.11	1.10	1.07	1.15	1.21	1.21

	BPTau	DMTau	CYTau	RECX15	LkCa15	USco J1604-2130	HD 97048
$M_\star$ [$M_\odot$]	0.65	0.53	0.43	0.28	1.00	1.20	2.50
$T_{\rm eff}$ [K]	3950	3780	3640	3400	4730	4550	10000
$L_\star$ [$L_\odot$]	0.89	0.23	0.36	0.091	1.20	0.76	39.4
$\dot{M}_{\rm acc}$[b] [$M_\odot$ yr^{-1}]	2.8(−8)	–	7.5(−9)	1.0(−9)	–	–	–
Dust and PAH parameters							
$a_{\rm min}$ [μm]	0.049	0.019	0.050	0.019	0.0067	0.015	0.024
$a_{\rm max}$[c] [mm]	3.1	4.5	3.0	1.6	2.2[c]	0.040	0.037
$a_{\rm pow}$	3.97	3.73	3.68	3.46	3.64	2.90	3.42
amC [%]	17.2%	19.0%	12.0%	22.2%	14.8%	21.4%	17.4%
$\alpha_{\rm settle}$	6.0(−5)	2.1(−3)	6.4(−5)	1.0(−4)	2.2(−4)	2.3(−3)	5.9(−2)
$f_{\rm PAH}$[c]	0.12	0.1	0.009	0.0009	0.014	0.0074[c]	0.42[c]
PAH$_{\rm charge}$[d] [%]	100%	0%	0%	0%	0%	100%	63%
Inner disk zone							
$R_{\rm in}$ [au]	0.060	0.98	0.035	0.028	0.1	0.044	0.33
$R_{\rm taper}$ [au]	–	–	–	1.8	–	–	–
$R_{\rm out}$ [au]	1.3	12.5	0.72	7.5	10.0	0.050	7.18

Table 7
(Continued)

	ABAur	HD 163296	MWC 480	HD 169142	HD 142666	GMAur	TWHya
Gas mass [$M_\odot$]	7.1(−7)	1.2(−6)	6.4(−7)	1.3(−4)	1.9(−8)	1.8(−9)	1.5(−6)
Dust mass [$M_\odot$]	6.9(−9)	1.2(−8)	6.3(−9)	3.5(−8)	1.9(−10)	1.8(−11)	9.8(−9)
Gas/dust	103	100	102	3715	100	100	153
Col. dens. ϵ	0.52	−0.81	0.38	0.53	1.34	0.42	1.29
Tapering γ	–	–	–	0.31	–	–	–
H @ 1 au [au]	0.12	0.42	0.098	0.14	0.11	0.10	0.02
Flaring β	1.22	0.60	1.01	1.24	1.50	1.02	1.16
Outer disk zone							
R_{in} [au]	1.3	12.5	4.2	–	40.1	46.4	62.6
R_{taper} [au]	32	149	58	–	205	56	76
R_{out} [e] [au]	166	570	220	–	400	165	650
Gas mass [$M_\odot$]	6.4(−3)	1.6(−2)	1.2(−1)	–	2.2(−2)	2.1(−3)	9.9(−2)
Dust mass [$M_\odot$]	1.4(−4)	2.7(−4)	1.2(−3)	–	2.8(−4)	4.0(−5)	5.3(−4)
Gas/dust	46	59	100	–	80	53	187
Col. dens. ϵ	0.65	0.50	0.11	–	0.95	0.73	0.87
Tapering γ	0.67	0.50	−0.34	–	−0.93	0.036	0.94
H @ 100 au [au]	7.1	6.0	7.7	–	4.0	19.9	5.9
Flaring β	1.12	1.17	1.15	–	1.12	1.21	1.19

Notes.
[a] amC is the volume fraction of amorphous carbon in the dust material, ϵ is the column density powerlaw index, γ is the powerlaw index for outer disk tapering, H is the scale height, β the flaring index. For further explanations of the parameter symbols see Woitke et al. (2016). Numbers written $A(-B)$ mean $A \times 10^{-B}$.
[b] The mass accretion rate $\dot{M}_{acc}$ enters the model via an additional heating rate for the gas. Entries "–" mean that this heating process was not included (passive disk model).
[c] In the outer disk zone. Parameters not marked with [b] are assumed to be unique throughout the disk.
[d] "–" indicates that PAH emission features are not detected, hence PAHs are not included in the RT, but they still have an influence on the model because of the photoelectric heating by PAHs.
[e] Where the hydrogen nuclei particle density reaches 10^{20} cm^{-2}.

contained in the downloadable `ModelSetup.tgz` files, see `Parameter.in`.

4.5.1. AB Aur

AB Aur is one of the best studied Herbig Ae/Be disks. Low-resolution spectral data are available (see Figure 1) from about 1 μm (SpeX/Infrared Telescope Facility), over *ISO*/SWS, *Spitzer*/IRS, *ISO*/LWS and *Herschel*/PACS, all the way up to about 400 μm (*Herschel*/SPIRE). Our data collection comprises four continuum images: NICMOS 1.1 μm (Perrin et al. 2009), SUBARU/CIAO H-band (Fukagawa et al. 2004), SUBARU/COMICS 25 μm (Honda et al. 2010), and archival SMA 850 μm data. In addition, we have 69 line fluxes, three line velocity profiles, and one line image (CO 3–2 from SMA). However, both continuum and line data are partly confused by the massive envelope around AB Aur, seen as "nebulosity" in the optical. Although observers have tried to carefully disentangle disk emission and envelope emission/absorption, the observational data is often puzzling. For example, concerning the ^{12}CO 2–1 and ^{13}CO 2–1 lines as published by Fuente et al. (2010, their Figure 2(b)) and (Guilloteau et al. 2013, their Table 3), respectively, the ^{12}CO 2–1 line seems weaker than the ^{13}CO 2–1 line, which no disk model can explain.

Given these observational uncertainties, our 2D disk model for AB Aur (Figure 4) provides a reasonable fit to a surprisingly large number of continuum and line observations by a simple two-zone disk model with a discontinuity around 80 au; this model does not include any envelope component. The disk model manages to explain the huge near-IR excess (about 9 $L_\odot$) by scattering and thermal re-emission from a tall inner disk. The equally impressive mid and far-IR excess (together about 10 $L_\odot$) are caused by an even taller outer disk starting outside of about 80 au. Together, these two disk zones result in a relative height $z/r \approx 0.5$ where the radial optical depth in the visual approaches one, i.e., the disk starts to obscure the star already at inclination angles $i \gtrsim 63°$. Note however, that the specific disk structure resulting from the fitting procedure could be partially biased by the fact that we did not include an envelope component.

The gas/dust ratio is found to be close to 100 in this model with a total disk mass of about 0.019 $M_\odot$ (close to the value 0.022 $M_\odot$ obtained from the pure SED-fit, see Table 4). Figure 5 shows that the fit of the CO rovibrational line flux data is

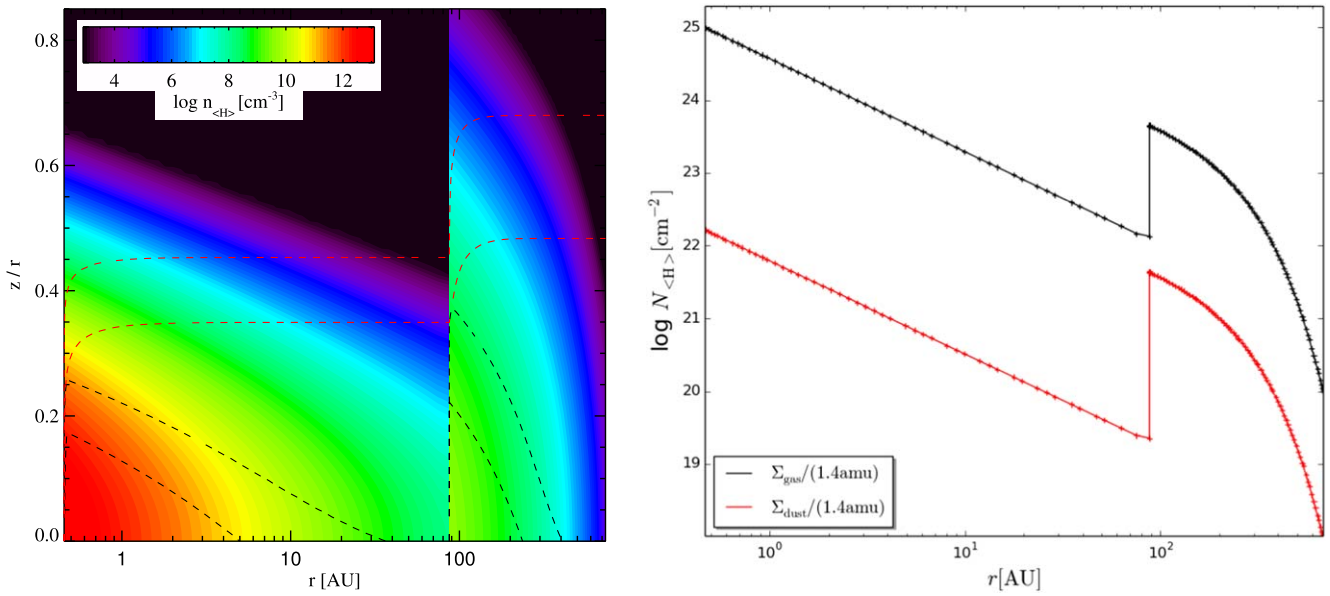

Figure 4. Left contour plot shows the gas density structure of AB Aur in the model with overplotted optical depth contours corresponding to radial $A_V = 0.01$ and $A_V = 1$ (dashed red), and vertical $A_V = 1$ and $A_V = 10$ (dashed black). The right plot shows the dust (red) and gas (black) column densities. The plus signs illustrate the distribution of radial grid points in the disk model.
(A color version of this figure is available in the online journal.)

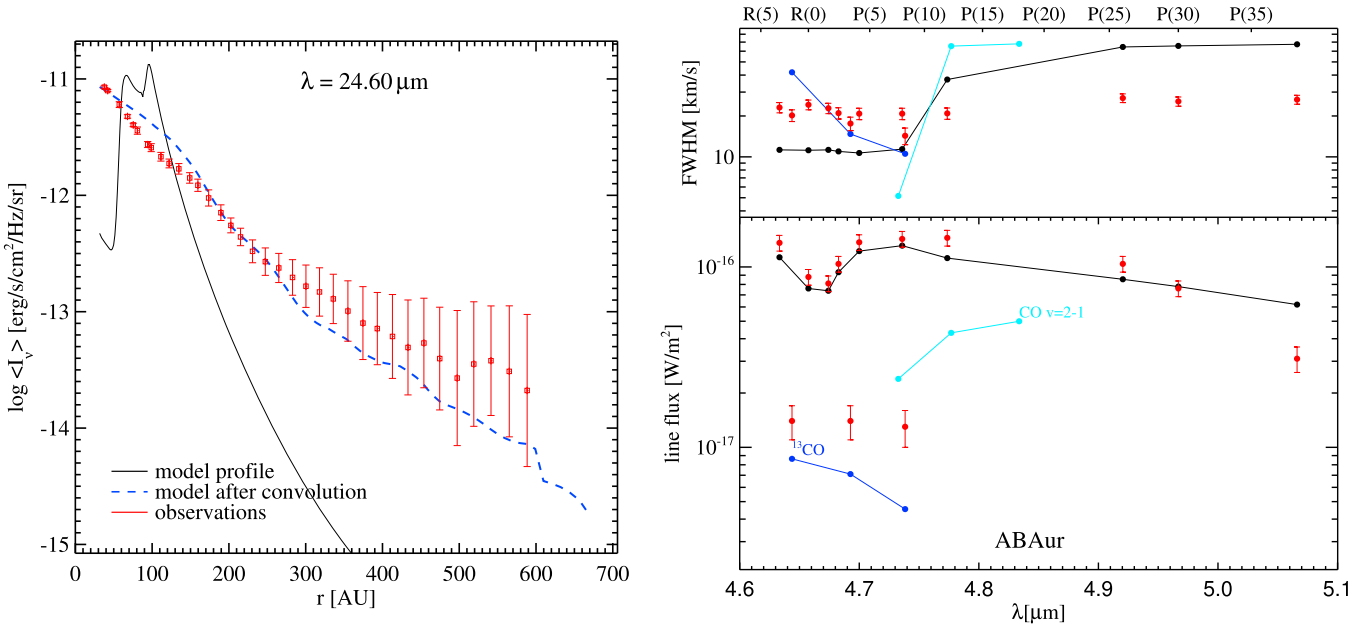

Figure 5. Left: fit of mid-IR radial intensity profile of AB Aur at 25 μm. The model (black full line) is rotated and convolved with the instrument PSF (blue dashed line) before comparing it to the SUBARU data (red errorbars). Right: results for the CO rovibrational lines, with the FWHM plotted on top and line fluxes below. Dots and lines show the model results (CO $v = 1$–0 in black, CO $v = 2$–1 in cyan and ^{13}CO $v = 1$–0 in blue color), and red dots and errorbars are the measurements.
(A color version of this figure is available in the online journal.)

excellent, although the measurements of the FWHM show that two disk zones with sharp inner edges cannot fully explain the CO rovibrational observations. In our model, the CO emission region switches from the outer disk (FWHM $\approx 10\,\mathrm{km\,s^{-1}}$) to the inner disk (FWHM $\approx 50\,\mathrm{km\,s^{-1}}$) around $P(10)$.

Table 8 shows that the [O I] 63 μm line is too strong in the model by a factor $\sim$3, and some of the far-IR emission lines (e.g., high-J CO) are somewhat too strong as well, whereas the OH lines are fine. The results for the sub-mm and mm-lines are a bit diverse, probably due to the aforementioned observational issues with cloud absorption. ^{12}CO 3–2 (866.963 μm), HCO^+ (3361.334 and 1120.478 μm), ^{13}CO 2–1 (1360.227 μm), o-H_2CO (1419.394 and 1328.291 μm) and CS (2039.834 μm) lines are in good agreement with the observations (better than a factor 2.5), but the ^{12}CO 2–1 line (1300.403 μm) is a factor 6.3 too strong, probably due to cloud issues; see Table 8.

4.5.2. HD 97048

HD 97048 is a well-studied Herbig group I disk. It has an inner cavity of 34 $\pm$ 4 au derived from Q-band imaging (T-ReCS on the Gemini South telescope, Maaskant et al. 2013). In addition, a small optically thick inner disk (0.3–2.5 au) is required to fit the strong near-IR excess in the SED. Our best fit model has a similar geometry, albeit slightly different radial zones (inner disk from 0.3 to 7.18 au, outer disk starting at 62.6 au (Figure 6). The differences can arise from the choice of dust opacities (e.g., different $a_{\rm min}$, $a_{\rm max}$ and composition). Recent spatially resolved ALMA data at 302 and 346 GHz are consistent with an inner cavity of $\sim$50 au (Walsh et al. 2016).

HD 97048 has been observed with the VISIR instrument in the PAH band at 8.6 μm (Lagage et al. 2006). Our flaring angle of $\beta = 1.19$ is slightly smaller than the one inferred from the VISIR image ($\beta = 1.26 \pm 0.05$). The surface scale height found from the VISIR PAH image is 51.3 au at 135 au distance from the star. Our model has a gas scale height of 8.43 au at 135 au, and typical factors between the gas scale height and the surface scale height are of the order of three to five. So our best disk model agrees with this within a factor $\sim$2.

Both [O I] fine structure lines at 63 and 145 μm were detected with *Herschel*/PACS (Meeus et al. 2012) and our model reproduces those fluxes within 30% (Table 9). Figure 7 shows that the modeled CO ladder (high J lines) agrees quite well with the observed one (Meeus et al. 2012; Fedele et al. 2013; van der Wiel et al. 2014). The CH^+ emission from our model is a factor 30 fainter than the detected *Herschel*/PACS flux (Fedele et al. 2013). Thi et al. (2011) showed that CH^+ emission in HD 100546 originates from the surface of the inner wall of the outer disk and this holds also for our disk model of HD 97048.

Since the construction of this DIANA model, CO rovibrational line fluxes were measured by van der Plas et al. (2015). For the $v = 1$–0 band, they range from $\sim 10^{-16}\,\mathrm{W\,m^{-2}}$ (low J) to $\sim 10^{-17}\,\mathrm{W\,m^{-2}}$ (high J). Our model has values a factor $\sim$10 smaller. The rovibrational emission originates largely in the inner disk ($\sim$75%), but partially also in the inner wall of the outer disk.

Also, new sub-mm data became available from APEX and ALMA. Foreground extinction causes the total flux of CO $J = 1$–0 and $J = 3$–2 as observed with ALMA ($74.28 \pm 0.14\,\mathrm{Jy\,km\,s^{-1}}$ and $8.22 \pm 0.28\,\mathrm{Jy\,km\,s^{-1}}$) to be a lower limit (van der Plas et al. 2017) and makes the line profiles difficult to fit; the $J = 3$–2 flux is close to that of Hales et al. (2014) who reported $1.4\,\mathrm{K\,km\,s^{-1}}$ (resulting in $2.13 \times 10^{-19}\,\mathrm{W\,m^{-2}}$ using a beam efficiency of 0.6 and the APEX beam size of 18″). Our model underpredicts the ALMA HCO^+ flux by a factor $\sim$7. However, our model used the small chemical network presented in Kamp et al. (2017) which does not fully capture the HCO^+ chemistry. With the large chemical network, HCO^+ line fluxes increase typically by a factor 3–4 (Kamp et al. 2017), which would bring our HD 97048 model closer to the observed value.

The ALMA CO $J = 3$–2 data of HD 97048 (van der Plas et al. 2017) suggests an even larger gas disk ($R_{\rm out} \sim 820$ au) than used in our model. They also show that CO and HCO^+ gas extends inside the dust cavity of this disk, which could have an effect on the CH^+ and CO rovibrational line fluxes (see above) and bring them closer to the observed values. Based on the strong tapering outer edge of our current disk model, we predict large differences in emitting size (85% of radial flux) between the three isotopologue $J = 2$–1 lines of ^{12}CO, ^{13}CO and C^{18}O of 430, 370, and 290 au and flux ratios of 6 and 3.02 for ^{12}CO/^{13}CO and ^{13}CO/C^{18}O. This can be tested with high spatial resolution ALMA data. To summarize, the disk model should be refined in the future using the wealth of existing and upcoming ALMA data.

4.5.3. HD 163296

HD 163296 is a bright isolated Herbig Ae star with a large and apparently almost perfectly symmetric Keplerian disk. The object has ALMA science verification continuum data partly shown in Figure 8, and line data partly shown in the lower row of plots in Figure 9. Our data collection includes a number of low resolution spectra (*ISO*/SWS, *Spitzer*/IRS, *Herschel*/PACS and *Herschel*/SPIRE), two (sub-)mm ALMA continuum images (band 6 and 7), 36 line observations and four ALMA line maps with derived intensity profiles. HD 163296 also has an almost complete coverage of observed CO line observations, from $J = 2$–1 at 1.3 mm up to $J = 36$–35 at 72.8 μm, the so-called CO spectral line energy distribution (SLED), Figure 8.

The model (see Figure 10) follows a pattern we have already seen before. A tall inner disk casts a shadow onto a massive, cold and mildly flaring outer disk with tapered outer edge (Figure 10). The model also suggests a large depletion of dust in the inner disk. The model provides an excellent SED-fit, and

Table 8
Derived Physical Properties of the Disk Model and Comparison of Computed Spectral Line Properties with Observations from ABAur.properties

DIANA Standard Fit Model Properties	
Minimum dust temperature [K]	21
Maximum dust temperature [K]	1830
Mass-mean dust temperature [K]	36
Minimum gas temperature [K]	26
Maximum gas temperature [K]	23349
Mass-mean gas temperature [K]	54
mm-opacity-slope (0.85–1.3) mm	1.7
cm-opacity-slope (5–10) mm	1.8
mm-SED-slope (0.85–1.3) mm	3.5
cm-SED-slope (5–10) mm	3.6
10 μm silicate emission amplitude	1.6
Naked star luminosity [$L_\odot$]	41.3
Bolometric luminosity [$L_\odot$]	70.4
Near-IR excess ($\lambda = 2.01$–6.82 μm) [$L_\odot$]	8.56
Mid IR excess ($\lambda = 6.82$–29.3 μm) [$L_\odot$]	5.12
Far-IR excess ($\lambda = 29.3$–$999.$ μm) [$L_\odot$]	4.74

Species	λ (μm)	Line Flux (W m^{-2})		FWHM (km s^{-1})		Size(au)
		Observed	Model	Observed	Model	
O I	63.183	8.5 ± 0.2(−16)	2.6(−15)	⋯	4.2	386.2
O I	145.525	4.5 ± 1.5(−17)	1.8(−16)	⋯	3.9	319.6
O I	0.630	9.7 ± 3.0(−16)	1.7(−16)	20.0 ± 2.0	5.7	98.9
C II	157.740	5.1 ± 0.8(−17)	8.1(−17)	⋯	2.7	615.6
C	370.415	5.6 ± 2.8(−18)	1.5(−17)	⋯	2.8	536.6
HCO^+	3361.334	1.4 ± 0.2(−21)	1.1(−21)	4.0 ± 0.5	3.3	338.9
HCO^+	1120.478	4.8 ± 1.0(−20)	9.2(−20)	2.5 ± 0.5	3.4	384.5
CO	866.963	1.0 ± 0.2(−18)	2.7(−18)	3.0 ± 0.5	3.1	577.2
CO	1300.403	1.2 ± 0.2(−19)	7.5(−19)	3.5 ± 0.5	3.1	484.2
^{13}CO	1360.227	2.7 ± 0.2(−19)	2.1(−19)	2.5 ± 0.5	3.1	422.1
$C^{18}O$	1365.430	3.9 ± 0.8(−20)	8.5(−20)	2.5 ± 0.5	3.2	387.7
$C^{17}O$	1334.098	2.0 ± 0.2(−20)	3.6(−20)	2.5 ± 0.5	3.3	371.8
CN	1321.390	3.2 ± 0.3(−21)	8.5(−20)	2.5 ± 0.5	2.5	563.2
o-H_2CO	1419.394	2.6 ± 0.3(−21)	2.9(−21)	2.5 ± 0.5	3.1	415.1
o-H_2CO	1328.291	9.0 ± 0.9(−21)	3.6(−21)	2.5 ± 0.5	3.1	411.3
HCN	1127.520	1.1 ± 0.2(−20)	1.3(−19)	2.5 ± 0.5	2.6	486.5
CS	2039.834	1.8 ± 0.4(−21)	1.8(−21)	2.5 ± 0.5	2.7	515.9
SO	1454.060	1.4 ± 0.3(−21)	1.4(−21)	2.5 ± 0.5	3.6	293.6
SO	1363.006	1.9 ± 0.4(−21)	2.9(−21)	2.5 ± 0.5	3.6	300.3
CO	371.650	3.5 ± 0.3(−17)	3.0(−17)	⋯	3.1	483.9
CO	325.225	4.3 ± 0.4(−17)	4.0(−17)	⋯	3.2	472.6
CO	289.120	4.3 ± 0.4(−17)	5.2(−17)	⋯	3.2	458.5
CO	260.239	4.1 ± 0.4(−17)	6.3(−17)	⋯	3.2	441.5
CO	236.613	4.9 ± 0.5(−17)	7.2(−17)	⋯	3.3	419.9
CO	216.927	3.8 ± 0.4(−17)	7.9(−17)	⋯	3.5	389.2
CO	200.272	4.4 ± 0.5(−17)	8.2(−17)	⋯	3.7	341.0
^{13}CO	388.743	3.8 ± 2.5(−18)	9.5(−18)	⋯	3.2	416.9
^{13}CO	302.414	7.1 ± 4.0(−18)	1.4(−17)	⋯	3.4	384.5
CO	72.842	<3.8(−17)	9.9(−19)	⋯	5.7	97.5
CO	79.359	<3.4(−17)	2.9(−18)	⋯	7.3	95.1
CO	90.162	3.1 ± 0.4(−17)	1.8(−17)	⋯	7.5	78.4
CO	108.762	<4.5(−17)	7.5(−17)	⋯	6.9	80.0
CO	113.457	5.9 ± 1.2(−17)	8.2(−17)	⋯	6.8	81.1
CO	118.580	<4.6(−17)	8.5(−17)	⋯	6.8	82.9
CO	124.193	<3.5(−17)	8.5(−17)	⋯	6.8	86.3
CO	130.368	3.9 ± 0.9(−17)	8.3(−17)	⋯	6.8	106.2
CO	137.196	<2.9(−17)	8.1(−17)	⋯	6.7	129.0
CO	144.784	2.7 ± 0.9(−17)	8.1(−17)	⋯	6.4	150.4

Table 8
(Continued)

Species	λ (μm)	Line Flux (W m^{-2})		FWHM (km s^{-1})		Size(au)
		Observed	Model	Observed	Model	
CO	153.266	4.1 ± 1.4(−17)	8.1(−17)	⋯	5.8	173.9
CO	162.811	<2.7(−17)	8.2(−17)	⋯	4.9	200.4
CO	173.631	6.4 ± 1.6(−17)	8.2(−17)	⋯	4.4	234.1
CO	185.999	<3.0(−17)	8.2(−17)	⋯	4.0	280.8
CO	4.633	1.4 ± 0.2(−16)	1.1(−16)	23.1 ± 2.0	11.3	92.1
CO	4.657	8.8 ± 0.5(−17)	7.6(−17)	24.2 ± 2.0	11.2	92.3
CO	4.674	8.1 ± 0.5(−17)	7.4(−17)	22.8 ± 2.0	11.3	92.3
CO	4.682	1.0 ± 0.2(−16)	9.4(−17)	21.0 ± 2.0	11.0	92.2
CO	4.699	1.4 ± 0.2(−16)	1.2(−16)	20.8 ± 2.0	10.7	92.2
CO	4.735	1.4 ± 0.2(−16)	1.3(−16)	20.8 ± 2.0	11.4	92.3
CO	4.773	1.4 ± 0.2(−16)	1.1(−16)	20.9 ± 2.0	37.1	92.1
CO	4.920	1.0 ± 0.2(−16)	8.5(−17)	27.1 ± 2.0	64.5	1.3
CO	4.966	7.6 ± 0.5(−17)	7.8(−17)	25.6 ± 2.0	65.6	1.1
CO	5.066	3.1 ± 0.5(−17)	6.2(−17)	26.4 ± 2.0	67.4	0.8
^{13}CO	4.643	1.4 ± 0.3(−17)	8.6(−18)	20.2 ± 2.0	42.0	0.5
^{13}CO	4.692	1.4 ± 0.3(−17)	7.1(−18)	17.6 ± 2.0	14.7	95.6
^{13}CO	4.738	1.3 ± 0.3(−17)	4.5(−18)	14.3 ± 2.0	10.5	101.8
OH	65.131	7.0 ± 2.0(−17)	4.0(−17)	⋯	9.4	94.6
OH	65.278	1.2 ± 0.2(−16)	6.0(−17)	⋯	7.2	96.2
OH	71.170	4.5 ± 0.6(−17)	2.2(−17)	⋯	12.1	93.7
OH	71.215	4.5 ± 0.6(−17)	2.6(−17)	⋯	10.3	95.2
OH	79.115	2.5 ± 0.8(−17)	2.4(−17)	⋯	5.9	101.1
OH	79.179	<2.4(−17)	2.4(−17)		6.0	101.2
OH	84.420	1.0 ± 0.1(−16)	5.4(−17)	⋯	7.7	96.2
OH	84.596	1.0 ± 0.1(−16)	7.2(−17)	⋯	7.2	97.7
OH	119.234	2.8 ± 1.4(−17)	3.7(−17)	⋯	7.2	100.5
OH	119.441	3.1 ± 1.4(−17)	4.5(−17)	⋯	7.0	103.8
o-H_2	17.033	6.9 ± 2.6(−18)	1.5(−16)	7.8 ± 1.2	8.5	139.6
p-H_2	12.277	5.6 ± 2.0(−18)	3.7(−17)	8.3 ± 1.2	7.8	113.5
p-H_2	8.025	1.5 ± 0.3(−17)	4.2(−18)	10.4 ± 2.0	6.0	111.0
o-H_2	4.694	9.0 ± 2.0(−18)	4.1(−19)	15.9 ± 2.0	11.1	102.3

Note. The observational data in the second table is given in the form value $\pm\sigma$ for detections, and in the form $<3\sigma$ in case of non-detections. The size in the last column is the radius in the image plane that contains 95% of the flux according to the model.

can explain most of the line observations within a factor two, from CO isotopologue lines over high-J CO and high-excitation water lines to the neutral carbon line at 370 μm. The [O I] 63 μm line is overpredicted by a factor of three, though, and the [N II] line at 205 μm is several orders of magnitude too weak.

The radial continuum and line intensity profiles show that the tapered-edged disk model can, to some extent, naturally explain the somewhat larger extension of the disk in ^{12}CO (sub-) mm lines (∼400 au) as compared to the (sub-)mm continuum (∼200 au), because the CO-lines stay optically thick even at larger radii where the optically thin continuum already vanishes in the background noise. There is no obvious need in this model to introduce a gas/dust ratio that changes with radius, as our model with a constant gas/dust ratio of about 350 in the outer disk zone fits both, the disk extension in mm-continuum and CO lines. However, dust radial migration is expected to result in a changing gas/dust ratio (e.g., Facchini et al. 2017), and closer inspection reveals that the model actually arrived at some kind of compromise. The disk extension of the model is slightly too small in CO lines, and slightly too large in the continuum. An abrupt disappearance of the mm-continuum signal around the outer edge has indeed been reported by de Gregorio-Monsalvo et al. (2013), which can be considered as true evidence for inward radial drift of mm-sized dust particles in HD 163296.

This DIANA-standard model has an unprecedented level of physical consistency and agreement with a large suite of multi-wavelength line and continuum data (Table 10). The outer disk is found to be very massive in this model (0.58 $M_\odot$), the heaviest disk among all DIANA-standard models, with a gas/dust mass ratio of ∼350. This is different from the results of the pure SED-fit, where the disk mass was estimated to be only 0.053 $M_\odot$, see Table 4. The inner disk is also found to be even more gas-enriched (gas/dust ∼85,000), which gives a boost to

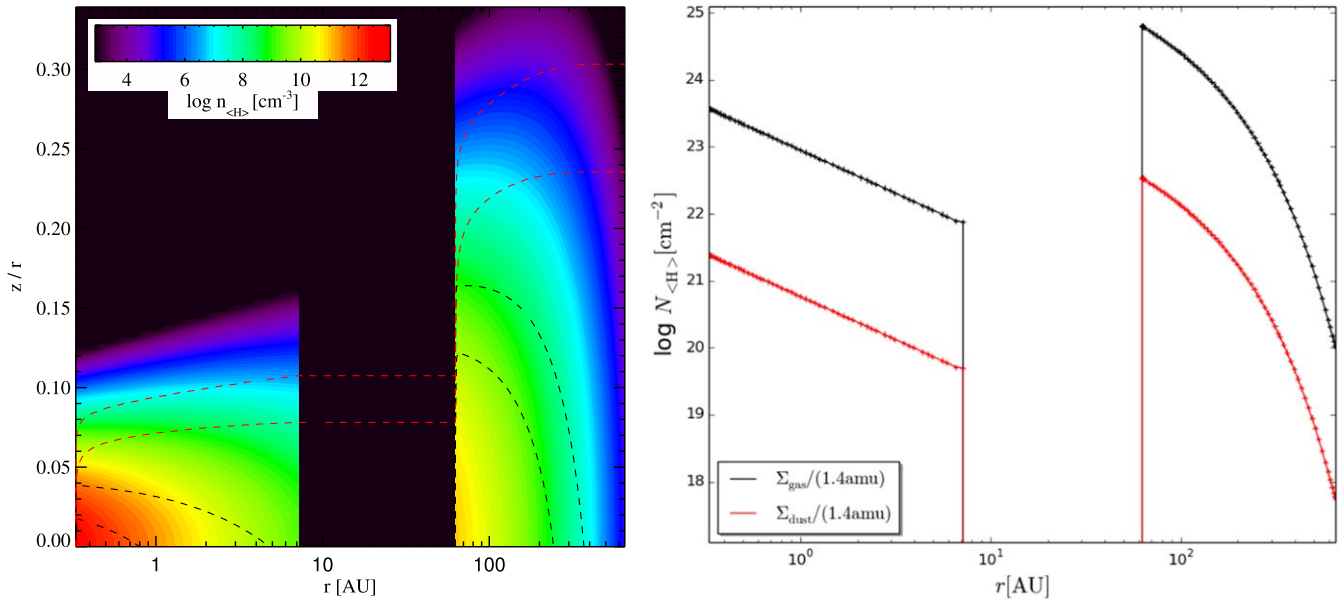

Figure 6. HD 97048 density and surface density plots. For details see Figure 4. (A color version of this figure is available in the online journal.)

all emission lines at shorter wavelength that originate in the inner disk, similar to RECX 15.

The shadow casted by the inner disk hits the outer disk around 200 au in this model, exciting far-IR emission lines in the surface of the outer disk only outside of that radius. This particular geometry leads to the prediction of a ring-like appearance of far-IR emission lines like [O I] 63 μm (lower right panel of Figure 10) and high-J CO lines, which, unfortunately, cannot be resolved by any current instrumentation. These results demonstrate how important the stellar UV irradiation is for the heating and line formation in the model, as both the gas and the dust are assumed to be entirely smooth and continuous around 200 au in the model. Latest VLT/SPHERE and ALMA continuum data, however, show ring-like substructures at 80, 124 and 200 au at millimeter wavelengths, but only the innermost of these in scattered light (Muro-Arena et al. 2018). These new observations have not been included in our data collection for HD 163296.

4.5.4. MWC 480 (HD 31648)

MWC 480 is one of only two DIANA sources where the final fit uses just a single-zone disk model (Figure 11). The SED in Figure 1 can be conveniently fitted with a mildly flared, strongly settled disk, where the near-IR excess of about 3 $L_\odot$ is a natural by-product. The data collection of MWC 480 includes two continuum images (at 850 μm and a NICMOS scattered light image at 1.6 μm), 32 line observations with three velocity-profiles and two line intensity maps. MWC 480 is particularly well-observed in (sub-)mm lines including CO, ^{13}CO, HCO$^+$, CN and HCN, and the model manages to reproduce all these observations, though less convincing for CN and HCN (see Table 11). Figure 12 shows the excellent line flux and profile agreement for the ^{12}CO and HCO$^+$ sub-mm lines. The CO rovibrational line fluxes also fit astonishingly well—for a single-zone model—but the lines are too broad. The high-J CO lines seem a bit too weak, indicating that the disk is not warm enough in the inner regions of the model. Similar conclusions can be drawn from some of the mm-line intensity profiles, where the line signals from the inner disk regions are somewhat too weak. A vertically more extended, less dense inner disk (as for HD 163296, HD 142666, CY Tau) might also improve the fit of some high energy emission lines in the case of MWC 480.

The gas/dust mass ratio was not varied during fitting this model, and the total disk gas mass of 0.022 $M_\odot$ is in accordance with the SED-fit (Table 4). The derived mass value agrees within a factor of three with the values reported in Mannings & Sargent (1997) and Meeus et al. (2012) but are not consistent with the much higher values ($M_{\rm disk} \gtrsim 0.2\,M_\odot$) derived from pure dust modeling by Guilloteau et al. (2011) or Sitko et al. (2008).

A remarkable feature of the MWC 480 disk is its observed variability in the infrared, including the silicate feature. We only focused on one epoch of observational data but we did run several models where we changed the scale height of the disk (a possible origin of the variability, Sitko et al. 2008; Grady et al. 2010) and found that such changes do not have a significant impact on the spectral line emission. Recently Fernandes et al. (2018) proposed dusty outflows/winds as an origin of the infrared variability but also azimuthally asymmetric features in the inner disk (clumps) might play a role

Table 9
Model Properties and Comparison of Computed Spectral Line Properties with Observations from HD97048.properties

DIANA Standard Fit Model Properties	
Minimum dust temperature [K]	13
Maximum dust temperature [K]	1777
Mass-mean dust temperature [K]	36
Minimum gas temperature [K]	16
Maximum gas temperature [K]	18292
Mass-mean gas temperature [K]	38
mm-opacity-slope (0.85–1.3) mm	1.6
cm-opacity-slope (5–10) mm	1.6
mm-SED-slope (0.85–1.3) mm	3.1
cm-SED-slope (5–10) mm	3.6
10 μm silicate emission amplitude	1.8
Naked star luminosity [$L_\odot$]	40.0
Bolometric luminosity [$L_\odot$]	53.9
Near-IR excess ($\lambda = 2.02$–6.72 μm) [$L_\odot$]	2.09
Mid IR excess ($\lambda = 6.72$–29.5 μm) [$L_\odot$]	3.91
Far-IR excess ($\lambda = 29.5$–$991.$ μm) [$L_\odot$]	5.21

Species	λ (μm)	Line Flux (W m^{-2})		FWHM (km s^{-1})		Size (au)
		Observed	Model	Observed	Model	
O I	63.183	1.6 ± 0.1(−15)	1.6(−15)	⋯	5.1	349.0
O I	145.525	6.6 ± 0.3(−17)	8.5(−17)	⋯	4.9	321.3
C II	157.740	1.1 ± 0.3(−16)	2.9(−17)	⋯	3.5	553.6
CH^+	60.245	2.9 ± 1.5(−17)	7.1(−20)	⋯	7.9	67.6
CH^+	72.137	<1.9(−17)	4.0(−19)	⋯	8.1	72.3
CH^+	90.010	1.7 ± 0.5(−17)	5.7(−19)	⋯	8.0	78.1
CH^+	179.593	<1.8(−17)	1.8(−19)	⋯	7.5	169.8
OH	79.115	<1.7(−17)	9.6(−18)	⋯	7.9	85.0
OH	79.179	<1.9(−17)	9.8(−18)	⋯	7.9	85.6
o-H_2O	63.323	<1.6(−17)	2.2(−17)	⋯	7.9	63.0
o-H_2O	71.946	<1.7(−17)	1.8(−17)	⋯	7.8	63.2
o-H_2O	78.742	<1.8(−17)	1.2(−17)	⋯	7.8	64.0
p-H_2O	89.988	1.7 ± 0.5(−17)	4.0(−18)	⋯	7.9	63.2
o-H_2O	179.526	<1.8(−17)	1.9(−18)	⋯	5.8	310.9
o-H_2O	180.488	<1.4(−17)	5.7(−19)	⋯	7.9	114.2
CO	72.842	<2.1(−17)	8.8(−19)	⋯	7.8	66.8
CO	79.359	<1.6(−17)	2.0(−18)	⋯	7.8	68.8
CO	87.190	<4.3(−17)	4.1(−18)	⋯	7.8	90.9
CO	90.162	1.5 ± 0.6(−17)	5.1(−18)	⋯	7.7	100.4
CO	93.349	<4.3(−17)	6.5(−18)	⋯	7.7	109.5
CO	104.444	<3.7(−17)	1.4(−17)	⋯	7.1	135.5
CO	108.762	<3.0(−17)	1.9(−17)	⋯	6.8	144.1
CO	113.457	3.0 ± 0.9(−17)	2.5(−17)	⋯	6.6	152.6
CO	118.580	1.5 ± 0.7(−17)	3.2(−17)	⋯	6.4	161.1
CO	124.193	<1.5(−17)	4.1(−17)	⋯	6.3	169.9
CO	130.368	<2.2(−17)	5.1(−17)	⋯	6.1	180.4
CO	137.196	<1.9(−17)	6.0(−17)	⋯	5.9	190.8
CO	144.784	2.9 ± 0.3(−17)	6.8(−17)	⋯	5.7	203.3
CO	153.266	3.2 ± 0.5(−17)	7.3(−17)	⋯	5.5	218.1
CO	162.811	<2.5(−17)	7.6(−17)	⋯	5.3	235.6
CO	173.631	4.9 ± 1.1(−17)	7.6(−17)	⋯	5.1	255.4
CO	185.999	<2.4(−17)	7.4(−17)	⋯	4.9	276.9
CO	200.272	4.9 ± 0.9(−17)	7.0(−17)	⋯	4.7	299.2
CO	216.927	2.8 ± 0.6(−17)	6.3(−17)	⋯	4.6	321.8
CO	236.613	3.6 ± 0.7(−17)	5.6(−17)	⋯	4.5	344.8
CO	260.239	3.5 ± 0.5(−17)	4.7(−17)	⋯	4.4	368.0
CO	289.120	2.4 ± 0.5(−17)	3.8(−17)	⋯	4.3	389.1
CO	325.225	1.8 ± 0.8(−17)	2.9(−17)	⋯	4.3	407.4

Table 9
(Continued)

Species	λ (μm)	Line Flux (W m^{-2})		FWHM (km s^{-1})		Size (au)
		Observed	Model	Observed	Model	
CO	371.650	8.2 ± 3.7(−18)	2.1(−17)	···	4.2	422.9
CO	433.556	6.3 ± 3.5(−18)	1.4(−17)	···	4.2	435.9
CO	520.231	1.1 ± 0.5(−17)	8.4(−18)	···	4.1	446.1
CO	650.251	1.3 ± 0.6(−17)	4.4(−18)	···	4.1	453.0

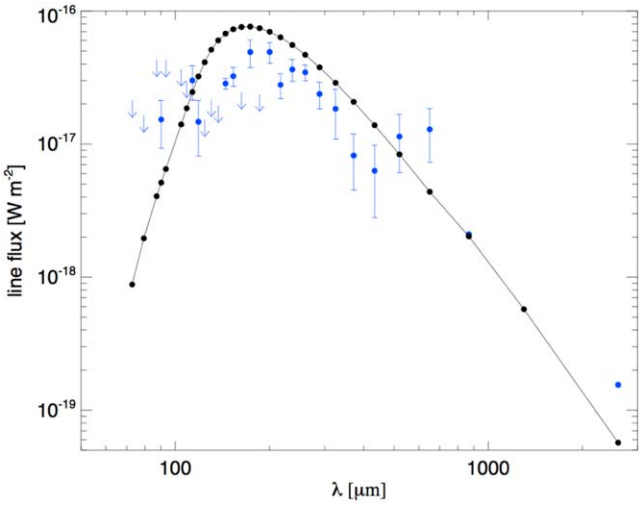

Figure 7. CO SLED in comparison to observations for HD 97048. The measurement points have 1σ errorbars attached. The blue arrows indicate upper limits, drawn from 3σ down to 1σ.
(A color version of this figure is available in the online journal.)

(Jamialahmadi et al. 2018). A more detailed study of CO rovibrational lines and possible future observation with CRIRES+ on the VLT would provide important constraints for the proposed variability scenarios. Our consistent dust and gas model is an excellent starting point for such investigations.

MWC 480 is also an excellent topic to study disk chemistry (e.g., Piétu et al. 2007; Henning et al. 2010; Chapillon et al. 2012b). For example the detection of CH_3CN and HC_3N (Chapillon et al. 2012a; Öberg et al. 2015; Huang et al. 2017; Bergner et al. 2018) together with the spatially resolved observations of CN and HCN and its isotopologues (Guzmán et al. 2015) make it a perfect target to study cyanide chemistry. Our model provides a detailed physical structure for detailed chemical studies and to test, for example, the importance of excited molecular hydrogen for CN/HCN chemistry as recently proposed by Cazzoletti et al. (2018) which might improve our fit for the CN and HCN lines.

4.5.5. HD 169142

Our HD 169142 model is a simple model on top of the SED-fit with slightly modified disk extension (Figure 13). The model has the disk dust cavity at 20 au as seen in near-IR (Quanz et al. 2013) and sub-mm continuum observations (e.g., Fedele et al. 2017), an inner disk extending from 0.1 to 5 au, thus a disk gap between 5 and 20 au. The disk masses and gas/dust ratio are not altered with respect to the SED-fitting results. The model fits the [O I] 63 μm line and CO 2–1 isotopologue lines in the (sub-)mm reasonably well (Table 12). However, the CO fundamental rovibrational lines are too strong and too narrow, leading to similar issues as for GM Aur, see page 45. In our model the ^{12}CO 4.7 μm emission is dominated by the inner wall of the outer disk. To improve the fit of these lines, one could consider a vertically extended but transparent inner disk, which would shield the inner wall of the outer disk from the stellar UV field. CRIRES observations (A. Carmona 2019, in preparation) show, however, that the ^{12}CO rovibrational emission region extends inside to at least 1 au, i.e., well through the cavity and into the inner disk. In contrast, the observations show that the narrower ^{13}CO and C^{18}O rovibrational lines (not shown in Table 12) are emitted from the outer disk >20 au. Since our model has no gas between 5 and 20 au, it fails to predict these properties of the CO isotopologue rovibrational lines.

4.5.6. HD 142666

HD 142666 was classified as a group II disk by (Meeus et al. 2001) based on its SED (Figure 1), which shows a smooth curvature, starting out with a strong near-IR excess (0.8 $L_\odot$), low-amplitude 10 and 20 μm silicate emission features and clearly detected PAH features (Figure 35), followed by a smooth and steady decline into the millimeter region. The strength of the PAH bands (Acke et al. 2010) as well as the location in the *N*-band size-color diagram (Menu et al. 2015) suggest that the geometry of HD 142666 may have some similarity with the transitional, gaped group I sources. Indeed, Rubinstein et al. (2018) find evidence from ALMA data for a large cavity of mm-side grains in the disk of

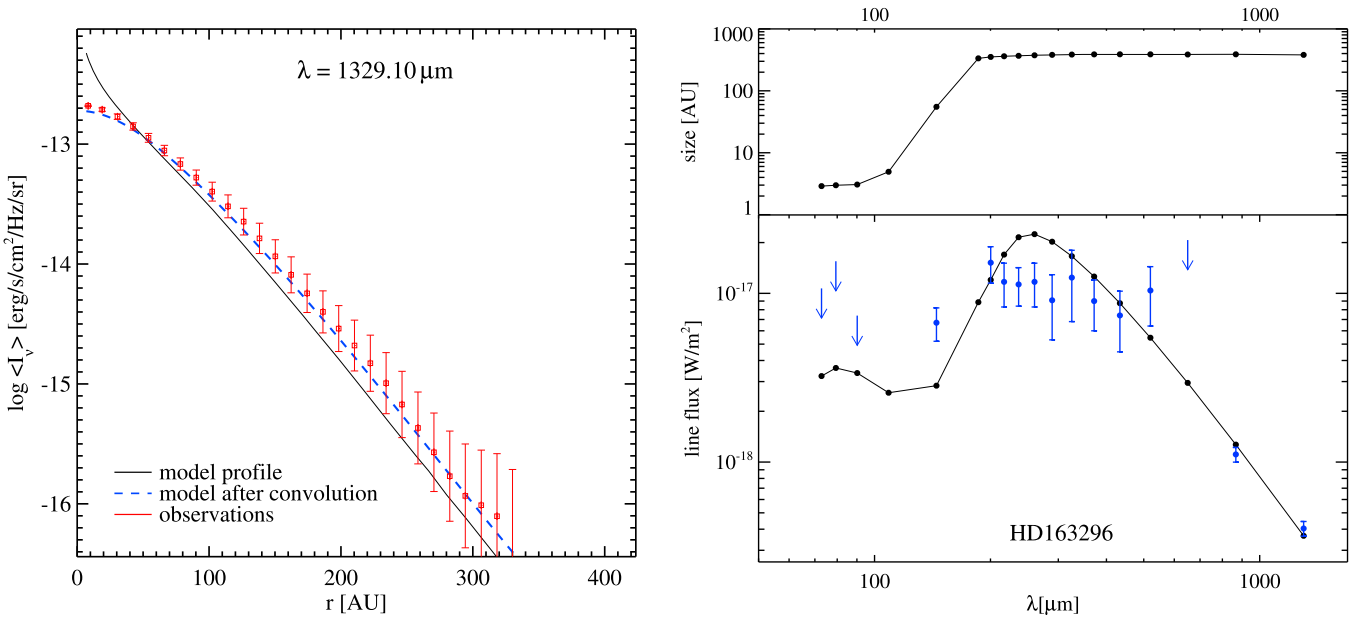

Figure 8. Left: Fit of radial intensity profile of HD 163296 at 1.3 mm (band 6 ALMA science verification data). Right: CO SLED model of HD 163296 (black lines and dots) in comparison to multi-instrument observational data (blue errorbars, arrows are 3σ non-detections).
(A color version of this figure is available in the online journal.)

HD 142666, and Garufi et al. (2017) detect the disk in scattered light. This illustrates that there is overlap in disk geometry between group I and II sources. The inner disk structure is complex as evidenced by recent near-IR interferometry (Davies et al. 2018). HD 142666 has no clear line detections other than [O I] 63 μm. The CO 3–2 and 2–1 (sub-)mm lines are detected, but the line data is noisy on a relatively bright continuum level, see Figure 15, and the two measured FWHMs contradict each other (they should be very similar if emitted from a disk).

Our DIANA standard model fits all continuum observations by a tall and marginally transparent inner disk zone casting a shadow on the main outer disk (Figure 14). The fit to the MIDI visibilities shows that the size of the 10 μm continuum emission region in the model is about correct (Figure 15). The fit to the [O I] 63 μm data is good, but the CO fundamental rovibrational lines are somewhat too strong and very broad (Table 13). The line fits worsen considerably if the stellar UV-excess is taken into account, which would lead to stronger heating and brighter emission lines. HD 142666 is known as a highly variable source (e.g., Zwintz et al. 2009).

4.5.7. Lk Ca 15

Lk Ca 15 is an important source known to have bright and rich mm-emission lines including bio-molecules. The SED requires a very flat outer disk, partly in the shadow of a high inner disk to reproduce the 10 μm silicate feature (Figure 16). The scattered light image at 1 μm (Thalmann et al. 2010) and the thermal emission image at 850 μm (Andrews et al. 2011) are consistent with a gap of ~35–50 au, very much in line with our best fit model.

Drabek-Maunder et al. (2016) show with thermo-chemical disk models that their new HCO^+ data requires the presence of gas inside 50 au and a large scale height for that inner gas disk. Based on their work, we refined the model further within the DIANA modeling framework. We still require an inner gas disk with a large scale height ($H = 0.11$ au at 1 au, Figure 16). The slightly revised DIANA disk model fits a number of (sub-)mm lines within a factor three including ^{12}CO, ^{13}CO, HCO^+, HCN, CS, and H_2CO (Table 14). Some remaining discrepancies are seen in the wings of the HCO^+ $J = 3$–2, 4–3 (Figure 17, right panel) and HCN $J = 3$–2 lines. Some profiles are slightly asymmetric like ^{13}CO $J = 2$–1 (Figure 17, left panel) and CS $J = 5$–4. This is a feature not captured in our disk model. The H_2CO lines are overall a factor three too strong in our model.

The CO $J = 6$–5 line and also the [O I] 63 μm line are a factor two and eight too strong, respectively, in our disk model, possibly suggesting that the outer disk is in fact colder than our model shows. The inner disk, though vertically extended, does neither completely shield the strong and hard X-rays from the central source, nor the strong UV excess.

4.5.8. USco J1604-2130

USco J1604-2130 is a transition disks with a large gap between 0.05 and 46 au. The H and K-band infrared excess requires dust at very small distances from the star (inner disk), while SMA imaging at 880 μm (Mathews et al. 2012) reveals

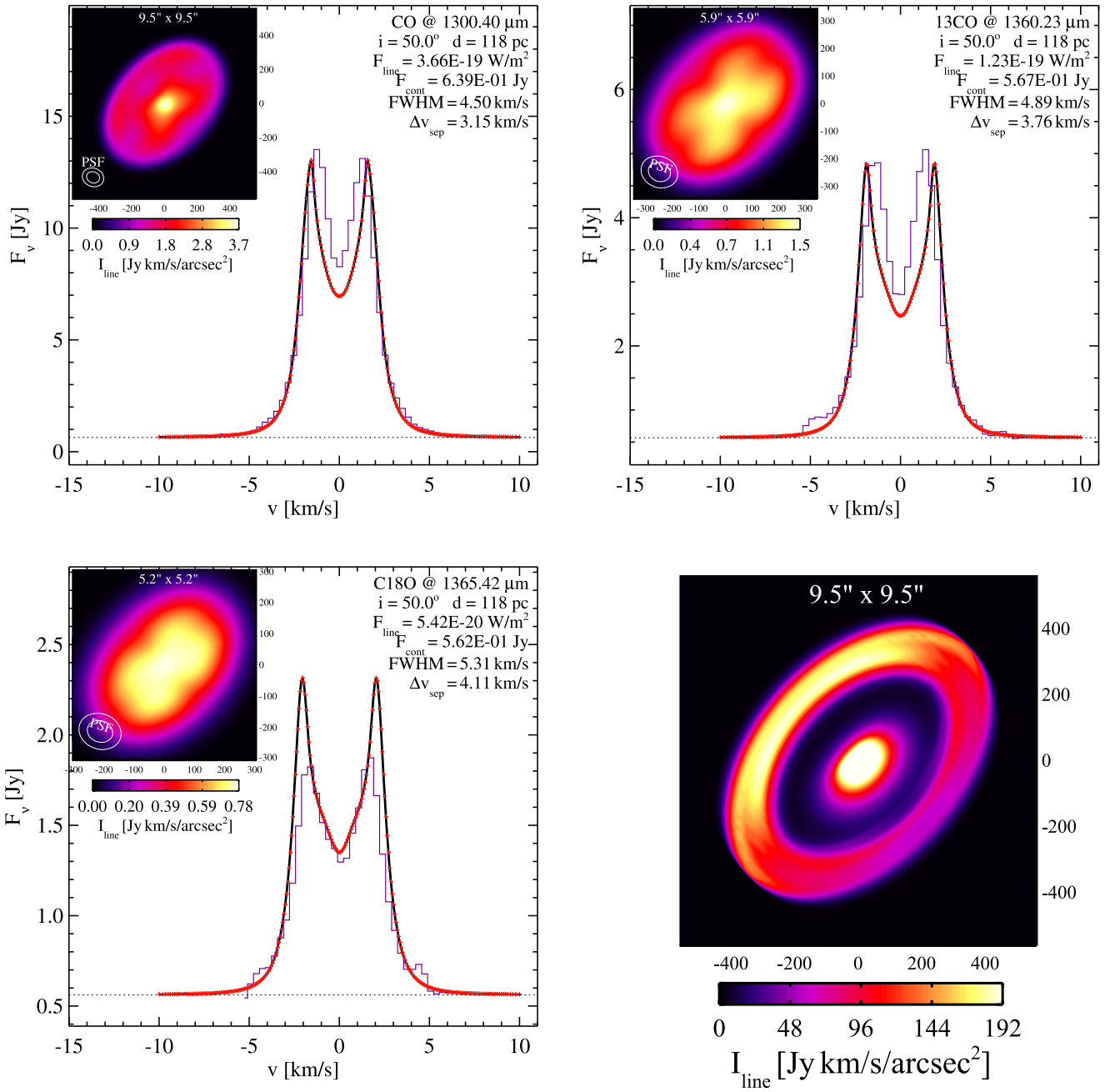

Figure 9. CO isotopologue lines around 1.3 mm for HD 163296. The lower right panel shows the [O I] 63 μm image from the disk model of HD 163296. (A color version of this figure is available in the online journal.)

the clear presence of a large gap. The small inner disk is optically thick and vertically extended (see Figure 18), thus shielding the outer disk partially from heating/dissociating UV radiation.

The far-IR and sub-mm line emission arises entirely in the outer disk and the model line fluxes match the observed ones within 30% except for the [C II] line (Table 15). The latter shows some extended emission on the *Herschel*/PACS footprint (Mathews et al. 2013). Since PACS did not resolve the disks, we cannot entirely exclude extended emission to contribute to the measured [C II] flux from the central spaxel.

Mid- and near-IR CO lines (wavelength below $\sim$100 μm) have an ever increasing contribution also from the small inner disk: $\sim$40% for the low J CO $v = 1$–0 lines increasing to 100% for $J > 20$ and $\sim$60% for the low J CO $v = 2$–1 lines increasing rapidly with J to 100%. However, line fluxes for rovibrational

Table 10
Model Properties and Comparison of Computed Spectral Line Properties with Observations from HD163296.properties

DIANA Standard Fit Model Properties	
Minimum dust temperature [K]	10
Maximum dust temperature [K]	1946
Mass-mean dust temperature [K]	27
Minimum gas temperature [K]	12
Maximum gas temperature [K]	15203
Mass-mean gas temperature [K]	29
mm-opacity-slope (0.85–1.3) mm	1.4
cm-opacity-slope (5–10) mm	1.6
mm-SED-slope (0.85–1.3) mm	2.5
cm-SED-slope (5–10) mm	3.1
10 μm silicate emission amplitude	2.0
Naked star luminosity [$L_\odot$]	34.4
Bolometric luminosity [$L_\odot$]	48.7
Near-IR excess ($\lambda = 2.05$–6.90 μm) [$L_\odot$]	4.10
Mid IR excess ($\lambda = 6.90$–29.3 μm) [$L_\odot$]	2.18
Far-IR excess ($\lambda = 29.3$–$970.$ μm) [$L_\odot$]	0.70

Species	λ (μm)	Line Flux (W m^{-2})		FWHM (km s^{-1})		Size (au)
		Observed	Model	Observed	Model	
CO	72.842	<1.1(−17)	3.2(−18)	⋯	51.9	2.9
CO	79.359	<1.6(−17)	3.6(−18)	⋯	49.2	3.0
CO	90.162	<7.4(−18)	3.4(−18)	⋯	48.1	3.1
CO	144.784	6.7 ± 1.5(−18)	2.8(−18)	⋯	20.1	55.2
CO	866.963	1.1 ± 0.0(−18)	1.3(−18)	4.5 ± 0.1	4.4	388.8
CO	1300.404	4.0 ± 0.1(−19)	3.7(−19)	4.5 ± 0.2	4.5	380.9
^{13}CO	1360.227	1.4 ± 0.2(−19)	1.2(−19)	4.9 ± 0.3	4.9	313.2
C^{18}O	1365.421	4.5 ± 0.2(−20)	5.4(−20)	5.5 ± 0.3	5.3	284.2
^{13}CO	2720.406	1.2 ± 0.7(−20)	1.1(−20)	4.5 ± 0.5	5.2	279.9
O I	63.183	1.7 ± 0.1(−16)	5.3(−16)	⋯	4.2	447.1
O I	145.525	<6.0(−18)	4.7(−17)	⋯	4.1	407.0
o-H_2O	29.836	4.3 ± 0.4(−17)	4.8(−17)	⋯	49.5	3.1
o-H_2O	63.323	1.6 ± 0.4(−17)	1.1(−17)	⋯	50.3	3.2
p-H_2O	63.458	1.1 ± 0.3(−17)	1.0(−17)	⋯	50.3	3.1
o-H_2O	71.946	1.4 ± 0.5(−17)	8.1(−18)	⋯	50.2	3.3
o-H_2O	78.742	1.1 ± 0.3(−17)	6.6(−18)	⋯	50.1	6.9
p-H_2O	78.928	<1.4(−17)	5.8(−18)	⋯	50.2	3.2
p-H_2O	89.988	<5.1(−18)	5.3(−18)	⋯	4.4	264.9
p-H_2O	144.517	<1.2(−17)	1.1(−18)	⋯	49.9	3.4
p-H_2O	158.311	<1.4(−17)	6.7(−19)	⋯	49.6	3.1
o-H_2O	179.526	<1.7(−17)	1.1(−17)	⋯	4.9	336.6
o-H_2O	180.488	<1.7(−17)	2.5(−18)	⋯	4.6	318.8
OH	79.115	1.2 ± 0.3(−17)	2.8(−18)	⋯	47.3	93.6
OH	79.179	<9.0(−18)	2.8(−18)	⋯	46.3	120.0
CO	650.251	<2.1(−17)	2.9(−18)	⋯	4.4	386.2
CO	520.231	1.0 ± 0.4(−17)	5.5(−18)	⋯	4.4	388.6
CO	433.556	7.4 ± 2.9(−18)	8.7(−18)	⋯	4.4	389.1
CO	371.650	9.0 ± 3.0(−18)	1.3(−17)	⋯	4.4	387.9
CO	325.225	1.2 ± 0.6(−17)	1.7(−17)	⋯	4.3	385.3
CO	289.120	9.1 ± 3.8(−18)	2.0(−17)	⋯	4.3	381.2
CO	260.239	1.2 ± 0.3(−17)	2.2(−17)	⋯	4.4	375.0
CO	236.613	1.1 ± 0.3(−17)	2.2(−17)	⋯	4.4	367.8
CO	216.927	1.2 ± 0.3(−17)	1.7(−17)	⋯	4.5	361.8
CO	200.272	1.5 ± 0.4(−17)	1.2(−17)	⋯	6.0	352.7
C	370.415	5.0 ± 2.0(−18)	4.9(−18)	⋯	4.2	418.4
N^+	205.240	1.7 ± 0.2(−17)	4.5(−22)	⋯	5.8	478.4

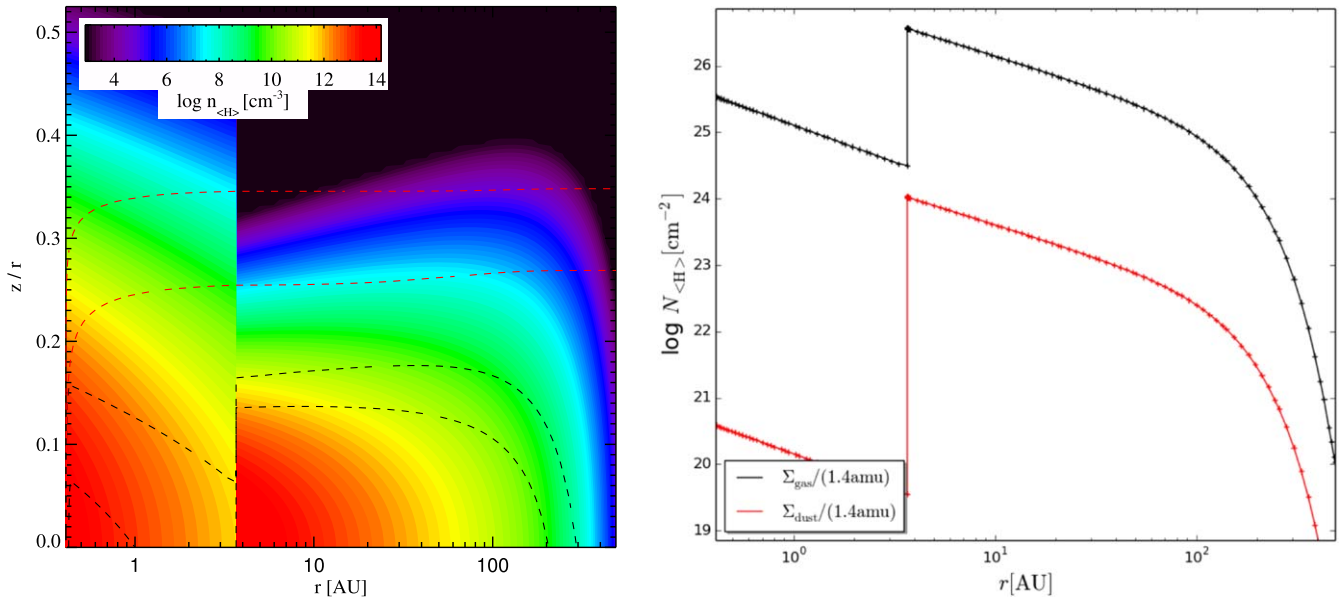

Figure 10. HD 163296 density and surface density plots. For details see Figure 4.
(A color version of this figure is available in the online journal.)

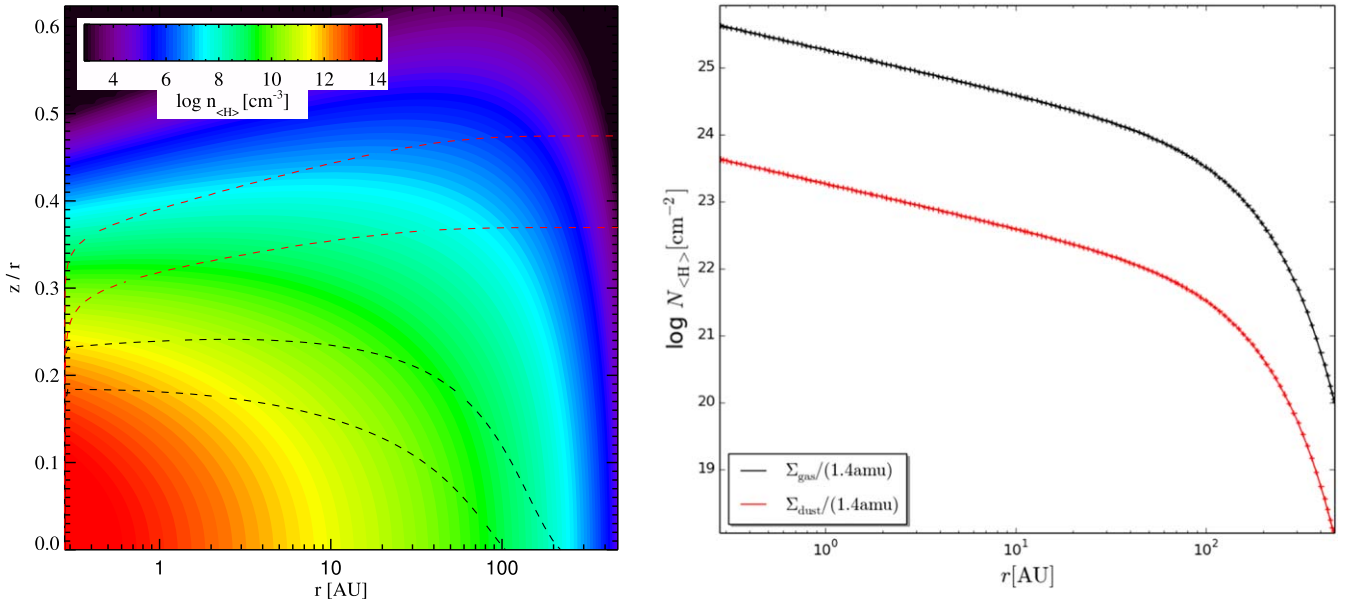

Figure 11. MWC 480 density and surface density plots. For details see Figure 4.
(A color version of this figure is available in the online journal.)

CO lines from our model are below 10^{-18} W m^{-2}. Due to the low inclination of 10°, the CO sub-mm lines are narrow with typical FWHM of 1.4 km s^{-1} (Table 15).

4.5.9. TW Hya

TW Hya probably is the best studied protoplanetary disk around a T Tauri star. Practically every suitable instrument developed in the past 30 years was pointed at this object, producing data sets of varying quality and scientific usefulness, yet the shape of the disk around TW Hya is still debated (see e.g., Menu et al. 2014; Andrews et al. 2016). Our data collection of TW Hya provides exquisite spectral (UV, X-ray, *Spitzer*/IRS, SPIRE) and photometric data (see Figure 1), one continuum image with derived intensity profile, and 57 lines, among them three with velocity and intensity profiles.

Table 11
Model Properties and Comparison of Computed Spectral Line Properties with Observations from MWC480.properties

DIANA Standard Fit Model Properties	
Minimum dust temperature [K]	11
Maximum dust temperature [K]	1599
Mass-mean dust temperature [K]	24
Minimum gas temperature [K]	11
Maximum gas temperature [K]	23865
Mass-mean gas temperature [K]	36
mm-opacity-slope (0.85–1.3) mm	1.0
cm-opacity-slope (5–10) mm	1.3
mm-SED-slope (0.85–1.3) mm	2.4
cm-SED-slope (5–10) mm	n.a.
10 μm silicate emission amplitude	1.6
Naked star luminosity [$L_\odot$]	13.3
Bolometric luminosity [$L_\odot$]	20.3
Near-IR excess (λ = 2.05–6.82 μm) [$L_\odot$]	2.88
Mid IR excess (λ = 6.82–29.1 μm) [$L_\odot$]	1.68
Far-IR excess (λ = 29.1–981. μm) [$L_\odot$]	0.58

Species	λ (μm)	Line Flux (W m^{-2})		FWHM (km s^{-1})		Size (au)
		Observed	Model	Observed	Model	
O I	63.183	9.5 ± 0.3(−17)	1.1(−16)	⋯	8.3	151.6
O I	145.525	<7.8(−18)	7.9(−18)	⋯	7.5	117.4
C II	157.740	<9.6(−18)	6.8(−18)	⋯	3.2	410.4
CO	4.633	3.1 ± 0.6(−17)	4.0(−17)	47.5 ± 10.0	94.0	6.1
CO	4.641	3.2 ± 0.6(−17)	3.6(−17)	53.7 ± 10.0	93.7	8.2
CO	4.682	3.7 ± 0.7(−17)	2.9(−17)	69.2 ± 14.0	92.9	15.3
CO	4.726	3.6 ± 0.7(−17)	4.7(−17)	48.1 ± 10.0	93.2	7.8
CO	4.735	3.6 ± 0.7(−17)	4.8(−17)	47.6 ± 10.0	93.5	6.2
CO	4.920	3.4 ± 0.7(−17)	4.3(−17)	69.9 ± 13.4	95.5	0.3
CO	4.966	2.7 ± 0.5(−17)	4.1(−17)	71.0 ± 14.2	95.5	0.3
CO	4.990	3.2 ± 0.6(−17)	4.0(−17)	80.0 ± 16.0	95.5	0.3
CO	72.842	<9.6(−18)	2.7(−20)	⋯	37.4	7.6
CO	79.359	<1.6(−17)	4.4(−20)	⋯	33.9	9.0
CO	90.162	<9.6(−18)	1.4(−19)	⋯	26.8	12.1
CO	144.784	6.9 ± 3.2(−18)	3.2(−18)	⋯	10.8	50.3
CO	866.963	6.1 ± 0.1(−19)	5.6(−19)	⋯	3.6	350.6
^{13}CO	906.846	1.1 ± 0.2(−19)	2.5(−19)	⋯	4.1	275.9
CO	1300.404	1.7 ± 0.1(−19)	1.7(−19)	⋯	3.6	346.5
o-H_2O	63.323	<6.6(−18)	9.1(−19)	⋯	34.1	7.1
o-H_2O	71.946	<1.2(−18)	9.1(−19)	⋯	30.4	9.3
o-H_2O	78.742	<1.8(−17)	1.7(−18)	⋯	17.0	35.5
OH	79.115	<9.9(−18)	2.0(−18)	⋯	8.5	106.6
OH	79.179	<1.0(−17)	2.1(−18)	⋯	8.3	110.2
CN	881.097	6.7 ± 0.7(−20)	1.6(−20)	⋯	3.1	394.9
CN	1321.390	2.5 ± 0.1(−20)	7.4(−21)	⋯	3.0	388.9
HCN	845.663	3.6 ± 0.4(−20)	9.1(−20)	⋯	4.0	294.8
HCN	1127.520	2.1 ± 0.2(−20)	4.5(−20)	⋯	3.8	325.4
HCO^+	840.380	7.5 ± 1.5(−20)	1.0(−19)	⋯	4.3	312.9
HCO^+	1120.478	4.2 ± 0.3(−20)	5.1(−20)	⋯	4.1	334.2
N_2H^+	804.439	<6.7(−21)	2.9(−21)	⋯	3.7	221.4
N_2H^+	1072.557	<6.9(−21)	1.8(−21)	⋯	3.7	221.9
CH^+	72.137	<2.2(−17)	1.1(−20)	⋯	21.0	18.5

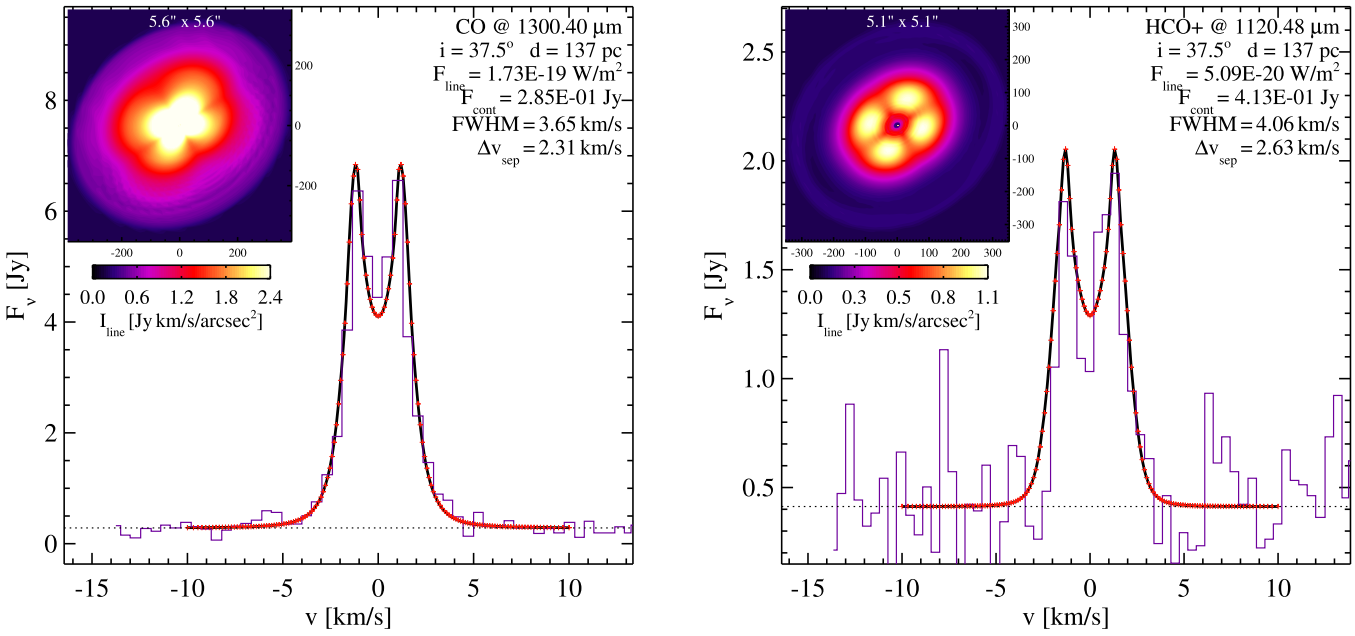

Figure 12. CO $J = 2$–1 and HCO^+ $J = 3$–2 lines in comparison to observations for MWC 480.
(A color version of this figure is available in the online journal.)

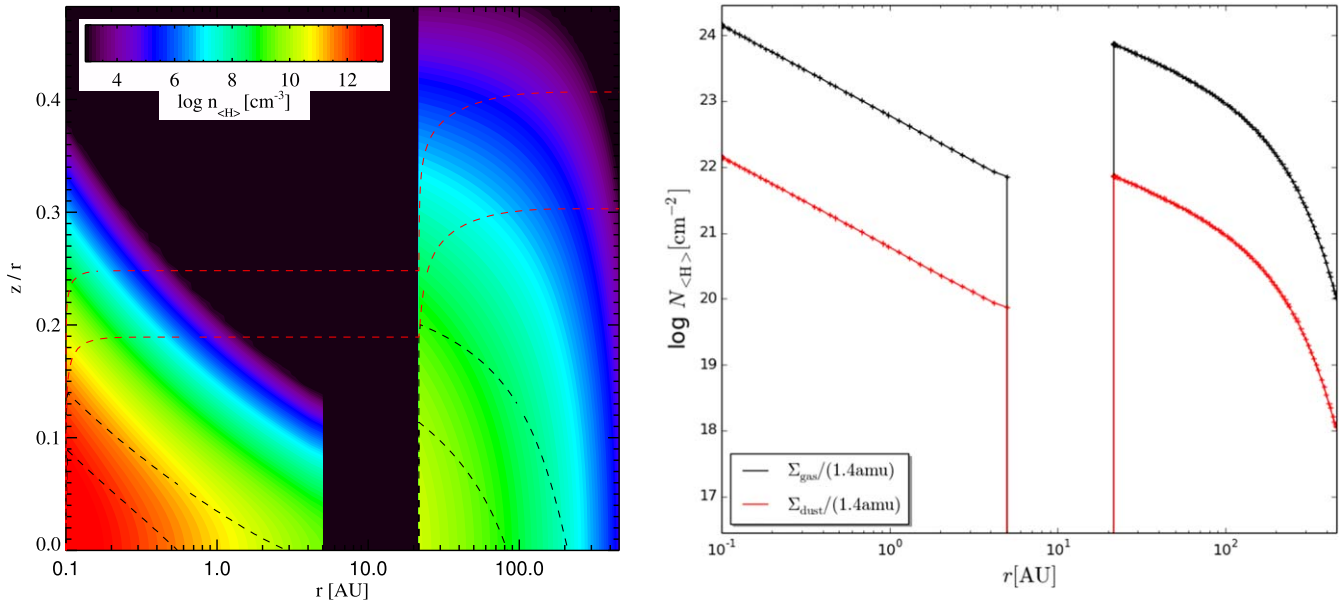

Figure 13. HD 169142 density and surface density plots. For details see Figure 4.
(A color version of this figure is available in the online journal.)

Figure 19 illustrates the geometry of the disk and the surface densities of dust and gas assumed. The model results in good fits of the SED and most line observations, from CO fundamental rovibrational lines over high-excitation water lines in the *Spitzer*-spectrum, [Ne II] 12.81 μm, far-IR high-J CO and ^{13}CO lines, to fundamental water lines (HIFI instrument) and a number of (sub-)mm lines, such as CO isotopologue lines, HCO^+, N_2H^+ and HCN (Table 16). Due to the wealth of line data, the model aims at providing appropriate line excitation conditions in very different parts of the disk, therefore it is not surprising that the fits of individually selected lines (such as CO $J = 3$–2 shown in Figure 20) are not perfect.

Table 12
Model Properties and Comparison of Computed Spectral Line Properties with Observations from HD169142.properties

DIANA Standard Fit Model Properties	
Minimum dust temperature [K]	12
Maximum dust temperature [K]	2325
Mass-mean dust temperature [K]	28
Minimum gas temperature [K]	14
Maximum gas temperature [K]	40000
Mass-mean gas temperature [K]	36
mm-opacity-slope (0.85–1.3) mm	1.0
cm-opacity-slope (5–10) mm	1.2
mm-SED-slope (0.85–1.3) mm	2.8
cm-SED-slope (5–10) mm	3.2
10 μm silicate emission amplitude	1.6
Naked star luminosity [$L_\odot$]	10.0
Bolometric luminosity [$L_\odot$]	13.7
Near-IR excess ($\lambda = 2.02$–6.72 μm) [$L_\odot$]	0.88
Mid IR excess ($\lambda = 6.72$–29.5 μm) [$L_\odot$]	0.81
Far-IR excess ($\lambda = 29.5$–$991.$ μm) [$L_\odot$]	0.99

Species	λ (μm)	Line Flux (W m^{-2})		FWHM (km s^{-1})		Size (au)
		Observed	Model	Observed	Model	
O I	63.183	7.2 ± 0.4(−17)	4.5(−17)	⋯	3.2	121.8
O I	145.525	<1.1(−17)	1.6(−18)	⋯	3.7	72.8
C II	157.740	<6.6(−18)	2.8(−18)	⋯	1.2	436.4
CO	1300.404	9.3 ± 0.4(−20)	1.7(−19)	2.1 ± 0.1	1.4	415.8
^{13}CO	1360.227	4.8 ± 0.4(−20)	4.2(−20)	2.1 ± 0.1	1.6	323.6
C^{18}O	1365.421	2.0 ± 0.4(−20)	1.0(−20)	⋯	1.7	299.1
o-H_2O	179.526	<8.7(−18)	1.5(−17)	⋯	2.3	338.7
o-H_2O	78.742	<1.1(−17)	1.9(−17)	⋯	3.2	125.1
CO	72.842	<1.6(−17)	2.6(−20)	⋯	4.1	23.6
CO	90.162	<1.1(−17)	5.4(−19)	⋯	4.1	24.0
CO	4.754	2.9 ± 0.2(−18)	2.0(−17)	7.3 ± 0.5	3.8	22.1
CO	4.773	2.6 ± 0.3(−18)	1.4(−17)	7.0 ± 0.6	3.8	22.1

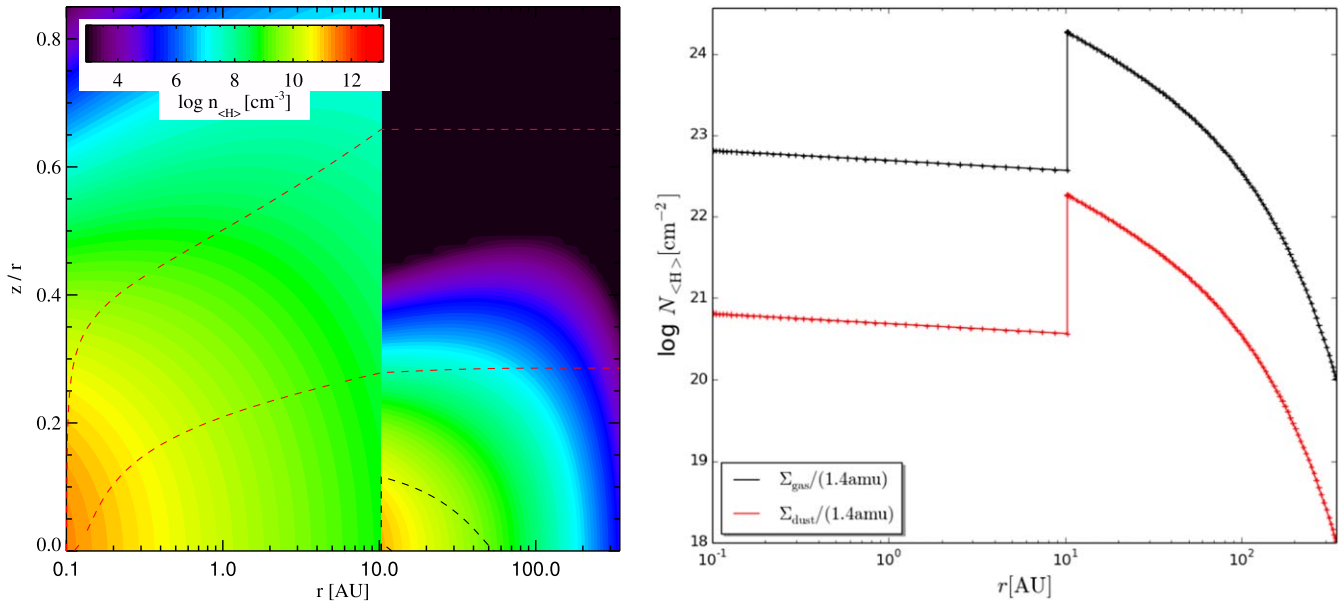

Figure 14. HD 142666 density and surface density plots. For details see Figure 4.
(A color version of this figure is available in the online journal.)

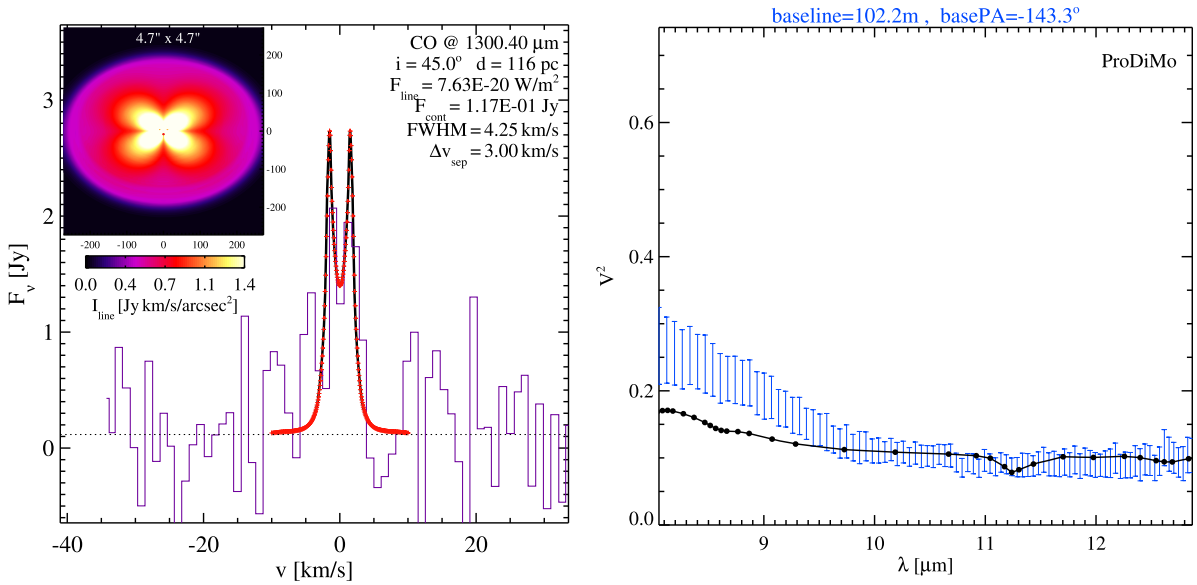

Figure 15. Left: Fit of noisy CO 2–1 archival SMA data of HD 142666. Right: Mid-IR visibilities computed by `ProDiMo` (black) in comparison to archival MIDI data (J. Menu 2018, private communication, blue) for HD 142666.
(A color version of this figure is available in the online journal.)

Unfortunately, two of the key lines observed with *Herschel* do not fit very well. The [O I] 63 μm line is too strong by a factor 4, and the HD 112 μm line is too weak by a factor of 13. Given our standard disk modeling approach, it is impossible to adjust the disk and dust opacity parameters to fit both lines. Matching the partially optically thick HD line requires a more massive disk where the gas is substantially warmer than the dust in deep layers; the [O I] 63 μm line requires just the opposite, a cooler, less massive disk.

Similar to HD 163296, we find a gas-rich disk with gas/dust $\sim$ 450, with an even more gas-enriched inner disk (gas/dust $\sim$ 800), which could be the result of radial migration

Table 13
Model Properties and Comparison of Computed Spectral Line Properties with Observations from HD142666.properties

DIANA Standard Fit Model Properties	
Minimum dust temperature [K]	7
Maximum dust temperature [K]	1890
Mass-mean dust temperature [K]	25
Minimum gas temperature [K]	10
Maximum gas temperature [K]	24910
Mass-mean gas temperature [K]	34
mm-opacity-slope (0.85–1.3) mm	0.6
cm-opacity-slope (5–10) mm	0.9
mm-SED-slope (0.85–1.3) mm	2.2
cm-SED-slope (5–10) mm	2.8
10 μm silicate emission amplitude	1.8
Naked star luminosity [$L_\odot$]	6.3
Bolometric luminosity [$L_\odot$]	9.1
Near-IR excess ($\lambda = 2.02$–6.72 μm) [$L_\odot$]	0.81
Mid IR excess ($\lambda = 6.72$–29.5 μm) [$L_\odot$]	0.60
Far-IR excess ($\lambda = 29.5$–$991.$ μm) [$L_\odot$]	0.22

Species	λ (μm)	Line Flux (W m^{-2})		FWHM (km s^{-1})		Size (au)
		Observed	Model	Observed	Model	
CO	1300.404	1.1 ± 0.1(−19)	7.6(−20)	6.4 ± 1.3	4.2	245.2
CO	2600.758	4.4 ± 0.4(−20)	8.9(−21)	10.6 ± 1.3	4.4	231.6
CO	72.842	<3.0(−17)	5.0(−20)	⋯	122.4	0.6
CO	130.368	<1.2(−17)	1.0(−18)	⋯	27.7	9.3
O I	63.183	1.9 ± 0.3(−17)	1.7(−17)	⋯	21.2	46.7
O I	145.525	<4.7(−18)	1.9(−18)	⋯	15.4	39.9
C II	157.740	<9.0(−18)	1.2(−18)	⋯	3.6	304.8
CO	72.842	<1.6(−17)	5.0(−20)	⋯	122.4	0.6
CO	79.359	<1.9(−17)	8.5(−20)	⋯	104.1	0.8
CO	90.162	<1.3(−17)	1.8(−19)	⋯	79.5	1.8
CO	144.784	<6.2(−18)	1.2(−18)	⋯	23.0	11.5
CO	4.652	<5.6(−18)	9.3(−18)	⋯	146.1	1.8
CO	4.990	<3.1(−18)	4.4(−18)	⋯	146.2	0.2

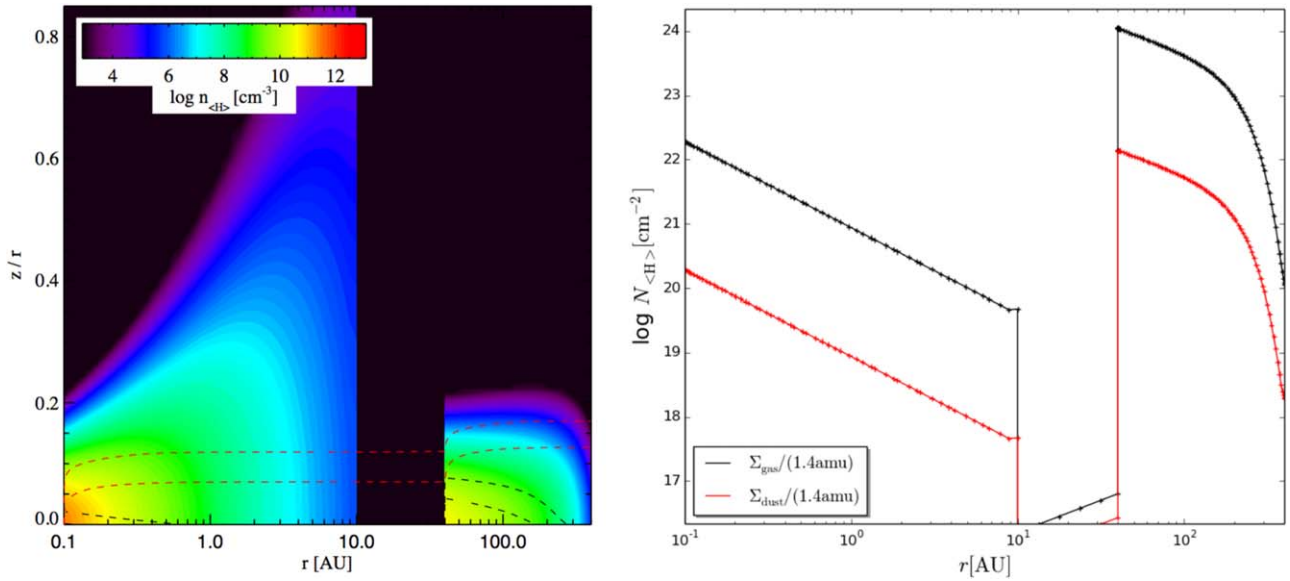

Figure 16. Lk Ca 15 density and surface density plots. For details see Figure 4. (A color version of this figure is available in the online journal.)

during disk evolution (in the outer disk) and a planet located at the transition between inner and outer disk which traps the dust, keeping the larger grains in the outer disk. Similar to HD 163296, it seems essential for TW Hya to assume a gas-rich inner disk with little dust, to boost all gas lines at shorter wavelengths, see also Thi et al. (2010) and Kamp et al. (2013).

Despite some remaining deviations between model and observations, we consider this TW Hya disk model as our "flagship," because of the unprecedented degree of physical and chemical consistency in the model, its simplicity, and the agreement of the results with a large suite of multi-wavelength line and continuum data. Recently, Du et al. (2015) and Kama et al. (2016b) published TW Hya models aiming at a consistent fitting of the HD and CO lines and the CO and [C I] lines respectively. Both models require a strong depletion of the elements oxygen and carbon in the surface layers of the disk around TW Hya. While the element depletion remains an issue of debate we raise here some points that might explain the differences. Du et al. (2015) use a three component model where one of the components has a tapered outer edge at 50 au; the detailed structure and tapering of the outer edge of the disk has been shown to have a profound effect on the CO line fluxes, especially also the line ratios of the isotopologues (Woitke et al. 2016). Also, dust settling is shown to affect the rarer isotopologues; the settling parameters in our model $\alpha_{\rm set} = 5 \times 10^{-3}$ indicates only moderate turbulence, which profoundly changes the gas-to-dust mass ratio in the line forming regions of the far-IR lines, especially in the outer disk where gas densities are low. The model presented here fits the CO isotopologue lines in the sub-mm and the water lines within a factor two, without any additional assumptions about peculiar element abundances. So, while enlarging the disk mass and simultaneously decreasing the carbon or oxygen abundances may be a tempting option to improve some line fits, it might worsen the fits in other spectral regions, for example the mid-IR and sub-mm and water lines (Kamp et al. 2013). Kama et al. (2016a) showed in a more detailed parameter study using the DALI code (Bruderer et al. 2009) that the flaring angle and tapering radius both affect the carbon fine structure and CO sub-mm lines in the same way as the carbon elemental abundance. In addition, the differences in quoted observed line fluxes from various papers amount to a factor 2–3 as well. Clearly more work is needed to reconcile the remaining model discrepancies.

4.5.10. GM Aur

GM Aur has been fitted by hand, independent of the SED-fit shown in Figure 1. We therefore show the obtained SED-fit by this model in Figure 21 as well. The density and column density structure are shown in Figure 22. Not all model parameters have been varied, so some of the dust size and material parameters, and the gas/dust ratio, still have their default values for T Tauri stars as recommended in (Woitke et al. 2016). These circumstances allow us to assess the uncertainties in mass determination. The DIANA-standard model shown here is about a factor of 3 less massive as the SED-fit model which resulted in a total disk mass of 0.11 $M_\odot$.

A good fit of the SED, [O I] 63 μm and CO 2–1 and HCO^+ 3–2 lines has been obtained. However, the CO fundamental rovibrational lines are too strong in the model, and too narrow (Table 17). In the model, these lines originate from the inner

Table 14
Model Properties and Comparison of Computed Spectral Line Properties with Observations from LkCa15.properties

DIANA Standard Fit Model Properties	
Minimum dust temperature [K]	6
Maximum dust temperature [K]	1538
Mass-mean dust temperature [K]	12
Minimum gas temperature [K]	6
Maximum gas temperature [K]	27008
Mass-mean gas temperature [K]	18
mm-opacity-slope (0.85–1.3) mm	1.2
cm-opacity-slope (5–10) mm	1.8
mm-SED-slope (0.85–1.3) mm	2.4
cm-SED-slope (5–10) mm	3.5
10 μm silicate emission amplitude	2.2
Naked star luminosity [$L_\odot$]	1.4
Bolometric luminosity [$L_\odot$]	1.6
Near-IR excess ($\lambda = 2.02$–6.72 μm) [$L_\odot$]	0.06
Mid IR excess ($\lambda = 6.72$–29.5 μm) [$L_\odot$]	0.05
Far-IR excess ($\lambda = 29.5$–$991.$ μm) [$L_\odot$]	0.07

Species	λ (μm)	Line Flux (W m^{-2})		FWHM (km s^{-1})		Size (au)
		Observed	Model	Observed	Model	
O I	63.183	1.0 ± 0.2(−17)	8.4(−17)	⋯	6.7	161.2
O I	145.525	<9.0(−18)	2.6(−18)	⋯	7.0	102.7
C II	157.740	<1.1(−17)	3.8(−18)	⋯	3.5	312.5
CO	1300.404	8.7 ± 0.2(−20)	7.6(−20)	2.8 ± 0.1	3.6	269.5
^{13}CO	1360.227	3.2 ± 0.2(−20)	2.6(−20)	2.9 ± 0.3	3.9	220.2
C^{18}O	1365.421	5.3 ± 0.4(−21)	9.3(−21)	⋯	4.3	201.2
HCO$^+$	1120.478	4.7 ± 0.2(−20)	2.9(−20)	3.3 ± 0.2	3.2	289.4
HCN	1127.520	5.1 ± 0.3(−20)	4.1(−20)	4.0 ± 0.3	3.2	300.4
CS	1223.964	1.2 ± 0.2(−20)	6.1(−21)	3.4 ± 0.6	3.2	265.6
o-H$_2$CO	1419.394	9.4 ± 0.5(−21)	1.2(−20)	⋯	2.9	337.3
p-H$_2$CO	1373.794	5.4 ± 0.5(−21)	1.4(−20)	⋯	2.9	339.0
o-H$_2$CO	1328.291	8.0 ± 0.4(−21)	1.4(−20)	2.7 ± 0.4	2.9	335.1
CO	433.556	6.2 ± 0.3(−19)	1.3(−18)	5.4 ± 0.5	3.8	243.2
HCO$^+$	840.380	1.4 ± 0.1(−19)	5.8(−20)	3.4 ± 0.2	3.3	273.9

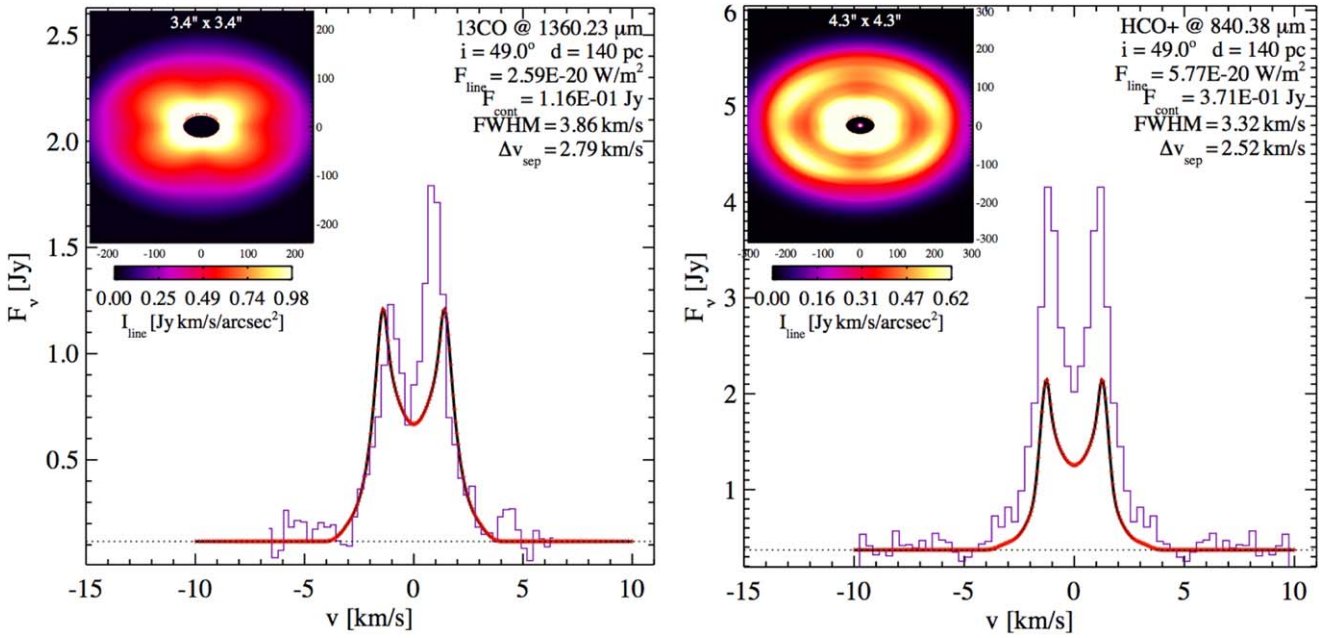

Figure 17. ^{13}CO $J = 2$–1 and HCO$^+$ $J = 3$–2 lines in comparison to observations for Lk Ca 15.
(A color version of this figure is available in the online journal.)

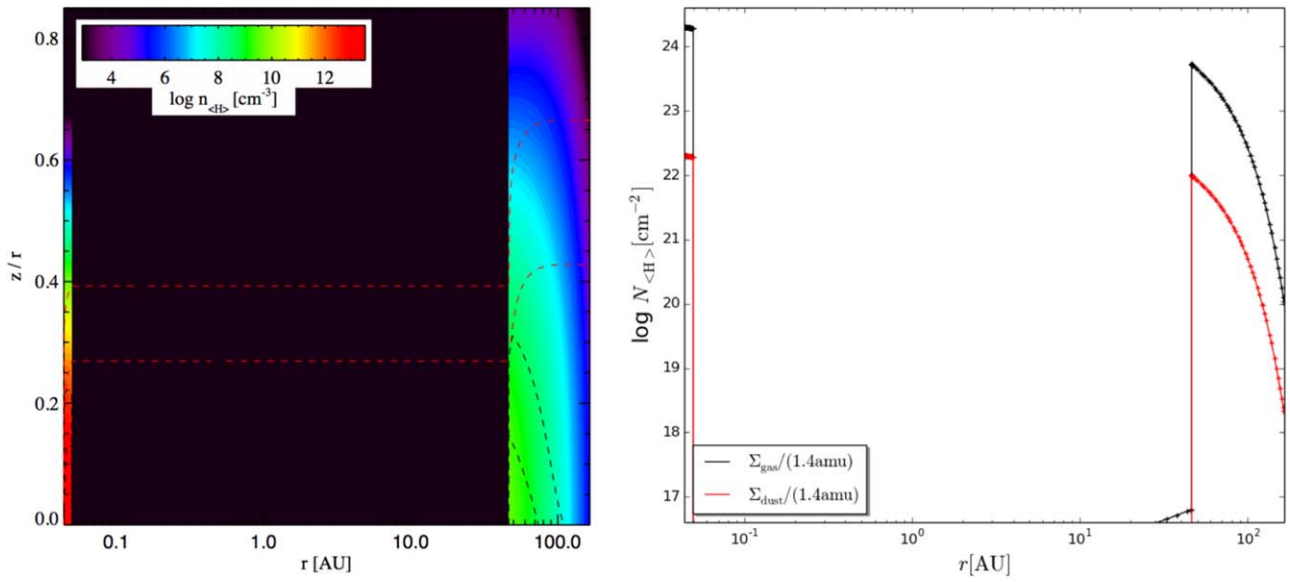

Figure 18. USco J1604-2130 density and surface density plots. For details see Figure 4.
(A color version of this figure is available in the online journal.)

wall of the outer disk at 20 au, and this wall emission is about a factor of 100 too bright, and also too narrow by a factor 2–3. A tall but tenuous inner disk might improve the fit of the CO fundamental lines, to shield the stellar UV field, similar to CY Tau and BP Tau.

McClure et al. (2016) derives a total disk mass of $M_{\rm disk} = 0.18\,M_\odot$ from SED modeling (gas to dust ratio of 100) and from HD $J = 1$–0 line observations they estimated $(2.5\text{–}20.4) \times 10^{-2}\,M_\odot$. They claim a CO gas phase depletion of up to two orders of magnitude using a rough estimate for the

Table 15
Model Properties and Comparison of Computed Spectral Line Properties with Observations from UScoJ1604-2130.properties

DIANA Standard Fit Model Properties	
Minimum dust temperature [K]	13
Maximum dust temperature [K]	1869
Mass-mean dust temperature [K]	24
Minimum gas temperature [K]	14
Maximum gas temperature [K]	27686
Mass-mean gas temperature [K]	31
mm-opacity-slope (0.85–1.3) mm	1.6
cm-opacity-slope (5–10) mm	1.5
mm-SED-slope (0.85–1.3) mm	3.2
cm-SED-slope (5–10) mm	3.5
10 μm silicate emission amplitude	1.1
Naked star luminosity [$L_\odot$]	0.8
Bolometric luminosity [$L_\odot$]	1.1
Near-IR excess ($\lambda = 2.02$–6.72 μm) [$L_\odot$]	0.07
Mid IR excess ($\lambda = 6.72$–29.5 μm) [$L_\odot$]	0.02
Far-IR excess ($\lambda = 29.5$–$991.$ μm) [$L_\odot$]	0.16

Species	λ (μm)	Line Flux (W m^{-2})		FWHM (km s^{-1})		Size (au)
		Observed	Model	Observed	Model	
O I	63.183	2.9 ± 0.2(−17)	3.1(−17)	⋯	1.6	85.8
C II	157.740	5.9 ± 1.7(−18)	1.6(−18)	⋯	1.3	146.3
CO	866.963	6.5 ± 0.1(−20)	8.8(−20)	⋯	1.4	139.5
CO	2600.758	2.5 ± 0.9(−21)	3.0(−21)	⋯	1.4	135.5

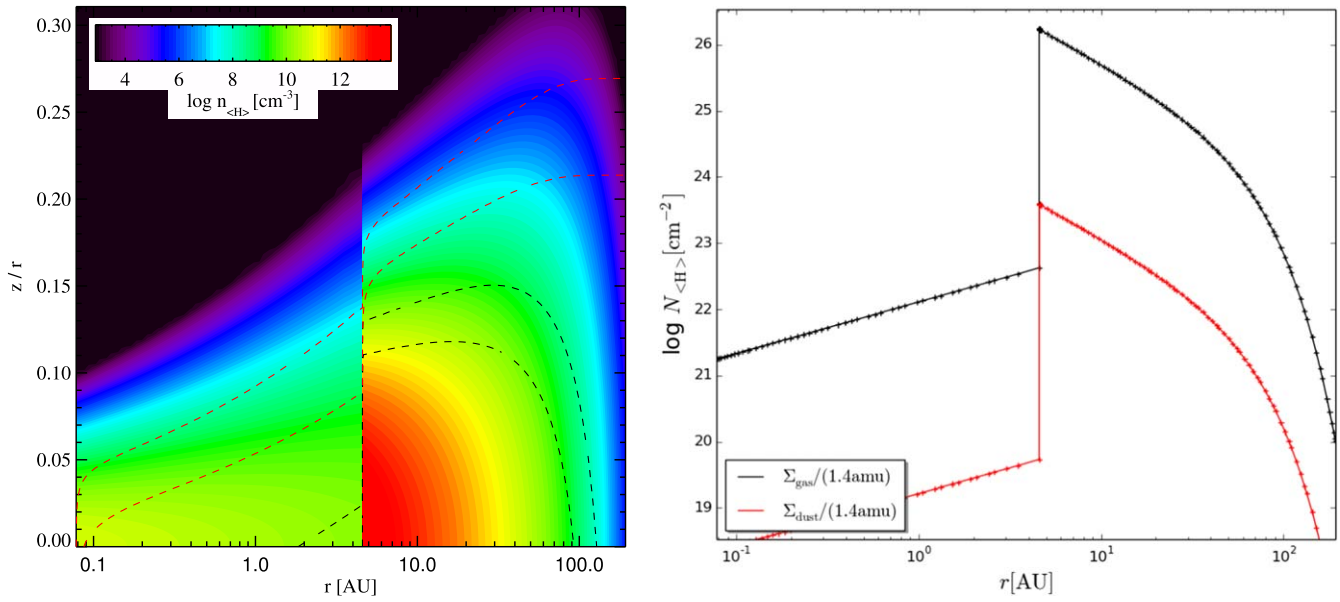

Figure 19. TW Hya density and surface density plots. For details see Figure 4. (A color version of this figure is available in the online journal.)

CO disk mass. However, due to the large uncertainties in disk masses derived via CO and HD also much lower depletion factors are possible. In the DIANA standard model we get a disk gas mass of $M_{\rm disk} = 3.3 \times 10^{-2}\,M_{\rm Sun}$ which is consistent with the HD derived disk mass but about an order of magnitude higher than the CO disk mass estimate of McClure et al. (2016). This implies that for our model no additional CO gas depletion is necessary. However, only the ^{12}CO $J = 2$–1 is included for the modeling. Further observations of CO isotopologues (e.g., with ALMA) and higher quality HD observations (e.g., possibly with SOFIA) are required to better constrain the disk masses and possibly the depletion of CO in GM Aur.

4.5.11. BP Tau

For BP Tau, the SED (Figure 1) is characterized by a strong near-IR excess and a large amplitude 10 μm silicate emission feature, followed by a steep and steady decline of the flux toward about 300 μm, where the SED eventually kinks downward with a modest millimeter-slope of about 2.1.

The model fits these properties, and a number of gas line observations in the millimeter, far-IR and near-IR regions, by assuming a tenuous but vertically highly extended inner disk (extending radially to 1.3 au) that casts a shadow onto the outer massive disk which is flat and strongly settled (Figure 23). The fit includes high-resolution Keck/NIRSPEC observations of fundamental rovibrational CO emission around 4.6 μm (Najita et al. 2003) as shown in Figure 24. We used the new Fast Line Tracer (FLiTs, Woitke et al. 2018) to calculate the CO spectrum from this disk. A good fit with the `ProDiMo` → FLiTs model was found *only after* viscous heating was taken into account, and the inner disk zone was assumed to to be tenuous and vertically highly extended, which creates sufficient hot gas (Table 18). The fit of the [O I] 63 μm line is not quite satisfactory, a factor of about 3 too bright, but that factor would be even larger if there was no tall inner disk assumed, which provides some shielding from the stellar UV (BP Tau is a strong UV and X-ray source).

4.5.12. DM Tau

Our DM Tau model is a simple model on top of the SED-fit, so it does not necessarily provide any further insight about the disk mass and gas/dust ratio. DM Tau is one of the largest, brightest, and best-studied T Tauri disks. Its SED (see Figure 1) is similar to TW Hya and GM Aur, showing the typical features of transitional disks, where the near-IR excess is mostly lacking. For the inner disk we find an increasing surface density profile. The massive outer disk starts at 13.5 au in the model (Figure 25). Most (sub-) mm lines fit well, including HCO^+ (Figure 26) and N_2H^+ lines. The fit of the HCN and CN lines is less convincing. The CO 2–1 isotopologue line show that the model may be a bit too extended. The [O I] 63 μm line is too strong by a factor of seven, although the outer disk is quite flat and already partly shielded by a tall inner disk. Table 19 provides an overview of all line results. The very faint near-IR excess does not allow to have much more shielding by the inner disk (as in the case of CY Tau or GM Aur)

Table 16
Model Properties and Comparison of Computed Spectral Line Properties with Observations from TWHya.properties

DIANA Standard Fit Model Properties	
Minimum dust temperature [K]	7
Maximum dust temperature [K]	1112
Mass-mean dust temperature [K]	21
Minimum gas temperature [K]	7
Maximum gas temperature [K]	40000
Mass-mean gas temperature [K]	21
mm-opacity-slope (0.85–1.3) mm	1.2
cm-opacity-slope (5–10) mm	1.4
mm-SED-slope (0.85–1.3) mm	2.2
cm-SED-slope (5–10) mm	3.0
10 μm silicate emission amplitude	2.2
Naked star luminosity [$L_\odot$]	0.3
Bolometric luminosity [$L_\odot$]	0.3
Near-IR excess ($\lambda = 2.02$–6.99 μm) [$L_\odot$]	0.01
Mid IR excess ($\lambda = 6.99$–29.4 μm) [$L_\odot$]	0.03
Far-IR excess ($\lambda = 29.4$–$972.$ μm) [$L_\odot$]	0.04

Species	λ (μm)	Line Flux (W m^{-2})		FWHM (km s^{-1})		Size (au)
		Observed	Model	Observed	Model	
O I	63.183	3.7 ± 0.1(−17)	1.4(−16)	⋯	1.3	97.6
O I	145.525	<3.6(−18)	2.9(−18)	⋯	1.5	99.5
C II	157.740	<3.6(−18)	2.4(−18)	⋯	1.0	159.8
o-H_2O	20.341	5.2 ± 2.0(−18)	1.8(−17)	⋯	11.3	0.8
o-H_2O	23.859	1.1 ± 0.2(−17)	2.6(−17)	⋯	10.2	2.1
o-H_2O	25.365	6.6 ± 2.0(−18)	2.7(−17)	⋯	9.8	3.5
o-H_2O	30.525	2.4 ± 0.2(−17)	2.5(−17)	⋯	9.0	4.7
o-H_2O	30.870	1.6 ± 0.2(−17)	2.1(−17)	⋯	9.2	4.6
OH_H	27.393	1.5 ± 0.2(−17)	2.6(−18)	⋯	12.3	0.8
OH_H	30.277	1.6 ± 0.2(−17)	2.4(−18)	⋯	12.0	0.8
OH_H	33.875	2.9 ± 0.2(−17)	2.0(−18)	⋯	11.8	0.9
o-H_2O	63.323	<7.2(−18)	5.3(−18)	⋯	6.7	15.3
o-H_2O	71.946	<6.3(−18)	4.6(−18)	⋯	3.4	26.7
o-H_2O	78.742	<6.0(−18)	5.4(−18)	⋯	2.1	43.3
p-H_2O	89.988	3.1 ± 0.9(−18)	3.4(−18)	⋯	2.1	46.7
o-H_2O	179.526	<7.8(−18)	3.0(−18)	⋯	1.5	65.3
o-H_2O	180.488	<8.4(−18)	6.1(−19)	⋯	2.0	44.1
p-H_2O	269.272	6.1 ± 0.4(−19)	1.2(−18)	⋯	1.3	95.3
o-H_2O	538.288	1.7 ± 0.4(−19)	2.5(−19)	⋯	1.1	105.1
CO	1300.403	1.1 ± 0.1(−19)	1.7(−19)	⋯	0.8	162.4
CO	866.963	3.9 ± 0.2(−19)	5.7(−19)	0.7 ± 0.1	0.8	173.1
CO	650.251	5.9 ± 0.6(−19)	1.3(−18)	⋯	0.8	164.2
CO	433.556	6.1 ± 0.6(−19)	3.0(−18)	⋯	0.9	150.2
CO	260.239	2.1 ± 0.2(−18)	3.7(−18)	⋯	1.2	80.4
CO	200.272	1.1 ± 0.2(−17)	1.6(−18)	⋯	1.8	51.0
CO	144.784	3.5 ± 1.2(−18)	8.7(−19)	⋯	4.4	7.6
CO	113.457	4.4 ± 1.2(−18)	6.0(−19)	⋯	6.6	4.5
^{13}CO	1360.227	2.0 ± 0.1(−20)	2.5(−20)	⋯	1.0	123.8

Table 16
(Continued)

Species	λ (μm)	Line Flux (W m^{-2})		FWHM (km s^{-1})		Size (au)
		Observed	Model	Observed	Model	
^{13}CO	906.846	4.4 ± 2.7(−20)	9.5(−20)	⋯	1.0	119.7
^{13}CO	453.497	1.8 ± 0.3(−19)	4.0(−19)	1.4 ± 0.1	1.1	98.2
^{13}CO	272.204	3.6 ± 0.4(−19)	1.9(−19)	⋯	1.5	66.1
C^{18}O	1365.430	5.0 ± 1.4(−21)	6.0(−21)	⋯	1.1	109.7
HCO^+	3361.334	2.5 ± 0.4(−21)	1.2(−21)	⋯	0.7	175.9
HCO^+	1120.478	1.1 ± 0.2(−19)	6.6(−20)	⋯	0.8	177.5
HCO^+	840.380	2.7 ± 0.1(−19)	1.2(−19)	0.7 ± 0.1	0.8	177.8
HCN	1127.520	7.5 ± 1.5(−20)	8.4(−20)	⋯	0.8	170.5
HCN	845.663	1.1 ± 0.3(−19)	1.5(−19)	⋯	0.8	161.7
N_2H^+	1072.557	2.0 ± 0.4(−20)	6.6(−21)	⋯	0.8	125.0
N_2H^+	804.439	5.7 ± 0.9(−20)	1.1(−20)	⋯	0.8	119.2
HD	112.053	6.3 ± 0.7(−18)	4.8(−19)	⋯	1.9	63.9
HD	56.223	<8.1(−18)	8.2(−20)	⋯	3.3	75.8
OH	55.890	2.2 ± 0.1(−17)	5.0(−18)	⋯	8.2	4.5
OH	55.950	2.7 ± 0.1(−17)	5.8(−18)	⋯	7.8	4.6
CO	4.609	6.4 ± 0.2(−18)	5.6(−18)	7.2 ± 0.2	12.3	4.6
CO	4.657	3.7 ± 0.2(−18)	2.8(−18)	7.2 ± 0.3	4.9	4.8
CO	4.682	4.1 ± 0.2(−18)	3.4(−18)	7.7 ± 0.3	4.9	5.0
CO	4.754	6.2 ± 0.1(−18)	6.5(−18)	7.1 ± 0.2	11.7	4.6
CO	4.793	7.2 ± 0.3(−18)	6.7(−18)	7.7 ± 0.3	12.6	4.6
CO	4.966	3.9 ± 1.0(−18)	3.2(−18)	18.5 ± 1.0	16.4	0.5
CO	4.990	2.3 ± 0.7(−18)	2.8(−18)	11.8 ± 1.0	16.5	0.5
O I	0.630	1.2 ± 0.1(−16)	2.2(−16)	10.0 ± 1.0	12.2	6.2
O I	0.557	1.7 ± 0.5(−17)	4.3(−17)	10.0 ± 1.0	19.2	0.8
S^+	0.406	4.4 ± 0.5(−17)	1.7(−19)	⋯	8.7	9.3
Ne^+	12.814	7.0 ± 0.2(−17)	3.4(−17)	⋯	4.5	45.8
Ne^{++}	15.554	5.0 ± 2.0(−18)	1.2(−17)	⋯	4.3	88.5
o-H_2	17.033	1.2 ± 0.2(−17)	5.9(−19)	⋯	4.7	24.9
p-H_2	12.277	7.0 ± 2.0(−18)	2.4(−19)	⋯	5.6	40.9

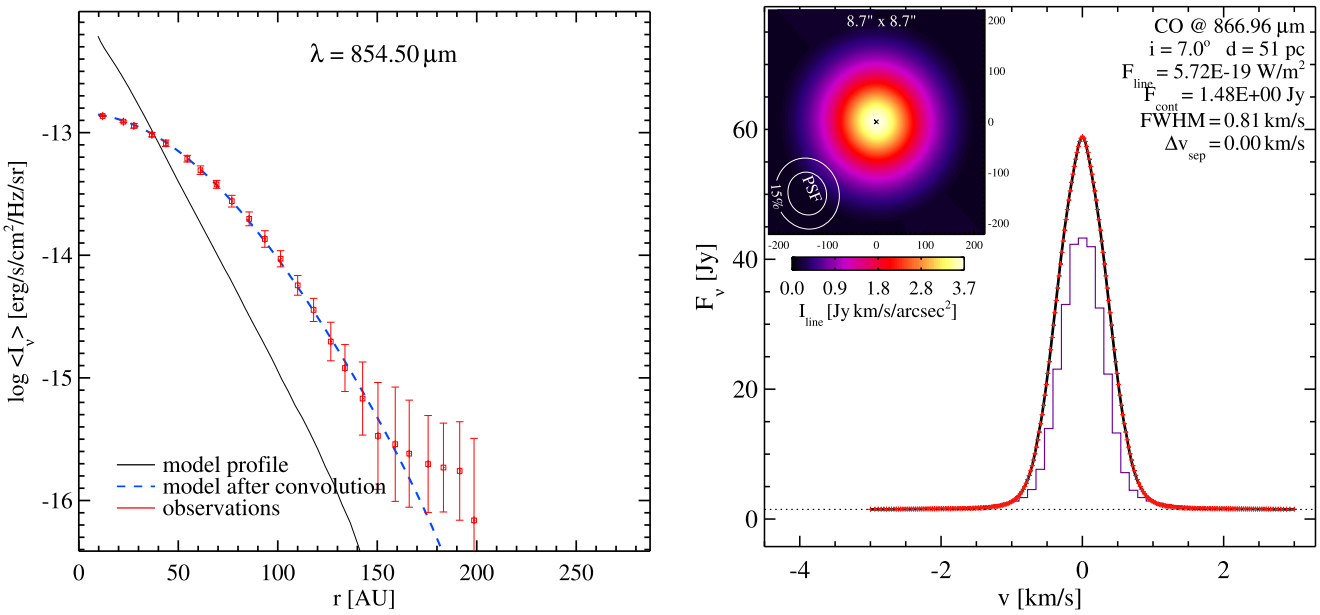

Figure 20. Left: Fit of radial intensity profile to archival ALMA 850 μm continuum data. Right: CO $J = 3$–2 line from TW Hya disk model in comparison to ALMA data.

(A color version of this figure is available in the online journal.)

to further reduce the UV and X-ray irradiation of the outer disk, which would weaken the [O I] 63 μm line. This issue might be related with the different X-ray luminosities reported in the literature (factor of ten, see Section 4.1 for details). But we have not tested the older lower X-ray luminosity with our model, furthermore a strong variability in X-rays is also a possible scenario.

McClure et al. (2016) derived a disk gas mass in the range of (1.0–4.7) $\times$ $10^{-2}\,M_\odot$ based on measurements of the HD $J =$ 1–0 spectral line and suggests a lower CO gas phase abundance of up to a factor of 5 compared to the canonical abundance of $\approx 10^{-4}$ (relative to molecular hydrogen), but the case of no CO depletion is also possible. This is consistent with our model with a disk gas mass of $1.6 \times 10^{-2}\,M_\odot$ and no CO depletion additionally to freeze-out. We note that the HD line was not included in our modeling.

As the disk of DM Tau is large and bright it is a popular target for molecular line observations and disk chemistry studies (e.g., Dutrey et al. 1997; Öberg et al. 2010; Loomis et al. 2015; Teague et al. 2015; Semenov et al. 2018). One interesting example is the detection of C_2H (Henning et al. 2010; Bergin et al. 2016) in DM Tau. The authors suggest that the X-ray/UV radiation and dust evolution play a crucial role for the C_2H abundance. Our model and the collected data provides additional constraints on the disk physical structure (e.g., radiation fields) and is therefore a ideal test-bed for further chemical studies although a more elaborate chemical network is likely required.

4.5.13. CY Tau

CY Tau has an SED (see Figure 1) with almost no 10 and 20 μm silicate emission features, that is steeply declining in the mid-IR, and has only a modest far-IR excess. At longer wavelengths this excess drops steadily all the way up to about 850 μm. The mm-fluxes are strong. The model explains this particular SED-shape by a very cold yet massive and strongly settled outer disk which is located in the shadow of a tenuous, tall inner disk (Figure 27).

The gas/dust ratio was fixed at 100 during the model fitting. The total disk mass of $0.12\,M_\odot$ is exceptionally large for this $M_\star = 0.43\,M_\odot$ T Tauri star, even larger than the value $0.10\,M_\odot$ obtained from the pure SED-fit, see Table 4. All observed emission lines are predicted well (Table 20). The CO $J = 2$–1 to ^{13}CO $J = 2$–1 line ratio is observed to be quite small, only $\sim$2. The model manages to explain this peculiar line ratio by an almost sharp outer edge with $\epsilon = 0.11$ and $\gamma = -0.34$.

Figure 28 shows a FLiTs spectrum for the R-branch of fundamental CO $v = 1$–0, with a very good fit of a number of individual lines including some CO $v = 2$–1 and o-H_2O lines, which was only obtained after lowering the column densities in the inner disk zone while simultaneously increasing the scale heights.

4.5.14. RECX 15

RECX 15 is an exceptional case, the only gas-rich protoplanetary disk in an otherwise rather old star formation cluster, which seems to be as small as 5 au in radius (Woitke et al. 2011, 2013). Figure 29 shows the density structure and surface

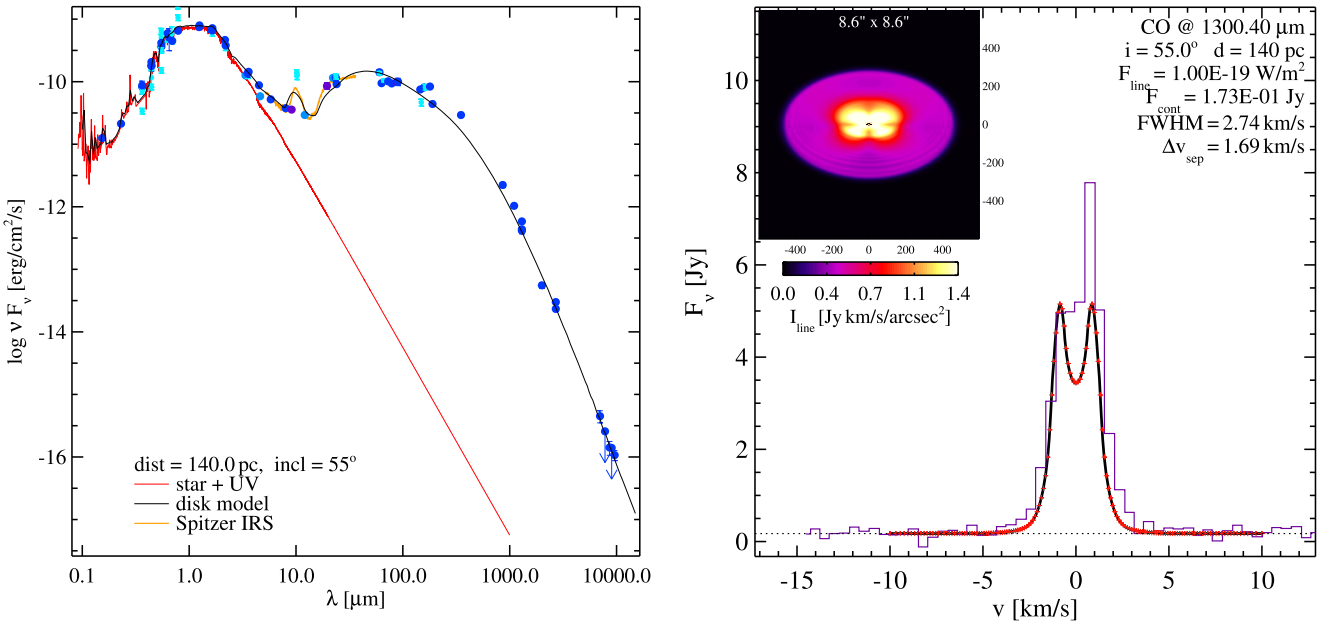

Figure 21. Left: SED-fit of GM Aur. Right: CO $J = 2$–1 line in comparison to the GM Aur data.
(A color version of this figure is available in the online journal.)

density profiles (gas and dust) for this object. RECX 15 must have lost its outer disk for some reason, possibly due to a close encounter. Only few gas lines have been detected, among them [O I] 63 μm, [O I] 6300 Å and o-H_2 2.121 μm. Our ALMA cycle-0 data shows a faint, very broad CO $J = 3$–2 line (FWHM $\approx 15\,\mathrm{km\,s^{-1}}$) which only a tiny Keplerian disk can explain (Figure 30). There is no spatially resolved data, not even with ALMA. The model manages to fit the SED (Figure 1) and the emission lines with a strongly flared, tall disk, strengthening our general conclusion that the inner disks of T Tauri stars are vertically much more extended than previously thought. The o-H_2 2.121 μm line is underpredicted by a factor 15, though. The gas/dust mass ratio is found to be $\sim$3500, an very unusual value for outer disks, but maybe not so atypical for the inner disks of transitional disks (Table 4). All line fits are summarized in Table 21.

4.6. Systematic Line Flux Deviations

We conclude this study by looking out for possible systematic weaknesses in our models, for example lines that are always predicted to be too strong or too weak. This would indicate some principle problem in our modeling assumptions or techniques, for example that certain molecules are always underabundant or overabundant with respect to observations due to an issue in the chemistry. Figures 31 and 32 show the ratios of predicted to observed line fluxes, for a sample of frequently observed emission lines. We note here again that all lines have been simultaneously fitted by one model for each object, which at the same time fits the continuum observations (SED and some images) as good as possible.

These figures do not reveal any severe weaknesses. The CO 3–2 and CO 2–1 isotopologue lines are typically well-fitted within a factor of two or better. The [O I] 6300 Å line maybe somewhat underpredicted for luminous stars, whereas the fits are fine for the T Tauri stars. The [O I] 63 μm line proves to be quite difficult to fit, we arrive at deviations within a factor 4 or less, with a slight tendency to overpredict. The other lines shown in Figure 32 show no obvious trends either. The frequently observed HCO^+ 3–2 line usually fits fine, as well as the N_2H^+ line, whereas the situation is more diverse for the HCN 3–2 and CN lines. An exception is AB Aur where the line data might be confused with foreground cloud absorption. The CO $J = 18$–17 line tends to be somewhat underpredicted by our models for the T Tauri stars.

5. Summary and Outlook

The European FP7 project DIANA has performed a coherent analysis of a large set of observational data of protoplanetary disks by means of state-of-the-art thermo-chemical disk models. We used multi-wavelength, multi-instrument, mostly archival data comprising photometry, low-resolution IR to far-IR spectra, continuum images and line observations of different kinds and different quality. Our goal was to fit all collected observational data simultaneously by means of a single disk model, separately for each object in our target list. Our aim was to conclude about the disk shape, the masses of the disks and

Table 17
Model Properties and Comparison of Computed Spectral Line Properties with Observations from GMAur.properties

DIANA Standard Fit Model Properties	
Minimum dust temperature [K]	6
Maximum dust temperature [K]	886
Mass-mean dust temperature [K]	18
Minimum gas temperature [K]	7
Maximum gas temperature [K]	26157
Mass-mean gas temperature [K]	19
mm-opacity-slope (0.85–1.3) mm	1.3
cm-opacity-slope (5–10) mm	1.7
mm-SED-slope (0.85–1.3) mm	2.4
cm-SED-slope (5–10) mm	3.5
10 μm silicate emission amplitude	1.8
Naked star luminosity [$L_\odot$]	0.7
Bolometric luminosity [$L_\odot$]	0.9
Near-IR excess ($\lambda = 2.07$–6.84 μm) [$L_\odot$]	0.03
Mid IR excess ($\lambda = 6.84$–29.9 μm) [$L_\odot$]	0.05
Far-IR excess ($\lambda = 29.9$–$998.$ μm) [$L_\odot$]	0.14

Species	λ (μm)	Line Flux (W m^{-2})		FWHM (km s^{-1})		Size (au)
		Observed	Model	Observed	Model	
O I	0.630	3.9 ± 1.0(−17)	1.2(−17)	42.0 ± 0.0	10.4	27.5
CO	4.649	1.3 ± 0.9(−18)	1.2(−16)	22.8 ± 0.0	9.0	19.4
CO	4.657	9.0 ± 8.0(−19)	8.3(−17)	15.6 ± 0.0	9.1	19.4
CO	4.699	1.0 ± 0.8(−18)	2.0(−16)	19.6 ± 0.0	9.0	19.4
CO	4.708	1.1 ± 0.8(−18)	1.9(−16)	18.0 ± 0.0	9.1	19.4
CO	4.717	1.1 ± 0.8(−18)	1.7(−16)	18.0 ± 0.0	9.1	19.4
CO	4.726	1.5 ± 0.9(−18)	1.3(−16)	26.9 ± 0.0	9.1	19.5
CO	4.735	1.6 ± 0.9(−18)	9.7(−17)	25.4 ± 0.0	9.1	19.5
CO	4.745	2.2 ± 1.1(−18)	6.7(−17)	37.2 ± 0.0	9.1	19.5
CO	4.754	2.7 ± 1.2(−18)	4.5(−17)	44.6 ± 0.0	9.1	19.5
CO	4.763	2.3 ± 1.1(−18)	3.0(−17)	35.6 ± 0.0	9.1	19.5
CO	4.773	2.9 ± 1.2(−18)	2.0(−17)	42.9 ± 0.0	9.1	19.6
CO	4.793	2.8 ± 1.2(−18)	9.1(−18)	46.3 ± 0.0	9.1	19.7
Ne^+	12.814	1.2 ± 0.3(−17)	6.8(−18)	⋯	9.5	53.3
O I	63.183	3.8 ± 0.5(−17)	7.2(−17)	⋯	5.4	230.2
o-H_2O	63.323	<7.3(−18)	4.3(−18)	⋯	9.1	20.2
CO	1300.404	1.5 ± 0.3(−19)	1.0(−19)	⋯	2.7	402.8
HCO^+	1120.478	3.9 ± 0.1(−20)	1.2(−20)	⋯	3.5	346.6

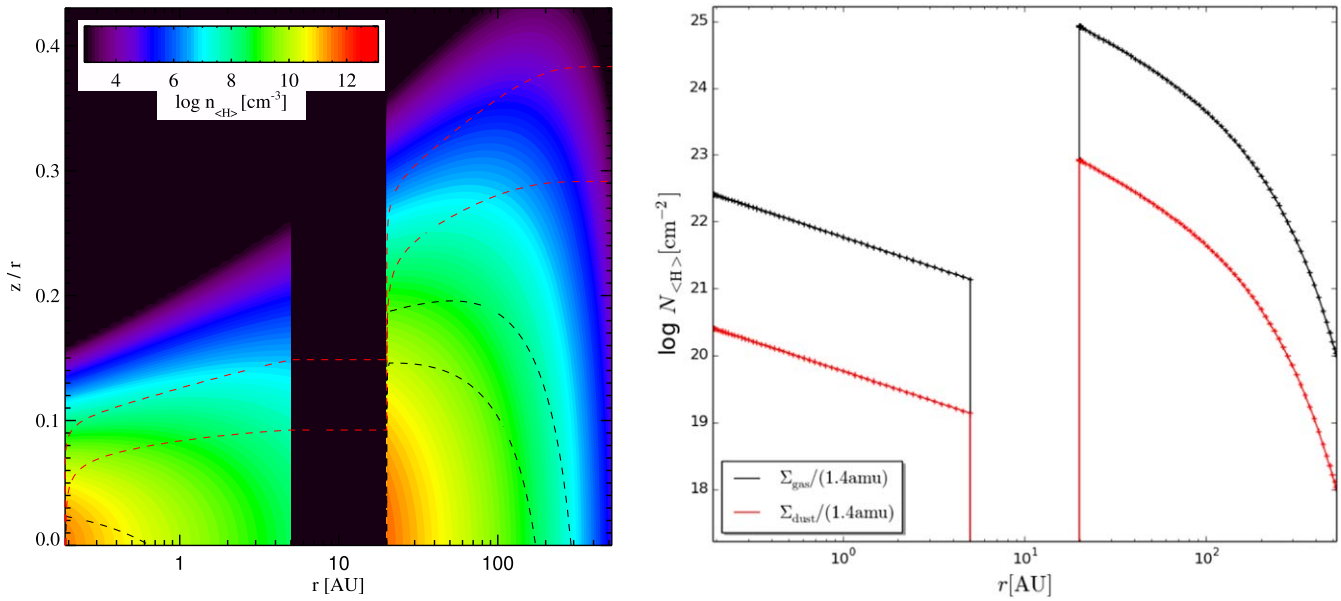

Figure 22. GM Aur density and surface density plots. For details see Figure 4. (A color version of this figure is available in the online journal.)

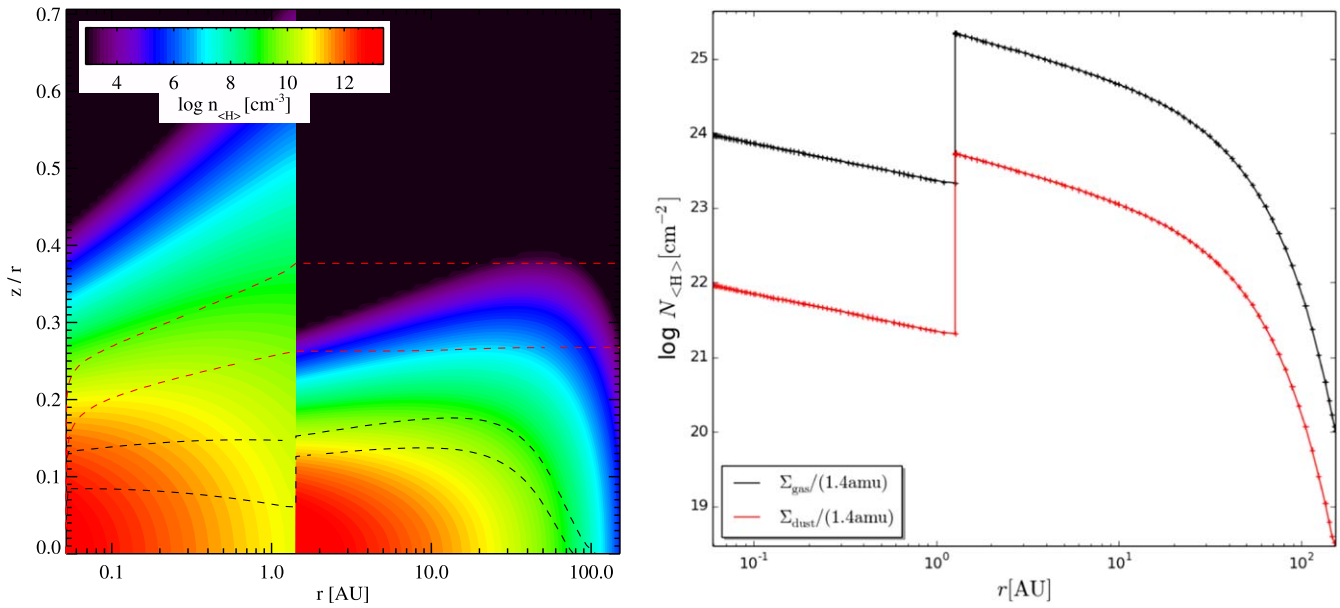

Figure 23. BP Tau density and surface density plots. For details see Figure 4. (A color version of this figure is available in the online journal.)

their physical parameters, the properties of the dust grains, the internal gas and dust temperature structures in the disks, and the chemical composition. The driving question of the project was *"does this work?"* Can we fit all available observational data with a standardized modeling approach, using 2D thermo-chemical disk models, only by varying the disk mass and shape parameters, the gas/dust ratio and the dust size and opacity parameters?

The answer is a surprisingly clear yes. In reality, disks are very complicated objects, individual, time-dependent and not strictly axi-symmetric. Yet, by allowing just for two disk zones, an inner and an outer disk, we could find parameter

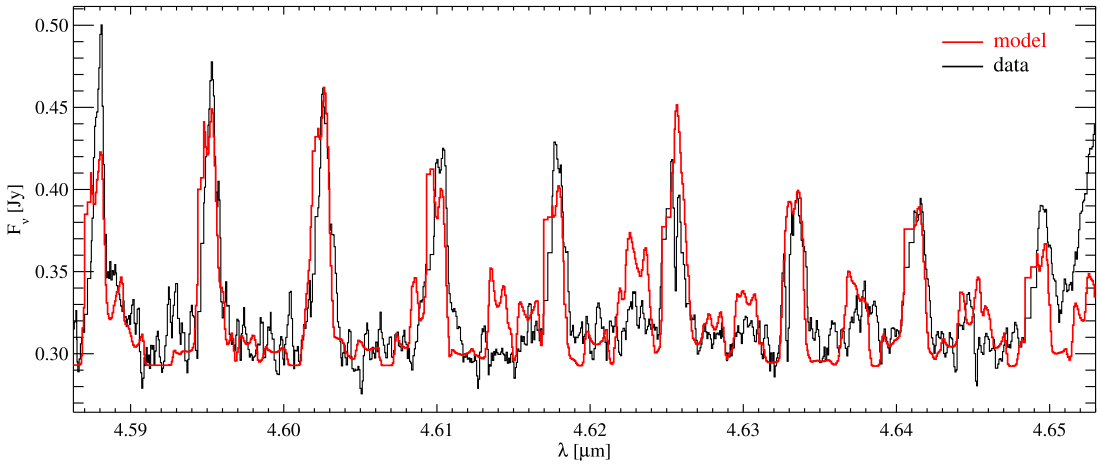

Figure 24. Model prediction and observed high-resolution Keck/NIRSPEC spectrum of the *R*-branch of fundamental CO $v = 1$–0 around 4.6 μm in BP Tau. (A color version of this figure is available in the online journal.)

combinations for our models, which predict observations that resemble most of the continuum and line data we could find, simultaneously. In particular, we did not need individual adjustments of element abundances, but achieved all our fits by using standard ISM element abundances with strongly depleted heavy elements.

Our data analysis was performed in three steps, (i) finding the stellar parameters including detailed UV and X-ray properties, (ii) using fast Monte-Carlo RT models to fit the SED in order to roughly determine the disk shape and dust opacity parameters, and (iii) using self-consistent radiation thermo-chemical models in application to an enlarged set of observational data, including all line and image data, to complete the fit. During the last modeling phase, the various disk shape, dust settling and opacity parameters were not frozen, but were continued to be varied for finding the best-fitting parameter values. This procedure distinguishes our work from most previous studies.

For most objects, however, we found at least one observation which we could not fit at all together with the other observations. This could be caused, for example, by the variability of an object or simply due to issues with foreground clouds or secondary sources in the field of view observed with different instruments. It could also be caused, of course, by some missing physics or chemistry in our models, but as Figures 31 and 32 show, we could not find any systematic problem. In case of such unclear or un-fittable data, the only practical way forward was to exclude such data or to artificially increase the respective measurement errors, otherwise the χ^2-minimization desperately tries to improve the fit of exactly those data which we trust the least. Thus, our data selection and definition of χ^2 was not mathematically sound; it was based on and required human judgment. We therefore do not claim to have found a unique solution of the disk structure of our targets.

An MCMC analysis might have revealed some interesting parameter degeneracies and credibility intervals, but was judged to be computationally unfeasible. A single thermo-chemical disk model takes about 10 CPU hours, the number of free parameters is about 20, and so hundreds of thousands of disk models would have needed to be calculated to determine those errorbars, which would have taken about 500 CPU-years for a single object.

Therefore, the intention of this project was not to determine all disk parameters with errorbars.[17] Instead, we have found some re-occurring patterns and trends in the models that helped us to better fit the data, which offers new ways to understand and explain disk observations in general, new clues for data interpretation, and useful starting points for future modeling purposes. We summarize these findings below.

Dust properties. The key to arrive at our simultaneous continuum and line fits often was to vary the dust size and opacity parameters that have an important influence on how deep the stellar UV photons penetrate into the disk, causing gas heating and line emission. We used the DIANA dust opacities for disks (Min et al. 2016b), based on a power-law dust size distribution with an effective mixture of laboratory silicate and amorphous carbon. Since our size distribution is typically extended to a few millimeters, our dust is much more transparent in the UV than standard interstellar dust, but rather opaque at 850 μm, $\kappa^{\rm abs}_{850} \approx 6.3^{+3.5}_{-2.3}$ cm^2/g(dust), which is somewhat larger than the frequently used value of 3.5 cm^2/g(dust) originally proposed by Beckwith et al. (1990) as order-of-magnitude estimate of 10 cm^2/g(dust) at 1000 GHz, and later scaled to 850 μm using $\kappa^{\rm abs}_\nu \propto 1/\lambda$.

[17] Appendix B contains a rough estimate of parameter uncertainties by probing the curvature in the local χ^2 minimum.

Table 18
Model Properties and Comparison of Computed Spectral Line Properties with Observations from BPTau.properties

DIANA Standard Fit Model Properties	
Minimum dust temperature [K]	4
Maximum dust temperature [K]	1723
Mass-mean dust temperature [K]	15
Minimum gas temperature [K]	4
Maximum gas temperature [K]	40000
Mass-mean gas temperature [K]	18
mm-opacity-slope (0.85–1.3) mm	1.4
cm-opacity-slope (5–10) mm	1.6
mm-SED-slope (0.85–1.3) mm	1.9
cm-SED-slope (5–10) mm	3.3
10 μm silicate emission amplitude	1.7
Naked star luminosity [$L_\odot$]	1.0
Bolometric luminosity [$L_\odot$]	1.3
Near-IR excess ($\lambda = 2.05$–6.90 μm) [$L_\odot$]	0.13
Mid IR excess ($\lambda = 6.90$–29.3 μm) [$L_\odot$]	0.10
Far-IR excess ($\lambda = 29.3$–$970.$ μm) [$L_\odot$]	0.03

Species	λ (μm)	Line Flux (W m^{-2})		FWHM (km s^{-1})		Size (au)
		Observed	Model	Observed	Model	
CO	1300.403	8.7 ± 2.0(−21)	1.1(−20)	4.2 ± 0.4	2.9	125.0
^{13}CO	1360.227	1.1 ± 0.5(−21)	1.5(−21)	⋯	3.8	76.2
CN	1321.390	2.4 ± 0.5(−21)	2.8(−22)	⋯	2.6	143.4
CO	4.633	1.7 ± 0.3(−17)	1.2(−17)	65.0 ± 4.0	87.0	0.6
CO	4.477	1.9 ± 0.2(−17)	1.3(−17)	70.0 ± 3.0	88.4	0.3
O I	63.183	9.5 ± 2.7(−18)	2.7(−17)	⋯	2.7	140.2
o-H_2O	63.323	<9.3(−18)	5.9(−19)	⋯	27.4	1.2

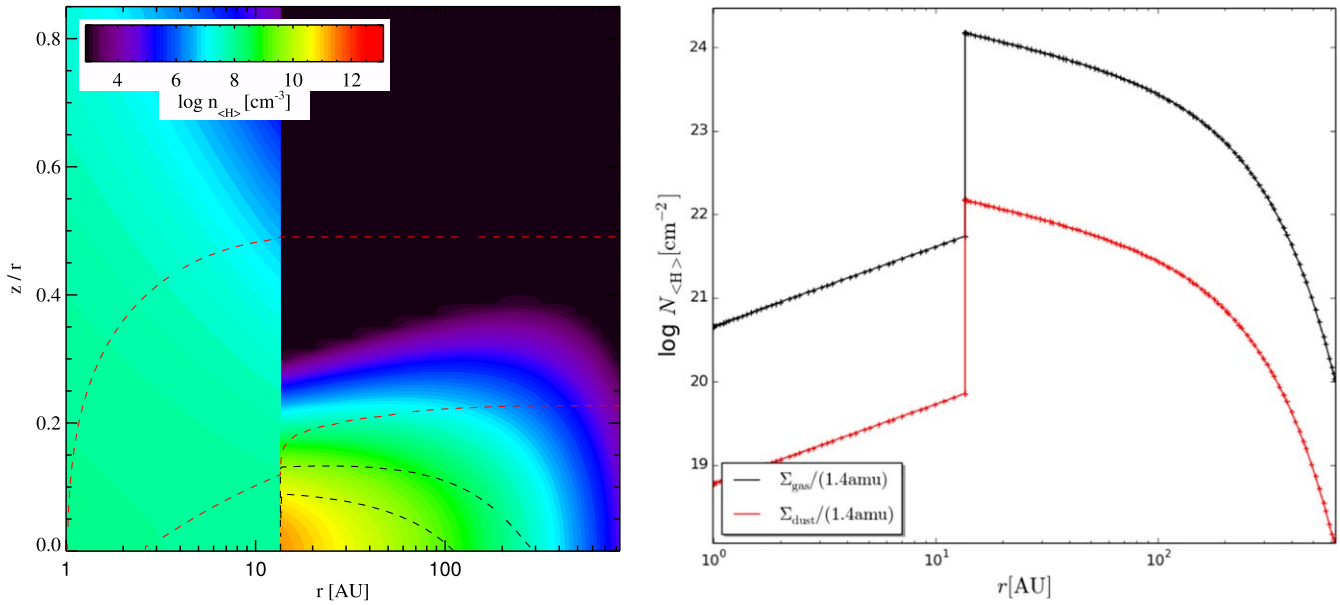

Figure 25. DM Tau density and surface density plots. For details see Figure 4. (A color version of this figure is available in the online journal.)

Dust settling. Another important degree of freedom for the fitting was the dust settling, which has opposite effects on continuum and line fluxes in the mid and far-IR, and can hence be used to break some degeneracies with disk flaring as known from pure SED-fitting. Our results suggest that dust settling is rather strong in these disks, and hence the turbulence rather weak, $\log_{10}\alpha_{\rm set} = -2.9 \pm 0.9$ as compared to the standard value of 10^{-2}. This is in agreement with the analysis by Pinte et al. (2016) of the HL Tau rings as seen with ALMA.

PAH properties. Our simultaneous fits of the PAH properties in protoplanetary disks show an underabundance of PAHs $f_{\rm PAH} \approx 0.005$–$0.8$ with respect to the standard abundance in the ISM ($10^{-6.52}$ PAH molecules/H-nucleus Tielens 2008), with large individual scatter. The PAH abundance is relevant to the model, in particular, by converting blue and soft UV photon energies into heat, which leads to additional line emission. We have solely considered small PAHs (circumcononene) with 54 carbon atoms, and our fits to a few Herbig Ae stars, where multiple mid-IR PAH emission features have been detected, show that these PAHs are mostly charged (60%–98%). We did not consider PAHs in disk gaps as discussed by Maaskant et al. (2014).

Two-zone disks. In 18 out of 27 cases, we decided to switch from a one-zone disk setup to a two-zone setup already during the SED-fitting phase. This was found to be necessary to fit certain properties in the photometric and low-resolution spectroscopic data including the PAH emission features. Some of these objects are well-known transitional disks, but for others this is not so clear, for example CY Tau, where the SED points to a massive yet very cold outer disk. Such disk properties can be produced by setting up a semi-transparent tall inner disk that casts a shadow onto the outer disk.

Gas-rich, tall inner disks. The two-zone scenario was often found to be useful to explain objects with very faint far-IR lines. In fact, 12 out of our 14 completed DIANA standard models used a two-zone setup. These tall inner disks shield the outer disk from the UV irradiation by the star, hence lead to less disk heating and line emission. Such inner disks do not obey the condition of hydrostatic equilibrium, in particular those of the T Tauri stars, so their nature can be disputed. However, we could not find any observation that could rule out such a scenario. On the contrary, having that tenuous, tall inner disk definitely helps to explain some of the strong optical lines (such as [O I] 6300 Å) and strong near-IR lines (such as CO fundamental), which are preferentially emitted by these inner disks. Interestingly, the gas/dust ratio in these inner disk zones was often found to be large, up to 90,000 for HD 163296, but never smaller than the standard value of 100.

Dust masses and cold disks. We found that the classical dust mass-determination method according to Equation (13) seems not entirely justified. According to our results, disks can be very cold in the midplane <10 K, and since a large fraction of the disk mass resides in those cold midplane areas, emission at 850 μm is generally far less intense than expected from the

Table 19
Model Properties and Comparison of Computed Spectral Line Properties with Observations from DMTau.properties

DIANA Standard Fit Model Properties	
Minimum dust temperature [K]	5
Maximum dust temperature [K]	242
Mass-mean dust temperature [K]	9
Minimum gas temperature [K]	5
Maximum gas temperature [K]	15978
Mass-mean gas temperature [K]	13
mm-opacity-slope (0.85–1.3) mm	1.0
cm-opacity-slope (5–10) mm	1.3
mm-SED-slope (0.85–1.3) mm	2.1
cm-SED-slope (5–10) mm	3.1
10 μm silicate emission amplitude	2.0
Naked star luminosity [$L_\odot$]	0.3
Bolometric luminosity [$L_\odot$]	0.4
Near-IR excess ($\lambda = 2.02$–6.72 μm) [$L_\odot$]	0.00
Mid IR excess ($\lambda = 6.72$–29.5 μm) [$L_\odot$]	0.02
Far-IR excess ($\lambda = 29.5$–$991.$ μm) [$L_\odot$]	0.04

Species	λ (μm)	Line Flux (W m^{-2})		FWHM (km s^{-1})		Size (au)
		Observed	Model	Observed	Model	
Ne^+	12.814	5.5 ± 1.1(−18)	3.3(−17)	⋯	15.3	7.4
O I	63.183	7.0 ± 2.0(−18)	4.6(−17)	⋯	3.0	331.6
O I	145.525	<3.6(−18)	1.2(−18)	⋯	8.5	164.3
C II	157.740	<3.6(−18)	4.5(−18)	⋯	1.5	565.0
o-H_2O	63.323	<5.4(−18)	8.8(−19)	⋯	9.3	11.9
CO	866.963	1.9 ± 0.1(−19)	3.7(−19)	⋯	1.8	448.9
CO	1300.404	1.1 ± 0.3(−19)	1.2(−19)	⋯	1.8	443.9
^{13}CO	1360.227	4.0 ± 0.5(−20)	1.8(−20)	⋯	2.2	324.3
$C^{18}O$	1365.421	5.0 ± 0.5(−21)	3.8(−21)	⋯	2.4	289.5
CN	881.097	6.7 ± 0.7(−20)	1.6(−19)	⋯	1.7	470.5
CN	1321.390	3.6 ± 0.3(−20)	6.5(−20)	⋯	1.6	482.0
HCN	845.663	1.9 ± 0.2(−20)	1.2(−19)	⋯	1.8	415.3
HCN	1127.520	2.6 ± 0.5(−20)	7.6(−20)	⋯	1.7	440.5
HCO^+	840.380	7.5 ± 0.4(−20)	7.2(−20)	⋯	1.8	439.8
HCO^+	1120.478	4.8 ± 0.1(−20)	4.4(−20)	⋯	1.7	461.8
N_2H^+	804.439	<6.7(−21)	1.2(−20)	⋯	2.0	273.2
N_2H^+	1072.557	9.3 ± 0.9(−21)	7.1(−21)	⋯	2.0	289.6

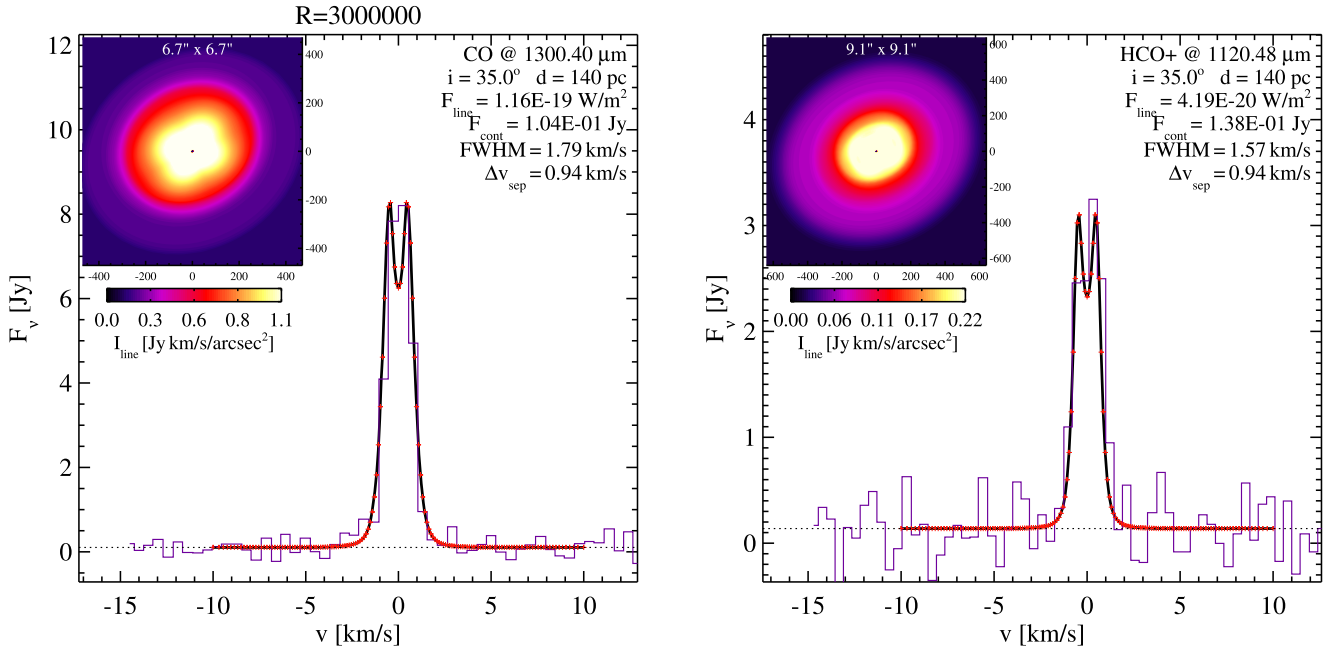

Figure 26. Left: CO 2–1 line flux and velocity profile in comparison to SMA data of DM Tau. Right: Same for HCO^+ 3–2 line at 1.12 mm.
(A color version of this figure is available in the online journal.)

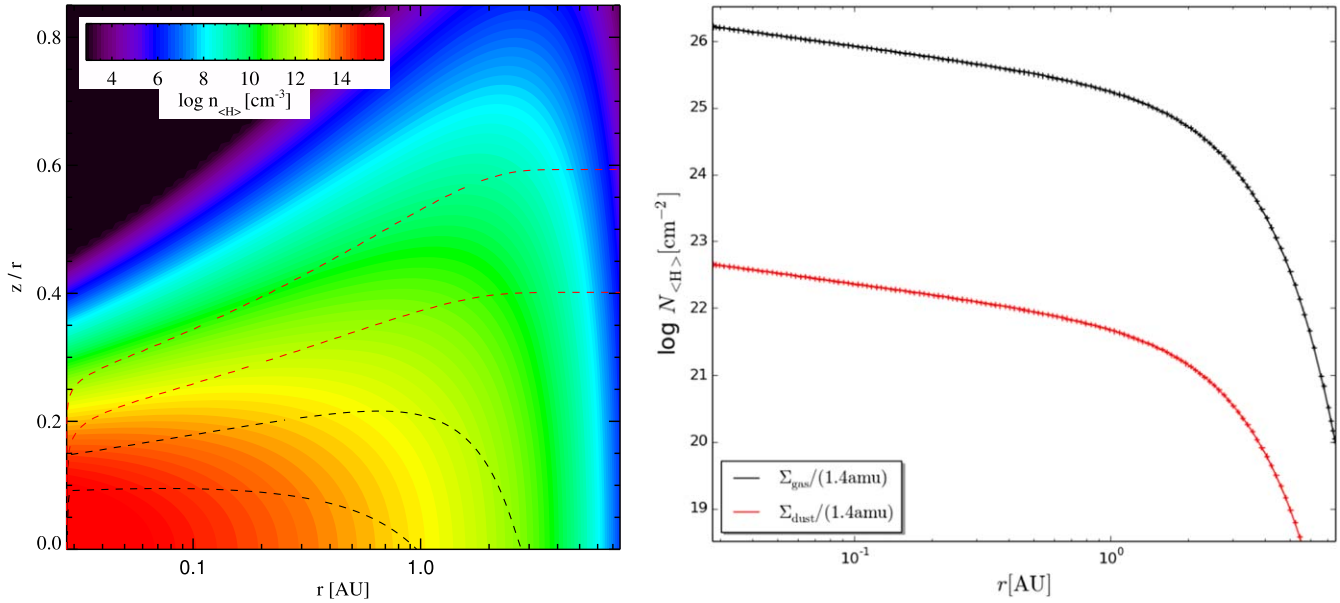

Figure 27. CY Tau density and surface density plots. For details see Figure 4.
(A color version of this figure is available in the online journal.)

Rayleigh–Jeans limit. This finding is supported by Guilloteau et al. (2016) who found temperatures as low as 5–7 K for the large grains in the Flying Saucer. We find the mean disk temperatures to vary by an order of magnitude among individual disks. Disks can be optically thick even at mm-wavelengths. We therefore found disk masses that are often much larger than stated elsewhere, see Table 7. The determination of dust sizes from the SED millimeter-slope is equally affected by these physical effects. We found that the dust mm-opacity-slope is only weakly correlated to the resulting SED-slope.

Dust/gas ratio. Concerning the gas/dust ratio in the outer disk, our results are inconclusive. Disregarding those DIANA

Table 20
Model Properties and Comparison of Computed Spectral Line Properties with Observations from CYTau.properties

DIANA Standard Fit Model Properties	
Minimum dust temperature [K]	5
Maximum dust temperature [K]	1683
Mass-mean dust temperature [K]	9
Minimum gas temperature [K]	5
Maximum gas temperature [K]	40000
Mass-mean gas temperature [K]	12
mm-opacity-slope (0.85–1.3) mm	1.3
cm-opacity-slope (5–10) mm	1.7
mm-SED-slope (0.85–1.3) mm	1.6
cm-SED-slope (5–10) mm	3.0
10 μm silicate emission amplitude	1.6
Naked star luminosity [$L_\odot$]	0.4
Bolometric luminosity [$L_\odot$]	0.5
Near-IR excess ($\lambda = 2.07$–6.96 μm) [$L_\odot$]	0.06
Mid IR excess ($\lambda = 6.96$–29.5 μm) [$L_\odot$]	0.03
Far-IR excess ($\lambda = 29.5$–$973.$ μm) [$L_\odot$]	0.01

Species	λ (μm)	Line Flux (W m^{-2})		FWHM (km s^{-1})		Size (au)
		Observed	Model	Observed	Model	
CO	1300.403	1.6 ± 0.3(−20)	2.0(−20)	2.4 ± 0.2	2.3	199.7
^{13}CO	1360.227	7.8 ± 0.9(−21)	6.0(−21)	2.5 ± 0.2	2.6	199.3
O I	63.183	1.2 ± 0.1(−17)	5.6(−18)	⋯	3.2	143.2
O I	0.630	7.8 ± 0.5(−18)	9.4(−18)	42.0 ± 3.0	59.0	0.4
o-H_2O	63.323	<1.2(−17)	1.4(−19)	⋯	29.8	0.7
CO	4.633	6.0 ± 2.0(−18)	6.6(−18)	75.0 ± 11.0	14.0	4.1
CO	4.920	5.0 ± 1.0(−18)	4.2(−18)	86.0 ± 9.0	92.1	0.1

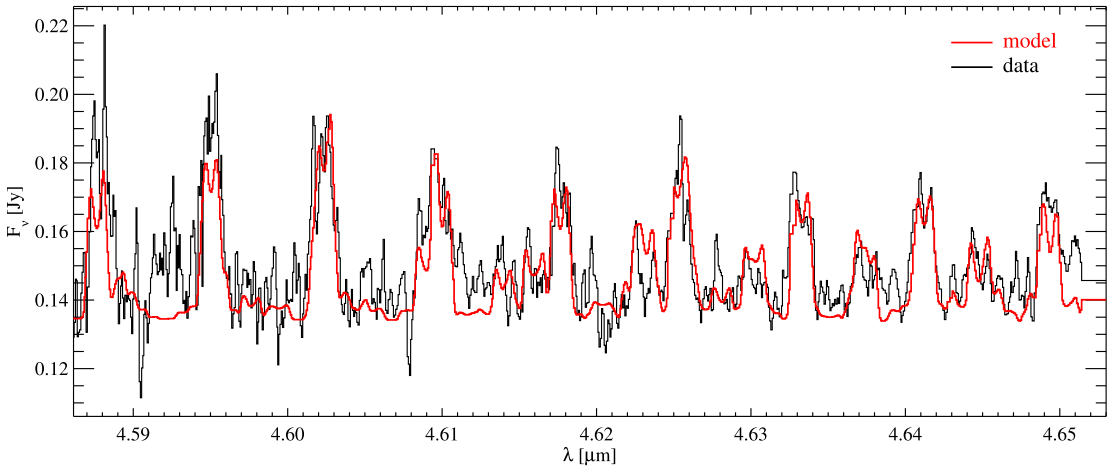

Figure 28. Comparison of the observed and modeled CO rovibrational spectrum with continuum.
(A color version of this figure is available in the online journal.)

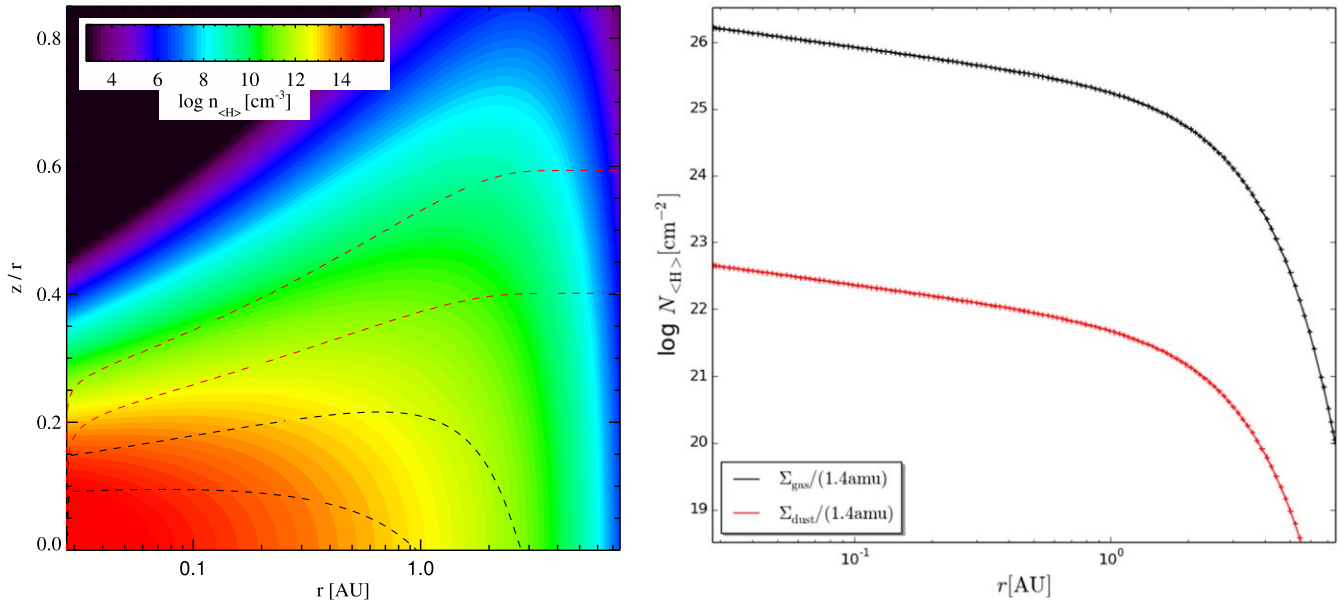

Figure 29. RECX 15 density and surface density plots. For details see Figure 4.
(A color version of this figure is available in the online journal.)

standard models where gas/dust = 100 was enforced, the remaining 8 models have gas/dust = 120^{+170}_{-70}.

We offer all collected observational data at http://www.univie.ac.at/diana and provide all modeling results at http://www-star.st-and.ac.uk/~pw31/DIANA/DIANAstandard. The 2D physico-chemical structures of our objects can be downloaded from these internet portals for further inspection and analysis. All model parameters are offered in an easy-to-use format, see Appendix A, and all users of `MCFOST`, `MCMax` or `ProDiMo` can download setup files to re-run our disk models. This ensures the transparency of our modeling work, and their re-use in future applications.

The use of the DIANA disk models beyond the project has already started. Stolker et al. (2017) used the DIANA SED model for the interpretation of multi-epoch VLT/SPHERE scattered light images of HD 135344B. They use our model to

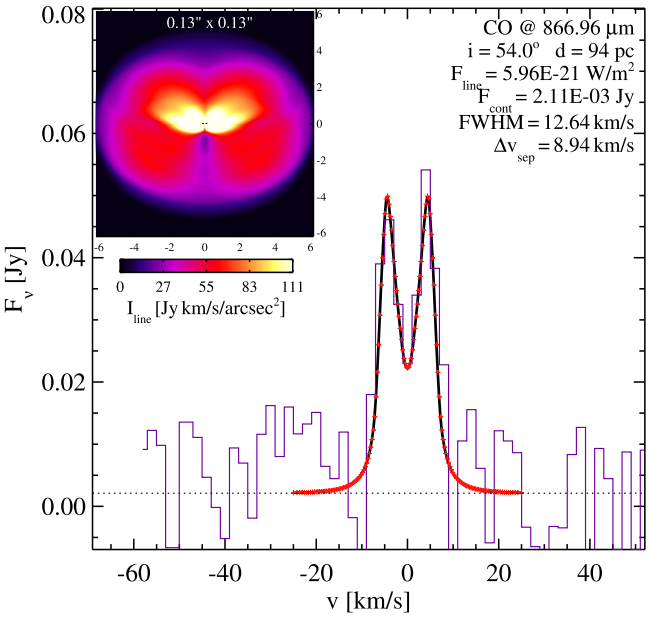

Figure 30. Model fit to our CO 3–2 ALMA cycle-0 observations of RECX 15. (A color version of this figure is available in the online journal.)

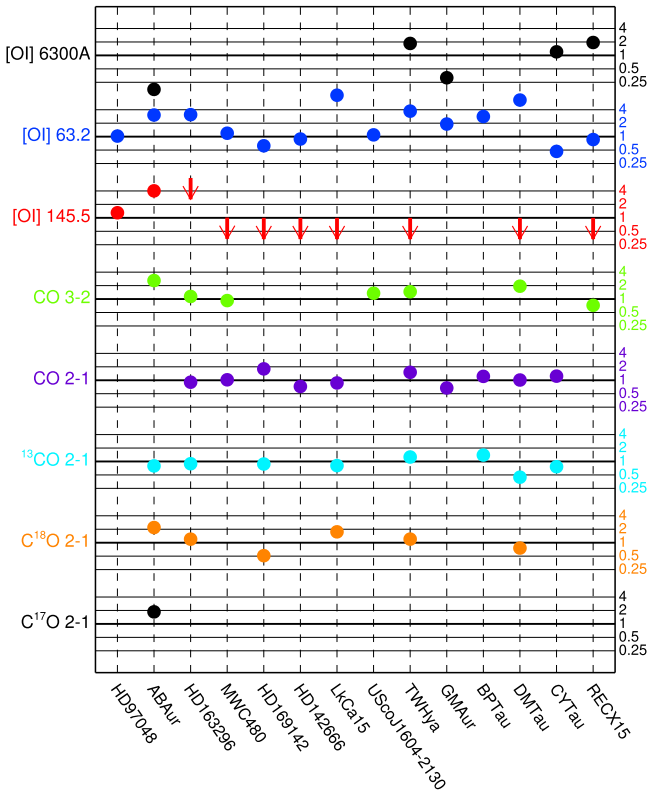

Figure 31. Summary of line fitting results from the DIANA-standard models. The y-axis shows the line fluxes as predicted by the models divided by the observed line fluxes $F_{\rm line}^{\rm mod}/F_{\rm line}^{\rm obs}$ on log-scalings as indicated on the right. If a dot is positioned at 0.5, for example, it means that the model underpredicts the line flux by a factor of 2. An arrow indicates that the observation is an upper limit. An arrow starting at 1 indicates a good match—the model predicts a line flux lower or equal to the observational 3σ upper limit. If, however, the arrow starts at 2, it means that the model predicts a line flux that is a factor 2 larger than the 3σ upper limit. Systematic errors in the observations are typically of order (10–30)%.
(A color version of this figure is available in the online journal.)

illustrate that a small misalignment between the inner and the outer disk (2.°6) can explain the observed broad, quasi-stationary shadowing in north–northwest direction. The effects of inclined inner disks on line fluxes would be worth studying in the future. As a second example, Muro-Arena et al. (2018) used the DIANA SED model of HD 163296 to analyze the combined VLT/SPHERE and ALMA continuum data set for this object. Even though clear ring structures are seen and the model is eventually refined to show a surface density modulation, the average surface density profile stays the same as in the DIANA SED model. This illustrates that in some cases, the detailed disk substructures are minor modulations of the global 2D disk models. These substructures are key for the planet formation processes, but have only little effect on global observables such SEDs and unresolved line observations that arise from an extended radial region of the disk. Lastly, the MWC 480 and Lk Ca 15 disk models can serve as an interesting starting point for the analysis of the full ALMA spectral scan (ALMA community proposal 2015.1.00657.S searching for complex molecules, led by Karin Öberg et al.). These examples illustrate the potential of the 2D disk models presented in this paper for future data analysis and interpretation, even in the realm of observed 3D disk substructures.

The authors acknowledge funding from the EU FP7-2011 under grant agreement No. 284405. J.D.I. gratefully acknowledges support from the DISCSIM project, grant agreement 341137, funded by the European Research Council under ERC-2013-ADG. Astrophysics at Queen's University Belfast is supported by a grant from the STFC (ST/P000312/1). O.D. acknowledges the support of the Austrian Research Promotion Agency (FFG) to the project JetPro, funded within the framework of the Austrian Space Applications Program (ASAP) FFG-854025. This paper makes use of the following ALMA data: RECX 15: ADS/JAO.ALMA#2011.0.00133.S (RECX 15) and ADS/JAO.ALMA#2011.0.00629.S (DM Tau and MWC 480). ALMA is a partnership of ESO (representing its member states), NSF (USA) and NINS (Japan), together with NRC (Canada) and NSC and ASIAA (Taiwan) and KASI (Republic of Korea), in cooperation with the Republic of Chile. The Joint ALMA Observatory is operated by ESO, AUI/NRAO and NAOJ.

Table 21
Model Properties and Comparison of Computed Spectral Line Properties with Observations from RECX15.properties

DIANA Standard Fit Model Properties	
Minimum dust temperature [K]	32
Maximum dust temperature [K]	1396
Mass-mean dust temperature [K]	86
Minimum gas temperature [K]	44
Maximum gas temperature [K]	26982
Mass-mean gas temperature [K]	116
mm-opacity-slope (0.85–1.3) mm	0.8
cm-opacity-slope (5–10) mm	1.6
mm-SED-slope (0.85–1.3) mm	2.5
cm-SED-slope (5–10) mm	3.5
10 μm silicate emission amplitude	1.4
Naked star luminosity [$L_\odot$]	0.1
Bolometric luminosity [$L_\odot$]	0.2
Near-IR excess ($\lambda = 2.02$–6.72 μm) [$L_\odot$]	0.02
Mid IR excess ($\lambda = 6.72$–29.5 μm) [$L_\odot$]	0.02
Far-IR excess ($\lambda = 29.5$–$991.$ μm) [$L_\odot$]	0.01

Species	λ (μm)	Line Flux (W m^{-2})		FWHM (km s^{-1})		Size (au)
		Observed	Model	Observed	Model	
CO	866.963	8.2 ± 0.6(−21)	6.0(−21)	14.9 ± 2.3	12.6	5.4
O I	63.183	3.0 ± 0.3(−17)	2.6(−17)	⋯	13.8	6.0
O I	0.630	6.5 ± 2.5(−17)	1.3(−16)	38.0 ± 10.0	20.8	3.4
o-H_2	2.121	2.5 ± 0.1(−18)	1.7(−19)	18.0 ± 1.2	66.9	2.0
O I	145.525	<6.0(−18)	1.4(−18)	⋯	13.2	5.5
C II	157.740	<9.0(−18)	1.8(−19)	⋯	14.0	6.0
CO	90.162	<9.6(−18)	7.3(−19)	⋯	19.9	3.7
CO	79.359	<2.4(−17)	5.6(−19)	⋯	25.0	2.3
CO	72.842	<8.1(−18)	4.7(−19)	⋯	28.7	2.1
o-H_2O	180.488	<5.1(−18)	9.2(−20)	⋯	24.2	4.3
o-H_2O	179.526	<5.1(−18)	1.2(−19)	⋯	20.1	4.8
o-H_2O	78.742	<3.0(−17)	1.2(−18)	⋯	21.3	4.8
p-H_2O	89.988	<9.6(−18)	6.8(−19)	⋯	24.2	4.4

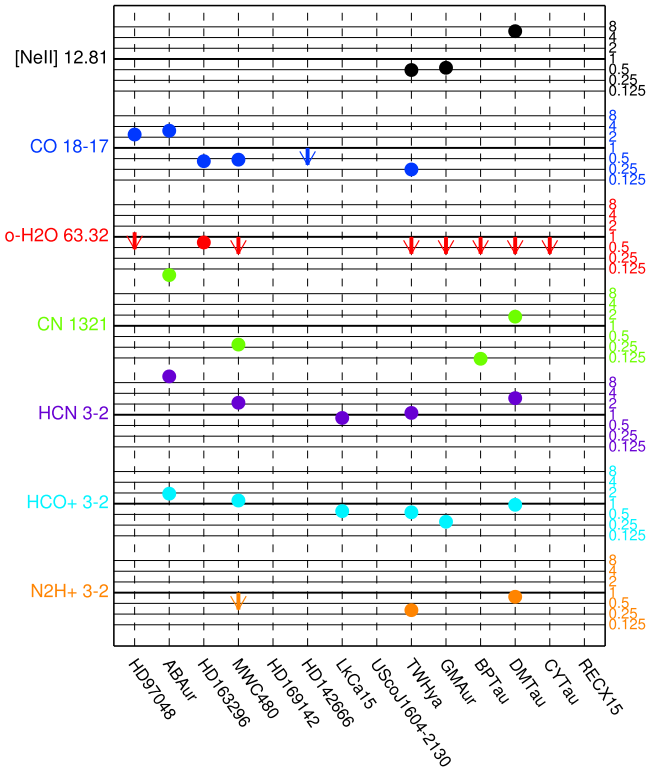

Figure 32. Continued from Figure 31.
(A color version of this figure is available in the online journal.)

Appendix A
Uploaded Model Data

The model data uploaded to the DIANA database[18] are organized in five sets:

1. {object-name}.para,
2. {object-name}.properties,
3. {object-name}_DIANAfit.ps.gz,
4. {object-name}_ModelOutput.tgz, and
5. {object-name}_ModelSetup.tgz.

Examples of the .para and .properties files are shown in Figures 33 and 34, respectively.

The .para files contain the complete set of modeling parameters, as well as a few quantities related to the stellar properties. These values are listed in a generic form to make them readable even to end-users not working with ProDiMo, MCFOST or MCMax. The different blocks of the .para files (see Figure 33) list the parameter names and units of the stellar parameter, some observational parameters like distance and inclination, two essential switches (one or two-zone model? PAHs included in RT?), the dust material and settling parameters, the PAH parameters, the gas parameters, as well as the disk shape, mass, and dust size parameters separately for the inner (for two-zone models) and the outer disk zones. The meaning of all physical quantities is explained in Woitke et al. (2016).

The .properties files contain a selection of important model output quantities, as well as some predicted observations, see Figure 34. The first block contains minimum, maximum and mean values of the gas and dust temperatures in the disk. The second block lists total masses of chemicals, and mean values thereof, for example,

$$\langle T_{\rm gas}^{\rm H_2} \rangle = \frac{\int T_{\rm gas}\, n_{\rm H_2}\, dV}{\int n_{\rm H_2}\, dV}, \qquad (20)$$

where $n_{\rm H_2}$ is the particle density of molecular hydrogen, $T_{\rm gas}$ the gas temperature, and $\int dV$ is the integration in cylindrical coordinates over radius r and height over midplane z in the disk. In the shown example, we find the mean gas temperature of atomic hydrogen to be ≈660 K and the mean gas temperature of molecular hydrogen to be ≈21 K.

The next block summarizes some predictions of directly observable continuum properties, such as the millimeter and centimeter slopes, the amplitude of the 10 μm silicate emission feature, and near-IR, mid-IR and far-IR excesses, followed by two blocks which contain the model SED computed by MCFOST and ProDiMo, the latter comes with an apparent size at all wavelengths, i.e., the radius of a circle in the image plane which contains 95% of the spectral flux. The apparent sizes are derived without convolution with any instrumental PSF, and are computed without direct starlight.

The second block from the bottom shows predictions and properties of a generic sample of 102 spectral emission lines. The name of the atom or molecule, the line center wavelength, the total line flux, the continuum flux, the FWHM of the line velocity-profile, the apparent size of the line emitting region (as above), and averages of density, gas and dust temperature and optical extinction over the line emitting regions. Studying the output for the CO isotopologue lines around 1.3 mm shows that the ^{12}CO line comes from less dense but warmer gas, whereas the ^{13}CO, C^{18}O and C^{17}O lines originate in successively cooler and deeper disk layers. Note that $\langle T_{\rm gas}\rangle \approx \langle T_{\rm dust}\rangle$ for all CO isotopologue lines, whereas the [O I] 63 μm line has $\langle T_{\rm gas}\rangle > \langle T_{\rm dust}\rangle$. This information is available for all 102 lines for all finished DIANA standard models.

The last block compares observed with predicted line properties including line fluxes, FWHMs and apparent sizes. In the case of TW Hya, 57 line observations have been collected, and accounted for in the fitting of the model parameters.

The DIANAfit.ps.gz files contain graphical output pages of the following model results: 2D-density structure (gas and dust), gas/dust ratio, mean dust sizes, column density structure,

[18] http://www.univie.ac.at/diana, see also http://www-star.st-and.ac.uk/~pw31/DIANA/SEDfit/SEDmodels_index.html and http://www-star.st-and.ac.uk/~pw31/DIANA/DIANAstandard for direct access.

```
================================
 DIANA standard model parameters
================================

----------------------------------------
            object =               TWHya
----------------------------------------
               Mstar [Msun] =              0.7500
                   Teff [K] =             4000.00
               Lstar [Lsun] =              0.2420
               Rstar [Rsun] =              1.0888
                     log(g) =              4.2389
   L_UV (91.2-205 nm) [Lsun] =          1.2836E-05
   L_UV (91.2-111 nm) [Lsun] =          3.0319E-06
       L_X (>0.1 keV) [Lsun] =          7.6790E-04
       L_X (1-10 keV) [Lsun] =          7.0413E-05
          Mdot [Msun/yr] =              1.5000E-09
         interstellar A_V =                  0.1999
         interstellar R_V =                  3.1000
-------------------------------------------------
             distance  [pc] =                51.0
          inclination [deg] =                 7.0
              disk PA [deg] =                n.a.
                 disk zones =                   2
                 PAHs in RT =              .false.
----------------- dust parameters -----------------
      Mg0.7Fe0.3SiO3 [Vol%] =              0.5010
           amC-Zubko [Vol%] =              0.2490
              vacuum [Vol%] =              0.2500
               alpha_settle =          5.2351E-03
----------------- PAH parameters ------------------
         ratio charged PAHs =                n.a.
     number of carbon atoms =             54.0000
   number of hydrogen atoms =             18.0000
----------------- gas parameters ------------------
 chemical heating efficiency =              0.0180
  turbulent velocity [km/s] =              0.1000
          type of chemistry =   large DIANA standard with D
------------------- inner zone --------------------
            gas mass [Msun] =          1.0503E-06
           dust mass [Msun] =          1.3266E-09
         inner radius [AU] =                0.0781
         outer radius [AU] =                4.5784
       col.dens.power-index =              -0.7788
    scale height @ 1AU [AU] =                0.0279
            flaring index =                 1.2052
   minimum dust radius [mic] =             0.00114
   maximum dust radius [mic] =             5734.897
      size-dist. power-index =                3.9926
                       fPAH =                0.0080
------------------- outer zone --------------------
       disk gas mass [Msun] =          4.4769E-02
      disk dust mass [Msun] =          1.0142E-04
         inner radius [AU] =                4.5784
    tapering-off radius [AU] =               48.0055
         outer radius [AU] =              192.9500
       col.dens.power-index =                1.5181
    tapering-off power-index =                0.4452
   scale height @ 100AU [AU] =                6.2615
            flaring index =                 1.2121
   minimum dust radius [mic] =             0.00114
   maximum dust radius [mic] =                5734.9
      size-dist. power-index =                3.9926
                       fPAH =                0.0806
```

Figure 33. Example file TWHya.para which contains all model parameters of the TW Hya disk model in an easy to understand, simple generic format.

```
====================================
 DIANA standard fit model properties
====================================

----------------------------------------
            object =               TWHya
----------------------------------------
      minimum dust temperature [K] =        7.24
      maximum dust temperature [K] =     1112.40
    mass-mean dust temperature [K] =       21.05
      minimum  gas temperature [K] =        7.35
      maximum  gas temperature [K] =    40000.00
    mass-mean  gas temperature [K] =       21.29
------ species masses and mass-mean temperatures --------
     240 species
    species mass[Msun]  <Tgas>[K] <Tdust>[K]       <AV>
         e-  4.924E-13    5659.18      65.89  7.630E-01
         H+  7.613E-10    6088.93      66.04  8.591E-01
          H  3.304E-07     664.48      58.94  6.566E-03
         H2  3.219E-02      21.29      21.28  1.404E+03
...
---------------- continuum properties -------------------
     mm-opacity-slope (0.85-1.3)mm =      1.2244
         cm-opacity-slope (5-10)mm =      1.3924
         mm-SED-slope (0.85-1.3)mm =      2.1526
            cm-SED-slope (5-10)mm =      3.0310
 10mic silicate emission amplitude =      2.1760
      naked star luminosity [Lsun] =      0.2719
      bolometric luminosity [Lsun] =      0.3455
             near IR excess [Lsun] =  6.8858E-03    (lam=2.02-6.99mic)
              mid IR excess [Lsun] =  2.7334E-02    (lam=6.99-29.4mic)
              far IR excess [Lsun] =  3.6517E-02    (lam=29.4-972.mic)
...
---------------------- MCFOST SED ------------------------
         125 points
    lam[mic]     Fnu[Jy]
  9.2100E-02  6.4362E-05
  9.3928E-02  2.8237E-04
  9.5791E-02  4.7802E-04
...
------------------ ProDiMo SED and apparent size -------------------
         300 points
    lam[mic]     Fnu[Jy]  size[AU]
...
  1.0012E+00  7.1632E-01  3.7740E+01
  1.0409E+00  7.4734E-01  3.7515E+01
  1.0821E+00  7.7549E-01  3.7258E+01
...
----------------------  line properties  ---------------------------
     102 lines
       lam[mic] lflux[W/m2]  Fcont[Jy] FWHM[km/s]  size[AU]  <nH>[cm-3] <Tgas>[K] <Tdust>[K]        <Av>
   CO  1300.403  1.6578E-19  0.615366       0.814   162.399  3.1274E+07    43.035     45.311  2.6194E-02
 13CO  1360.228  2.5141E-20  0.554141       0.966   123.788  3.1151E+08    34.579     34.692  1.8789E-01
 C18O  1365.430  6.0085E-21  0.549196       1.061   109.722  5.3079E+08    33.173     33.199  2.8603E-01
 C17O  1334.098  1.9415E-21  0.579859       1.082   106.615  5.9306E+08    33.130     33.146  3.0820E-01
 HCO+  1120.478  6.5941E-20  0.861775       0.793   177.482  2.0272E+07    24.738     25.303  3.3364E-02
 [OI]    63.183  1.3759E-16  4.619789       1.325    97.677  4.4558E+07    94.968     71.085  1.0940E-02
...
------------ comparison observed/model line properties -------------
      57 spectral lines
          lam[mic]      obs.lineflux[W/m2]       model  obs.FWHM[km/s]    model   size[AU]
OI       63.18367060   3.70E-17 +/- 1.00E-18  1.3761E-16  0.00 +/-  0.00   1.3281 9.7579E+01
o-H2O    20.34147403   5.20E-18 +/- 2.00E-18  1.8208E-17  0.00 +/-  0.00  11.3296 7.7652E-01
o-H2O    23.85979742   1.10E-17 +/- 2.00E-18  2.5681E-17  0.00 +/-  0.00  10.1508 2.1124E+00
o-H2O    25.36599169   6.60E-18 +/- 2.00E-18  2.6824E-17  0.00 +/-  0.00   9.8190 3.4773E+00
o-H2O    30.52542262   2.40E-17 +/- 2.00E-18  2.4765E-17  0.00 +/-  0.00   8.9982 4.7101E+00
o-H2O    30.87089842   1.60E-17 +/- 2.00E-18  2.0718E-17  0.00 +/-  0.00   9.2165 4.5666E+00
...
```

Figure 34. Example file TWHya.properties which contains a collection of important physico-chemical results and predictions of observational quantities from the model, such as continuum and line fluxes, apparent sizes, FWHM of lines, etc. Note the "..." in the figure which means that a number of lines have been omitted here for clarity. Mean value $\langle . \rangle$ refer to averages over the specific line emission regions. The size [au] is the radius of a circle in the image plane that contains 95% of the flux.

scale height as function of radius, UV field-strength χ, radial optical depths for UV photons and X-rays, X-ray ionization rate ζ_X, dust, gas and PAH temperature structures, chemical and cooling relaxation timescales, Rosseland-mean dust opacity, sound speed, the most important heating and cooling processes, mean dust opacity as function of wavelength, SED, magnification of mid-IR region, apparent size and continuum emission regions as function of wavelength, enlargements of SED in selected spectral windows with emission lines overplotted, continuum images at near-IR to mm wavelengths, comparison of model to observed intensity profiles after PSF-convolution, concentration of selected chemicals as 2D-contour plots, 2D-plots of the line emission regions that produce >50% of the line flux (available for all 102 generic emission lines),

computed velocity profiles for the observed lines in comparison to the data (where available), and line intensity plots (after averaging over θ in concentric rings) as function of r.

The ModelOutput.tgz files contain all model output data as listed above (and more) in numerical tables where each line corresponds to a (r, z)-point in the model. These data can be used, for example, to make your own plots, for example to look for the various ice-lines.

The ModelSetup.tgz files contain all numerical input and data-files necessary to recompute the model. These files are included in the format required for `ProDiMo`, `MCFOST` and `MCMAX`. The data-files include the observational data in the "model-friendly" input format requested by `ProDiMo`.

Appendix B
Uncertainties in Disk Parameter Determination

Our derived values of the model parameter concerning disk shape, gas, dust and PAH parameters are subject to large uncertainties, partly due to measurement errors and calibration uncertainties of the astronomical instruments used, but partly also due to well-known fitting degeneracies, in particular if the disk model is only fitted to SED data.

Absolute measurement errors are typically 10%–30%, for example due to calibration uncertainties, usually larger than the quoted measurement uncertainties. This is particularly relevant for multi-instrument data as we consider in this paper. Another source for uncertainties are numerical errors. For computational grid sizes 100×100 as used here, line flux predictions from the models are uncertain by about 10% (Woitke et al. 2016, see Appendix F therein) due to numerical problems to properly resolve the sometimes very small (i.e., very thin) line forming regions.

A proper resolution of all modeling uncertainties and degeneracies would require a Bayesian analysis, which needs about 10^6 models for each object in a $\sim$20-dimensional parameter space. After careful consideration, the team decided *not* to perform such a Bayesian analyses, because it would surpass our already considerable numerical efforts in this project to determine the χ^2 minimums by a large factor.

However, to get a rough impression of our modeling uncertainties, we consider here some deviations dp_j from the best values $p_j^{\rm opt}$ of parameter j in both directions from the local χ^2-minimum as

$$\chi^2_{\rm min} = \chi^2(p_j^{\rm opt}), \tag{21}$$

$$\chi^2_{j+} = \chi^2(p_j^{\rm opt} + \delta_{j,j'}\, dp_{j'}), \tag{22}$$

$$\chi^2_{j-} = \chi^2(p_j^{\rm opt} - \delta_{j,j'}\, dp_{j'}), \tag{23}$$

and then fit a parabola to the three points $\{\chi^2_{j-}, \chi^2_{\rm min}, \chi^2_{j+}\}$ in each parameter dimension j to (i) check whether the best parameter value $p_j^{\rm opt}$ actually sits in a multi-dimensional minimum as expected, and (ii) to determine the distance Δp_j by which parameter j can be varied, until a considerable worsening of the fit is obtained as

$$\chi^2(p_j^{\rm opt} + \delta_{j,j'}\, \Delta p_{j'}) = \chi^2_{\rm min} + 0.1. \tag{24}$$

Typically, our best fits have $\chi_{\rm min} \approx 1 \ldots 3$. The constant offset of 0.1 is chosen "by eye," such that a human can effortlessly identify the best fitting model among all three models with parameter values $p_j^{\rm opt} - \Delta p_j$, $p_j^{\rm opt}$ and $p_j^{\rm opt} + \Delta p_j$ by looking at all the fits to the various continuum and line data.

Table 22 lists these local estimates Δp_j of our parameter confidence intervals for three selected DIANA standard models. The first two objects HD 163296 and TW Hya have rich continuum and line data, the last object BP Tau has less data, with emphasis on the CO rovibrational data which probes first and foremost the inner disk.

The formal conclusion from this exercise is that we can fit disk gas masses by roughly a factor of two, and dust masses by about 20%. However, this disregards any degeneracies with e.g., the dust opacity parameters. Some parameters like the

Table 22
Error Estimations for Three Example Disks; See the Text for Further Explanations

	HD 163296	TW Hya	BP Tau
Dust parameters			
Minimum dust size $a_{\rm min}$ [μm]	0.020 ± 140%	0.0011 ± 55%	0.049 ± 14%
Maximum dust size $a_{\rm max}$ [mm]	8.2 ± 71%	5.7 ± 105%	3.1 ± 60%
Dust size distribution powerlaw index $a_{\rm pow}$	3.71 ± 0.08	3.99 ± 0.08	3.97 ± 0.05
Volume fraction of amorphous carbon amC [%]	6.0 ± 1.3	25 ± 3	17 ± 4
Dust settling parameter $\alpha_{\rm settle}$	6.6(−3) ± 87%	5.2(−3) ± 120%	6.0(−5) ± 20%
PAH and gas parameters			
Abundance of PAHs $f_{\rm PAH}$	0.076 ± 0.06	0.08 ± 0.1	0.12 ± 0.28
Efficiency of chemical heating $\gamma_{\rm chem}$	0.19 ± 0.28	0.014 ± 0.025	0.13 ± 0.15
Inner disk parameters			
Gas mass $M_{\rm gas}$ [$M_\odot$]	1.3(−4) ± 58%	1.1(−6) ± 31%	7.1(−7) ± 17%
Dust mass $M_{\rm dust}$ [$M_\odot$]	1.5(−9) ± 45%	1.3(−9) ± 62%	6.9(−9) ± 18%
Inner radius $R_{\rm in}$ [au]	0.41 ± 14%	0.078 ± 46%	0.060 ± 33%
Column density exponent ϵ	1.11 ± 0.39	−0.78 ± 0.29	0.52 ± 0.06
Scale height at 1 au H [au]	0.077 ± 5%	0.028 ± 14%	0.12 ± 6%
Flaring exponent β	1.01 ± 0.11	1.21 ± 0.13	1.22 ± 0.02
Outer disk parameters			
Gas mass $M_{\rm gas}$ [$M_\odot$]	5.8(−1) ± 60%	4.5(−2) ± 45%	6.4(−3) ± 50%
Dust mass $M_{\rm dust}$ [$M_\odot$]	1.7(−3) ± 15%	1.0(−4) ± 14%	1.4(−4) ± 25%
Inner radius $R_{\rm in}$ [au]	3.7 ± 18%	4.6 ± 9%	1.3 ± 7%
Tapering-off radius $R_{\rm taper}$ [au]	130 ± 15%	48 ± 9%	32 ± 55%
Column density exponent ϵ	0.95 ± 0.20	1.52 ± 0.13	0.65 ± 0.18
Tapering-off exponent γ	0.20 ± 0.30	0.45 ± 0.23	0.67 ± 0.23
Scale height at 100 au H [au]	6.5 ± 0.2	6.3 ± 0.3	7.1 ± 0.3
Flaring exponent β	1.11 ± 0.03	1.21 ± 0.03	1.12 ± 0.02

PAH abundance (none of the selected objects has clear PAH detections in the mid-IR) and the chemical heating efficiencies can only be determined by order of magnitude, power law indices can roughly be determined by 0.1–0.3, but some disk shape parameters like the scale height and flaring exponent can be determined more precisely, by about 5%–15%.

Appendix C
Detailed mid-IR Spectra

Figure 35 shows enlargements of our SED-fitting models in the mid-IR region in comparison to the *Spitzer*/IRS, *ISO*/SWS and photometric data for 27 objects. These results are discussed in Section 3.2.

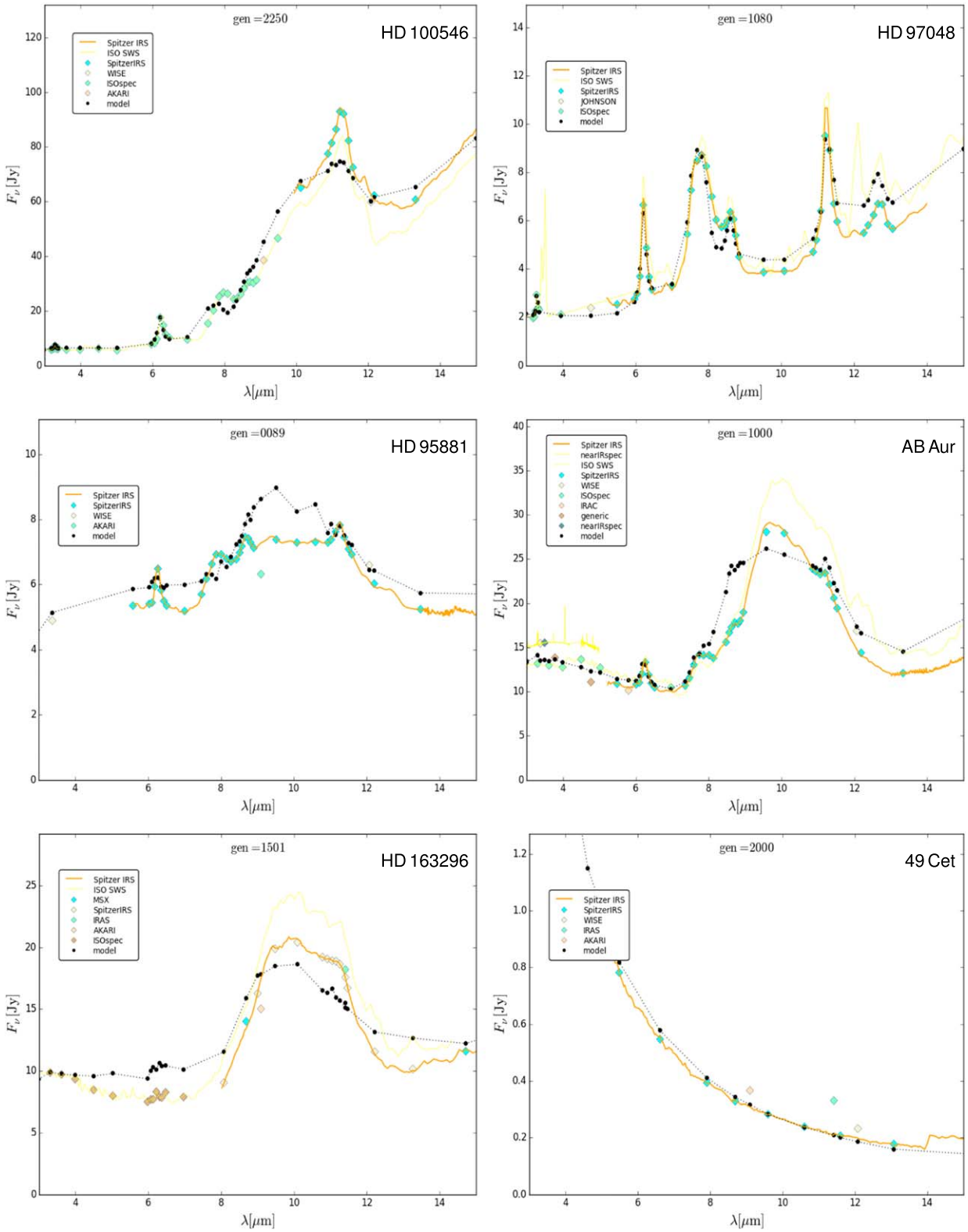

Figure 35. Enlargements of the SED-fits in the mid-IR region on linear scales, centered around the broad silicate emission feature at 10 μm and the PAH emission features at 3.3, 6.25, 7.85, 8.7, 11.3, and 12.7 μm. All results have been obtained with the DIANA standard dust opacities, see text, where only the powerlaw parameters of the dust size-distribution and the volume fraction of amorphous carbon was varied for the fit. Therefore, detailed fits of the spectral shapes of the features are not expected. Concerning the PAHs, only the abundance of the PAHs and the fraction of charged PAHs was varied for fitting.

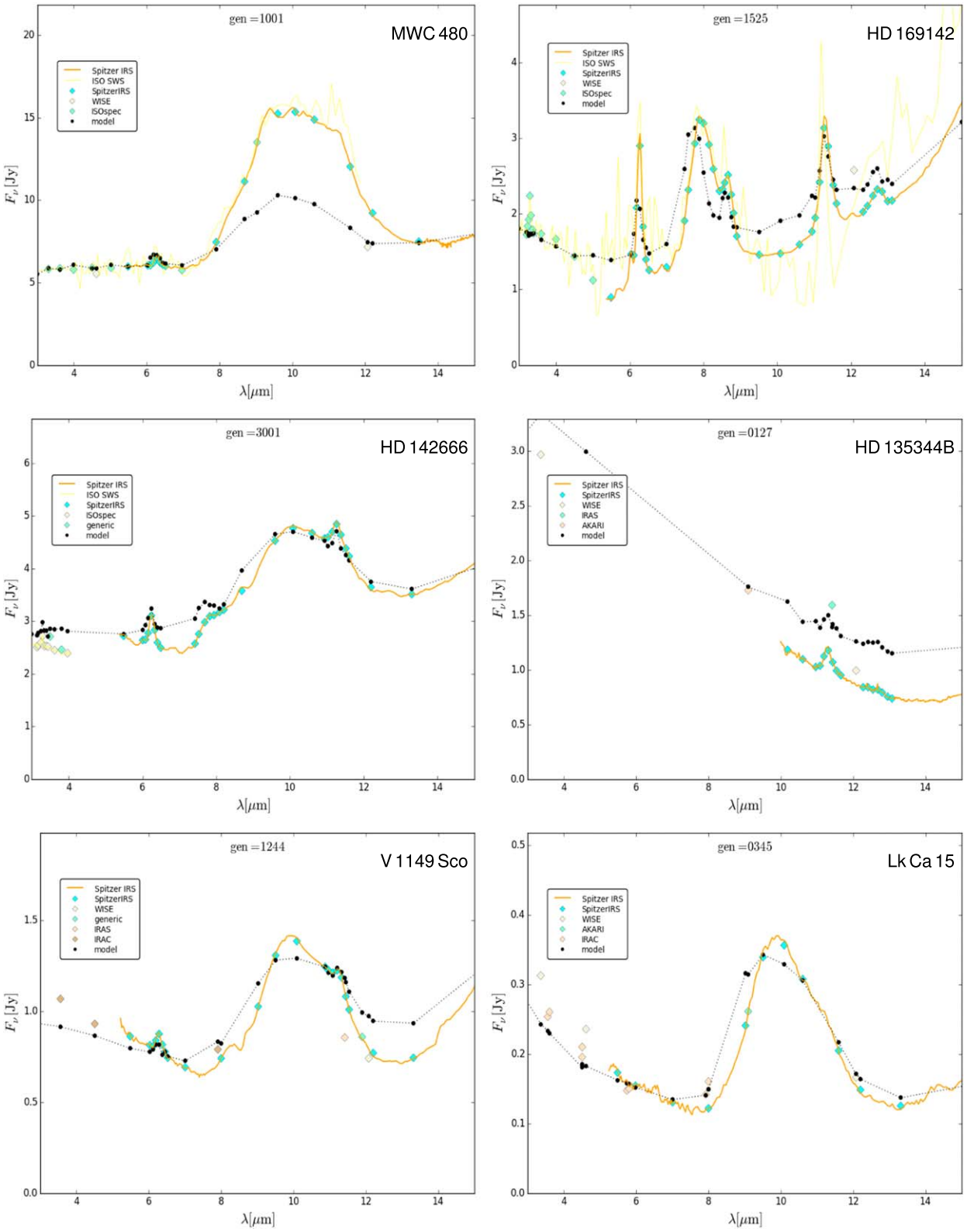

Figure 35. (Continued.)

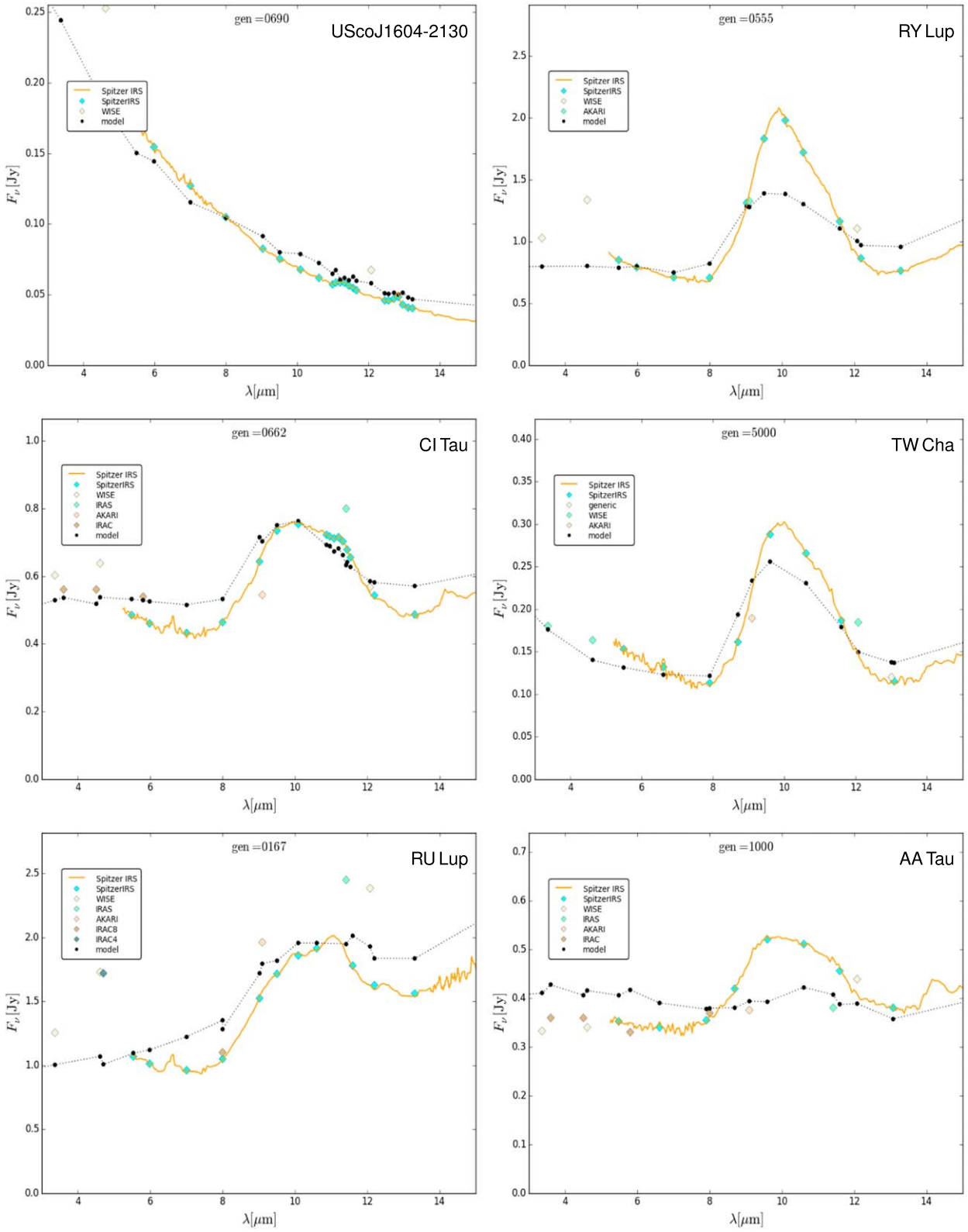

Figure 35. (Continued.)

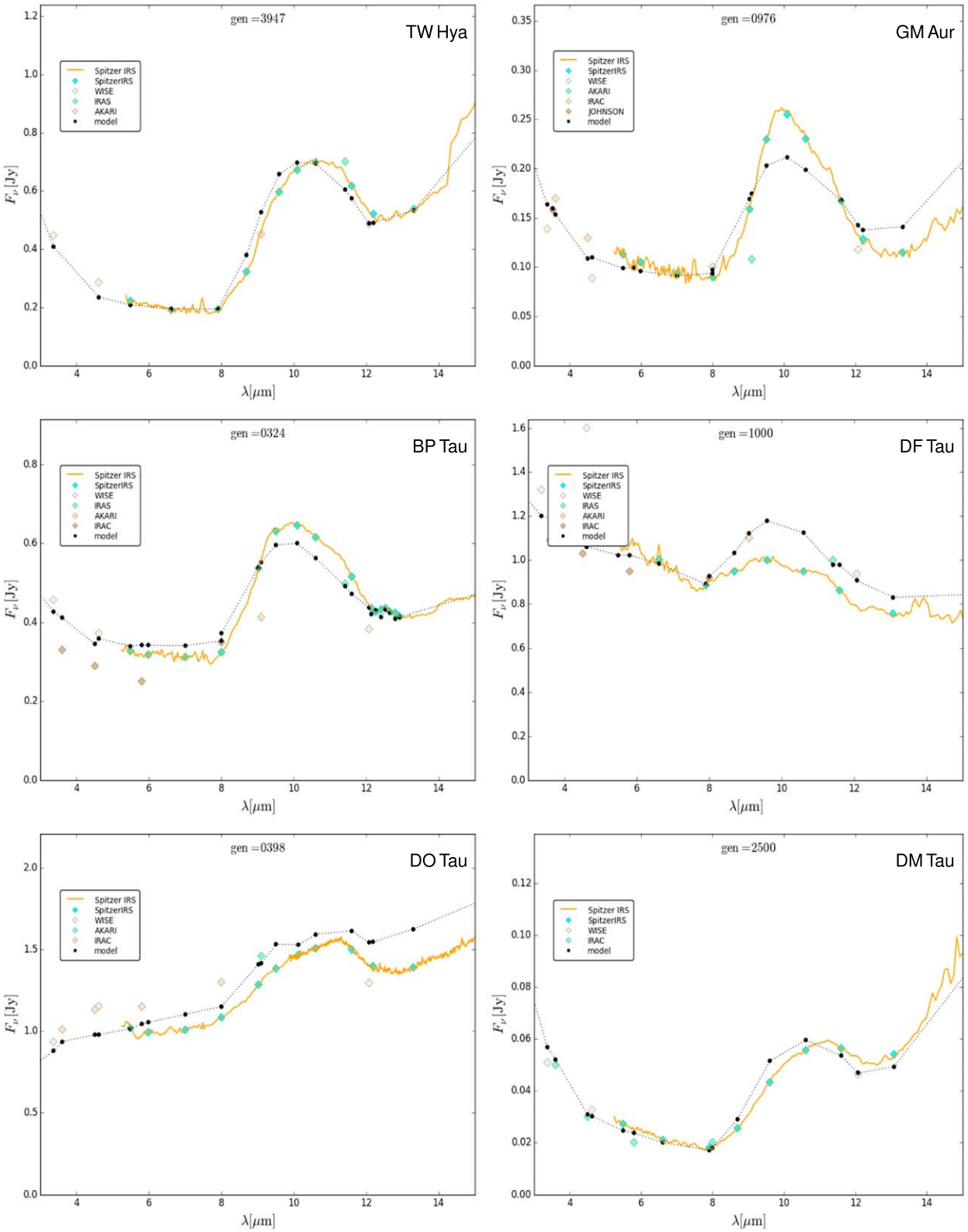

Figure 35. (Continued.)

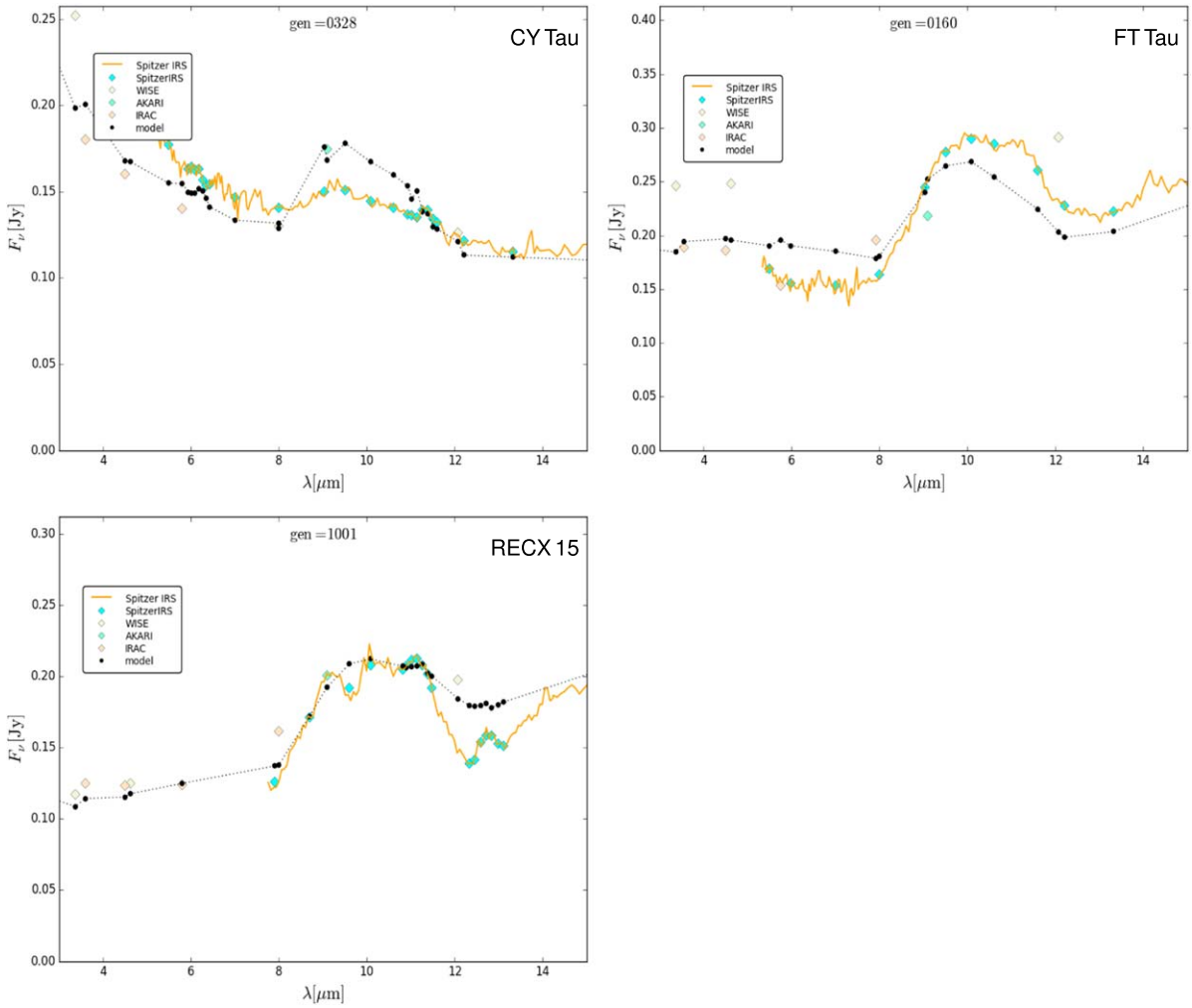

Figure 35. (Continued.)

References

Acke, B., Bouwman, J., Juhász, A., et al. 2010, ApJ, 718, 558
Andrews, S. M., Rosenfeld, K. A., Kraus, A. L., & Wilner, D. J. 2013, ApJ, 771, 129
Andrews, S. M., Rosenfeld, K. A., Wilner, D. J., & Bremer, M. 2011, ApJL, 742, L5
Andrews, S. M., & Williams, J. P. 2005, ApJ, 631, 1134
Andrews, S. M., & Williams, J. P. 2007, ApJ, 659, 705
Andrews, S. M., Wilner, D. J., Zhu, Z., et al. 2016, ApJL, 820, L40
Aresu, G., Kamp, I., Meijerink, R., et al. 2011, A&A, 526, A163
Banzatti, A., Meyer, M. R., Bruderer, S., et al. 2012, ApJ, 745, 90
Beckwith, S. V. W., Sargent, A. I., Chini, R. S., & Guesten, R. 1990, AJ, 99, 924
Bergin, E. A., Cleeves, L. I., Gorti, U., et al. 2013, Natur, 493, 644
Bergin, E. A., Du, F., Cleeves, L. I., et al. 2016, ApJ, 831, 101
Bergner, J. B., Guzmán, V. G., Öberg, K. I., Loomis, R. A., & Pegues, J. 2018, ApJ, 857, 69
Blevins, S. M., Pontoppidan, K. M., Banzatti, A., et al. 2016, ApJ, 818, 22
Boneberg, D. M., Panić, O., Haworth, T. J., Clarke, C. J., & Min, M. 2016, MNRAS, 461, 385
Brinch, C., & Hogerheijde, M. R. 2011, A&A, 523, A25
Brott, I., & Hauschildt, P. H. 2005, in ESA Special Publication 576, The Three-Dimensional Universe with Gaia, ed. C. Turon, K. S. O'Flaherty, & M. A. C. Perryman (Noordwijk: ESA), 565
Bruderer, S. 2013, A&A, 559, A46
Bruderer, S., Doty, S. D., & Benz, A. O. 2009, ApJS, 183, 179
Bruderer, S., van Dishoeck, E. F., Doty, S. D., & Herczeg, G. J. 2012, A&A, 541, A91
Calvet, N., D'Alessio, P., Hartmann, L., et al. 2002, ApJ, 568, 1008
Carmona, A., Pinte, C., Thi, W. F., et al. 2014, A&A, 567, A51
Carmona, A., Thi, W. F., Kamp, I., et al. 2017, A&A, 598, A118
Cazaux, S., & Tielens, A. G. G. M. 2004, ApJ, 604, 222
Cazaux, S., & Tielens, A. G. G. M. 2010, ApJ, 715, 698
Cazzoletti, P., van Dishoeck, E. F., Visser, R., Facchini, S., & Bruderer, S. 2018, A&A, 609, A93
Chapillon, E., Dutrey, A., Guilloteau, S., et al. 2012a, ApJ, 756, 58
Chapillon, E., Guilloteau, S., Dutrey, A., Piétu, V., & Guélin, M. 2012b, A&A, 537, A60
Cleeves, L. I., Bergin, E. A., Qi, C., Adams, F. C., & Öberg, K. I. 2015, ApJ, 799, 204
Cleeves, L. I., Öberg, K. I., Wilner, D. J., et al. 2016, ApJ, 832, 110
D'Alessio, P., Canto, J., Calvet, N., & Lizano, S. 1998, ApJ, 500, 411
Davies, C. L., Kraus, S., Harries, T. J., et al. 2018, ApJ, 866, 23

de Gregorio-Monsalvo, I., Ménard, F., Dent, W., et al. 2013, A&A, 557, A133
Dionatos, O., Woitke, P., Guedel, M., et al. 2019, A&A, in press (arXiv:1902.11204)
Drabek-Maunder, E., Mohanty, S., Greaves, J., et al. 2016, ApJ, 833, 260
Du, F., & Bergin, E. A. 2014, ApJ, 792, 2
Du, F., Bergin, E. A., Hogerheijde, M., et al. 2017, ApJ, 842, 98
Du, F., Bergin, E. A., & Hogerheijde, M. R. 2015, ApJL, 807, L32
Dubrulle, B., Morfill, G., & Sterzik, M. 1995, Icar, 114, 237
Dullemond, C. P., & Dominik, C. 2004, A&A, 417, 159
Dutrey, A., Guilloteau, S., & Guelin, M. 1997, A&A, 317, L55
Dutrey, A., Henning, T., Guilloteau, S., et al. 2007, A&A, 464, 615
Facchini, S., Birnstiel, T., Bruderer, S., & van Dishoeck, E. F. 2017, A&A, 605, A16
Favre, C., Cleeves, L. I., Bergin, E. A., Qi, C., & Blake, G. A. 2013, ApJL, 776, L38
Fedele, D., Bruderer, S., van Dishoeck, E. F., et al. 2013, A&A, 559, A77
Fedele, D., Carney, M., Hogerheijde, M. R., et al. 2017, A&A, 600, A72
Fernandes, R. B., Long, Z. C., Pikhartova, M., et al. 2018, ApJ, 856, 103
Fitzpatrick, E. L. 1999, PASP, 111, 63
Fuente, A., Cernicharo, J., Agúndez, M., et al. 2010, A&A, 524, A19
Fukagawa, M., Hayashi, M., Tamura, M., et al. 2004, ApJL, 605, L53
Garufi, A., Meeus, G., Benisty, M., et al. 2017, A&A, 603, A21
Geers, V. C., van Dishoeck, E. F., Pontoppidan, K. M., et al. 2009, A&A, 495, 837
Geers, V. C., van Dishoeck, E. F., Visser, R., et al. 2007, A&A, 476, 279
Gorti, U., Hollenbach, D., Najita, J., & Pascucci, I. 2011, ApJ, 735, 90
Grady, C. A., Hamaguchi, K., Schneider, G., et al. 2010, ApJ, 719, 1565
Güdel, M., Briggs, K. R., Arzner, K., et al. 2007, A&A, 468, 353
Güdel, M., Lahuis, F., Briggs, K. R., et al. 2010, A&A, 519, A113
Guilloteau, S., Di Folco, E., Dutrey, A., et al. 2013, A&A, 549, A92
Guilloteau, S., Dutrey, A., Piétu, V., & Boehler, Y. 2011, A&A, 529, A105
Guilloteau, S., Piétu, V., Chapillon, E., et al. 2016, A&A, 586, L1
Guzmán, V. V., Öberg, K. I., Loomis, R., & Qi, C. 2015, ApJ, 814, 53
Hales, A. S., De Gregorio-Monsalvo, I., Montesinos, B., et al. 2014, AJ, 148, 47
Harries, T. J. 2000, MNRAS, 315, 722
Henning, T., Semenov, D., Guilloteau, S., et al. 2010, ApJ, 714, 1511
Hillenbrand, L. A., & White, R. J. 2004, ApJ, 604, 741
Honda, M., Inoue, A. K., Okamoto, Y. K., et al. 2010, ApJL, 718, L199
Huang, J., Öberg, K. I., Qi, C., et al. 2017, ApJ, 835, 231
Isella, A., Guidi, G., Testi, L., et al. 2016, PhRvL, 117, 251101
Jamialahmadi, N., Lopez, B., Berio, P., et al. 2018, MNRAS, 473, 3147
Kama, M., Bruderer, S., Carney, M., et al. 2016a, A&A, 588, A108
Kama, M., Bruderer, S., van Dishoeck, E. F., et al. 2016b, A&A, 592, A83
Kamp, I., Thi, W.-F., Meeus, G., et al. 2013, A&A, 559, A24
Kamp, I., Thi, W.-F., Woitke, P., et al. 2017, A&A, 607, A41
Kamp, I., Tilling, I., Woitke, P., Thi, W., & Hogerheijde, M. 2010, A&A, 510, A260000
Kamp, I., Woitke, P., Pinte, C., et al. 2011, A&A, 532, A85
Kraus, A. L., & Ireland, M. J. 2012, ApJ, 745, 5
Lagage, P.-O., Doucet, C., Pantin, E., et al. 2006, Sci., 314, 621
Loomis, R. A., Cleeves, L. I., Öberg, K. I., Guzman, V. V., & Andrews, S. M. 2015, ApJL, 809, L25
Maaskant, K. M., Honda, M., Waters, L. B. F. M., et al. 2013, A&A, 555, A64
Maaskant, K. M., Min, M., Waters, L. B. F. M., & Tielens, A. G. G. M. 2014, A&A, 563, A78
Mannings, V., & Sargent, A. I. 1997, ApJ, 490, 792
Mathews, G. S., Klaassen, P. D., Juhász, A., et al. 2013, A&A, 557, A132
Mathews, G. S., Williams, J. P., & Ménard, F. 2012, ApJ, 753, 59
McClure, M. K., Bergin, E. A., Cleeves, L. I., et al. 2016, ApJ, 831, 167
Meeus, G., Montesinos, B., Mendigutía, I., et al. 2012, A&A, 544, A78
Meeus, G., Waters, L. B. F. M., Bouwman, J., et al. 2001, A&A, 365, 476
Menu, J., van Boekel, R., Henning, T., et al. 2014, A&A, 564, A93
Menu, J., van Boekel, R., Henning, T., et al. 2015, A&A, 581, A107
Min, M., Bouwman, J., Dominik, C., et al. 2016a, A&A, 593, A11
Min, M., Dullemond, C. P., Dominik, C., de Koter, A., & Hovenier, J. W. 2009, A&A, 497, 155
Min, M., Rab, C., Woitke, P., Dominik, C., & Ménard, F. 2016b, A&A, 585, A13
Miotello, A., van Dishoeck, E. F., Kama, M., & Bruderer, S. 2016, A&A, 594, A85
Mohanty, S., Greaves, J., Mortlock, D., et al. 2013, ApJ, 773, 168
Muro-Arena, G. A., Dominik, C., Waters, L. B. F. M., et al. 2018, A&A, 614, A24
Najita, J., Carr, J. S., & Mathieu, R. D. 2003, ApJ, 589, 931
Natta, A., Testi, L., Calvet, N., et al. 2007, in Protostars and Planets V, ed. B. Reipurth, D. Jewitt, & K. Keil (Tucson, AZ: Univ. Arizona Press), 767
Öberg, K. I., Guzmán, V. V., Furuya, K., et al. 2015, Natur, 520, 198
Öberg, K. I., Qi, C., Fogel, J. K. J., et al. 2010, ApJ, 720, 480
Pascucci, I., Testi, L., Herczeg, G. J., et al. 2016, ApJ, 831, 125
Perrin, M. D., Schneider, G., Duchene, G., et al. 2009, ApJL, 707, L132
Piétu, V., Dutrey, A., & Guilloteau, S. 2007, A&A, 467, 163
Pinte, C., Dent, W. R. F., Ménard, F., et al. 2016, ApJ, 816, 25
Pinte, C., Harries, T. J., Min, M., et al. 2009, A&A, 498, 967
Pinte, C., Ménard, F., Duchêne, G., & Bastien, P. 2006, A&A, 459, 797
Pinte, C., Padgett, D. L., Ménard, F., et al. 2008, A&A, 489, 633
Pinte, C., Price, D. J., Ménard, F., et al. 2018, ApJL, 860, L13
Pinte, C., Woitke, P., Ménard, F., et al. 2010, A&A, 518, L126
Pontoppidan, K. M., & Blevins, S. M. 2014, FaDi, 169, 49
Price, D. J., Cuello, N., Pinte, C., et al. 2018, MNRAS, 477, 1270
Quanz, S. P., Avenhaus, H., Buenzli, E., et al. 2013, ApJL, 766, L2
Rab, C., Güdel, M., Woitke, P., et al. 2018, A&A, 609, A91
Rechenberg, I. 1994, Evolutionsstrategie, Optimierung technischer Systeme nach Prinzipien der biologischen Evolution, 246
Rubinstein, A. E., Macías, E., Espaillat, C. C., et al. 2018, ApJ, 860, 7
Semenov, D., Favre, C., Fedele, D., et al. 2018, A&A, 617, A28
Siess, L., Dufour, E., & Forestini, M. 2000, A&A, 358, 593
Sitko, M. L., Carpenter, W. J., Kimes, R. L., et al. 2008, ApJ, 678, 1070
Stolker, T., Sitko, M., Lazareff, B., et al. 2017, ApJ, 849, 143
Teague, R., Semenov, D., Guilloteau, S., et al. 2015, A&A, 574, A137
Testi, L., Birnstiel, T., Ricci, L., et al. 2014, in Protostars and Planets VI, ed. H. Beuther et al. (Tucson, AZ: Univ. Arizona Press), 339
Thalmann, C., Grady, C. A., Goto, M., et al. 2010, ApJL, 718, L87
Thi, W.-F., Mathews, G., Ménard, F., et al. 2010, A&A, 518, L125
Thi, W.-F., Pinte, C., Pantin, E., et al. 2014, A&A, 561, A50
Thi, W.-F., Woitke, P., & Kamp, I. 2011, MNRAS, 412, 711
Tielens, A. G. G. M. 2008, ARA&A, 46, 289
Tilling, I., Woitke, P., Meeus, G., et al. 2012, A&A, 538, A20
Valenti, J. A., Fallon, A. A., & Johns-Krull, C. M. 2003, ApJS, 147, 305
Valenti, J. A., Johns-Krull, C. M., & Linsky, J. L. 2000, ApJS, 129, 399
van der Marel, N., van Dishoeck, E. F., Bruderer, S., et al. 2016, A&A, 585, A58
van der Plas, G., van den Ancker, M. E., Waters, L. B. F. M., & Dominik, C. 2015, A&A, 574, A75
van der Plas, G., Wright, C. M., Ménard, F., et al. 2017, A&A, 597, A32
van der Wiel, M. H. D., Naylor, D. A., Kamp, I., et al. 2014, MNRAS, 444, 3911
Vasyunin, A. I., Semenov, D., Henning, T., et al. 2008, ApJ, 672, 629
Walsh, C., Juhász, A., Meeus, G., et al. 2016, ApJ, 831, 200
Williams, J. P., & Best, W. M. J. 2014, ApJ, 788, 59
Woitke, P., Dent, W. R. F., Thi, W.-F., et al. 2013, in Protostars and Planets VI, Poster #2B013
Woitke, P., Kamp, I., & Thi, W. 2009, A&A, 501, 383
Woitke, P., Min, M., Pinte, C., et al. 2016, A&A, 586, A103
Woitke, P., Min, M., Thi, W.-F., et al. 2018, A&A, 618A, 57
Woitke, P., Pinte, C., Tilling, I., et al. 2010, MNRAS, 405, L26
Woitke, P., Riaz, B., Duchêne, G., et al. 2011, A&A, 534, A44
Wolff, S. G., Perrin, M. D., Stapelfeldt, K., et al. 2017, ApJ, 851, 56
Zhang, K., Pontoppidan, K. M., Salyk, C., & Blake, G. A. 2013, ApJ, 766, 82
Zwintz, K., Kallinger, T., Guenther, D. B., et al. 2009, A&A, 494, 1031